A NEW SINGULAR S-FEM FOR THE LINEAR ELASTIC FRACTURE MECHANICS

SAYEDEH NASIBEH NOURBAKHSH NIA

M.Sc.(Hons.), ISFAHAN UNIVERSITY OF TECHNOLOGY, 2008

A THESIS SUBMITTED

FOR THE DEGREE OF DOCTOR OF PHILOSOPHY

DEPARTMENT OF MECHANICAL ENGINEERING

NATIONAL UNIVERSITY OF SINGAPORE

2012

Acknowledgements

Five years back, when I studied one of professor Gui-Rong Liu's books for the very first time, I never thought of being so lucky one day to be his student. It happened, though, and I got the honor of working on the current thesis under his supervision. I would like to express my deepest appreciation to professor Liu for his dedicated support, guidance and continuous encouragement during my study.

I would also like to express my sincerest gratitude to my second advisor, "Professor Thamburaja Prakash" for kindly taking care of me after Prof. Liu moved to university of Cincinnati. This study could not be accomplished without his continuous support and guidance.

Many thanks to all of my friends and colleagues in "center for Advanced Computations in Engineering and Science (ACES)" at National University of Singapore (NUS), and all of my other friends who created every single moment of happiness during my stay in Singapore. Thanks to all of them for all the memorable fun that I have had with them.

I also would like to express my sincere gratitude to my family, particularly to my parents, for their faithful encouragement and patience, and finally to my husband "Mohammad" for his endless love and support.

Table of Contents

Summary

In the past few decades finite element method has come to be known as one of the most popular and powerful numerical methods in analyzing different engineering structures including those threatened to experience an unpredicted fracture due to the initiation and growth of cracks. To deal with the linear elastic fracture problems, FEM provides a well-established approach of quadratic quarter-point elements to produce the theoretical singularity in the stress and strain field. The following main advantages of FEM are the main reasons of its reputation for being used in different engineering applications;

- The method handles relatively easy different problems with the complicated geometry and arbitrary loading configuration and boundary conditions.
- The method has been well-established in the last decades such that it has a clear structure and possible for being used in developing new software packages.
- The method provides a high reliability because of owning a solid theoretical foundation.

Despite the foregoing features of FEM, it also suffers from a number of disadvantages which consist of;

- Using the lower order elements like linear (triangular or tetrahedral) elements, FEM exhibits an overly stiff behavior; yielding in providing inaccurate results for the stress solutions.
- Using the entire mesh of higher order elements in the framework of FEM results in a considerable amount of increase in the computational time.

To overcome these shortcomings, the present thesis focus on providing a softer model than that of FEM by using the strain smoothing technique on a dual domain of the space discretized with a set of non-overlapping and no-gapping linear elements. Two new methods of singular ES-FEM and singular FS-FEM are then introduced to be used in two and three dimensional spaces. The methods propose new types of crack tip elements to capture the theoretical singularity of stress and strain field based on a simple and direct interpolation method. In 2-D, singular ES-FEM formulates a 5-node triangular crack tip element with the enriched shape functions to produce the singular behavior at the crack tip. Similarly, 10-node prism crack tip element is developed in the method of singular FS-FEM. using the smoothed finite element method, one only need to calculate the displacement (and not the derivatives) over the boundaries of smoothing domains associated to with edges (in 2-D) or faces (in 3-D) of the elements.

The results show that, in both cases of two and three dimensional problems, the proposed methods provide the more accurate results (in terms of strain energy, displacement, and more importantly stress intensity factors) than those of currently widely-used FEM with quarter-point elements. Besides, using the new proposed methods with a base mesh of coarse linear elements without using the any iso-parametric mapping will increase the computational efficiency.

List of Tables

List of Figures

List of symbols

A_k^s	*Area of smoothing domain* Ω_k^s
$A_k^{s,a}$	*Area of sub-smoothing domain*
A_J	*Area path around the crack to calculate J-integral parameter*
$\mathbf{b}$	*Vector of external body forces*
$\mathbf{B}_I(\mathbf{x})$	*Compatible strain gradient matrix*
$\overline{\mathbf{B}}_I^a$	*Strain matrix of sub-smoothing domain*
$\bar{\mathbf{B}}_I(\mathbf{x})$	*Smoothed strain gradient matrix*
C_F	*Constant of Forman model*
C_k	*Constant of Kujawski model*
$\mathbf{d}$	*vector of nodal displacements in standard FEM*
$\bar{\mathbf{d}}$	*vector of nodal displacements in S-FEM*
da/dN	*Crack growth rate*
$\mathbf{D}$	*Symmetric positive definite matrix of material constants*
$\mathcal{D}(S)$	*Delaunay Triangulation for a given set of generator points S*
$\mathbf{f}$	*nodal external force vector*
$\mathbb{H}^m(\Omega)$	*Hilbert space on* Ω
$\mathbb{H}^1(\Omega)$	*Sobolev space on* Ω
$\mathbb{H}_0^1(\Omega)$	*Subset of* $\mathbb{H}^1(\Omega;\mathbb{R}^1)$ *with the vanishing values on the* Γ_u
J	*J-integral parameter*
k_i	*Kolosov constant of material*
$\mathbf{K}$	*Stiffness matrix of FEM*
$\bar{\mathbf{K}}$	*smoothed stiffness matrix of the S-FEM models*
K_I	*Stress intensity factor of the first fracture mode*
K_{II}	*Stress intensity factor of the second fracture mode*
K_{III}	*Stress intensity factor of the third fracture mode*
$\mathbb{L}^2(\Omega)$	*space of square integrable functions on* Ω
q	*Weighting function for the interaction integral calculation*
m_k	*Constant of Kujawski model*

$\mathbf{n}$	*Unit outward normal matrix*
$\mathbf{n}_k^s$	*Outward normal vector matrix on the boundary* Γ_k^s
n_F	*Constant of Forman model*
$n_h^{k,a}$	*Component of outward normal vector matrix on the boundary* $\Gamma_k^{s,a}$
$\mathbf{N}_I(\mathbf{x})$	*Nodal basis shape function*
N_e	*Total number of elements*
N_s	*Total number of smoothing domains*
N_n^s	*Number of nodes associated with the smoothing domain*
$N_{sd,eg}$	*Number of smoothing domains per edge*
$N_{s-sd,eg}$	*Number of sub-smoothing domains per edge*
N_{GP}	*Number of Gaussian points to calculate the integrals*
N_d^{eff}	*Set of effective elements for calculation of interaction integral*
S	*A set of given points to create the Voronoi diagram*
$\mathbf{t}$	*Prescribed traction vector in the x-axis and y-axis*
$\mathbf{u}$	*exact displacement vector in the x-axis and y-axis*
$\mathbf{u}^h$	*approximation solution obtained by the FEM*
$\mathcal{V}(S)$	*Voronoi diagram for a given set of generator points S*
$\mathbf{w_0}$	*Prescribed displacement vector*
Γ	*Problem boundary*
Γ_u	*Essential (Dirichlet) boundary*
Γ_t	*Natural (Neumann) boundary*
Γ_k^s	*Boundary of smoothing domain*
$\Gamma_k^{s,a}$	*Boundary of sub-smoothing domain*
Ω	*Problem domain*
Ω_i^e	*Element domain*
Ω_k^s	*smoothing domain*
$\boldsymbol{\sigma}$	*Exact stress*
∇_s	*Symmetric deferential operator matrix*
$\nabla\mathbf{v}$	*Gradient of* $\mathbf{v}$
β	*Dundurs parameter*

ε	*Bimaterial constant*
$\boldsymbol{\varepsilon}$	*Exact strain vector*
$\boldsymbol{\varepsilon}^h(\mathbf{x})$	*Compatible strain obtained by the FEM*
$\bar{\boldsymbol{\varepsilon}}(\mathbf{x})$	*Smoothing strain obtained by the S-FEM models*
μ_i	*Shear modulus*
ν_i	*Poisson's ratio*
ψ	*Phase angle*
$\|v\|_{\mathbb{L}^2(\Omega)}$	*Norm in* $\mathbb{L}^2(\Omega)$ *space*
$\|v\|_{\mathbb{H}^m(\Omega)}$	*Norm in* $\mathbb{H}^m(\Omega)$ *space*
$\|v\|_{\mathbb{H}^1(\Omega)}$	*Norm in* $\mathbb{H}^1(\Omega)$ *space*
$(v,w)_{\mathbb{L}^2(\Omega;\mathbb{R}^1)}$	*Scalar inner product in* $\mathbb{L}^2(\Omega)$ *space*
$\Phi_k(\mathbf{x})$	*Smoothing function*
Φ	*Nodal basis shape functions for 1-D crack tip element*

Chapter 1: Introduction

"A dream becomes a goal when action is taken toward its achievement."

Bo Bonnett

1.1 Background

Responding to increasing demands in mechanical, aerospace and biomedical applications, several intensive studies have been conducted on the fracture mechanics behavior of materials over the past few decades. The catastrophic crack growth usually leads to the failure of different equipment like aircrafts, infrastructures or automotive structures, threatening human life and imposing additional expenses on the industry. Using developments in fracture mechanics, the inadequacies of the design criteria can be compensated, especially when there is a likelihood of initial crack existence in the structure. The crack propagation under the service load can be anticipated and controlled in such a case.

The primary study on theory of fracture mechanics was conducted by Griffith (1921) to propose a model for the failure of brittle materials, justifying singular behavior of analytical stress around the crack tip. A modified form of the Griffith's approach for the linear elastic fracture mechanics was later developed by Irwin (1958) reformulated in

terms of a parameter called stress intensity factor. Based on this approach stress intensity factor is the most significant parameter in categorizing the crack behavior. Although use of this parameter demands an accurate knowledge of stress field in the vicinity of the crack tip, analytical solutions only exist for selected and relatively simple problems. For more complicated practical cases without an analytical stress solution, however, numerical techniques can be considered as the only way to analyze the structure, where a proper estimation of singular stress field is demanded for an accurate analysis.

One of the most widely-used and best established numerical techniques in the field of linear elastic fracture mechanics is finite element method (FEM). However, the stress singularity at the crack tip cannot be captured when the polynomial basis functions are used in the conventional finite elements, and hence the convergence rate of the solution is badly affected. Currently, the most widely-used singular element for the crack problems is the so-called "eight-node quarter-point element" or the "six-node quarter-point element (collapsed quadrilateral)" in which the mid-side nodes are shifted by a quarter edge-length toward the crack tip. The singularity is then achieved accordingly by the well-known iso-parametric mapping procedure [1-3]. This method only works with the entire element mesh of quadratic elements of the same type which leads to a higher computational cost in comparison with linear elements.

Although several other approaches have been proposed by adding new ideas to the singular FEM, it is still accepted as one of the best methods simulating fracture problems. Among the other developed techniques is extended finite element method (X-FEM) for discontinuous fields by adding some local enrichment functions to the FEM in the

framework of partition of unity finite element method (PUFEM) [4-7]. In the X-FEM settings, however, a layer of "blending" elements will be produced in the transition zone from the enrichment to the usual FEM approximation, leading to a local loss of the partition of unity. Although some strategies were introduced to improve the blending elements in X-FEM and minimize the loss of partition of unity property [8-10], the problem still stands.

On the other hand of developments, a new method of "smoothed-finite element method (S-FEM)" has recently been developed by Liu [11-13] to improve the accuracy of FEM for both two and three dimensional problems. Using linear triangular and tetrahedral elements, the method works very well for continuous fields and provides the more accurate results than FEM. However, the method does not work well for the domains containing discontinuities like crack. In this thesis, a proper treatment is proposed and properly implemented to overcome the deficiency of S-FEM in dealing with fracture problems.

1.2 Objectives and scope of the thesis

Based on what is briefly reviewed in the last section, research gaps for the current FEM-based techniques customized for the fracture problems can be listed as follows:

- **An entire mesh of quadrilateral element type (or higher order elements) is required** in the currently conventional singular FEM, which leads to a significant amount of increase in computational cost. The expensive computational cost of singular FEM can be highlighted more by considering the unavoidable re-meshing

process for the quasi-static or dynamic analyses of crack growth simulations. On the other hand, essential capturing of stress singularity around the crack tip is not achieved if a mesh of linear elements is adapted in the vicinity of crack tip. Unfortunately, in the framework of conventional FEM, the idea of decreasing computational costs by using a combination of quarter-point elements around the crack tip and linear elements on the rest parts of the domain is not applicable because of "incompatibility of displacement field" which will occur in the boundary of adjacent elements of different types.

- **The inherent overly-stiff property of singular FEM** leads to a relative loss of accuracy. A question remains whether it is possible to improve the accuracy by softening the model represented by singular FEM.
- **It is of interest to enhance the performance of FEM in a way that the property of "partition of unity" always is satisfied**. Although, the widely-used approach of extended finite element method (X-FEM) resolves the shortcoming of computational cost by skipping re-meshing process during the crack propagation, another deficiency of locally loss of "partition of unity" in the area of "blending elements" is produced by X-FEM.

The main aim of this study is to develop a singular smoothed finite element method (singular S-FEM) to improve the accuracy and efficiency of FEM for both 2-D and 3-D fracture problems. In this study the following objectives are sought:

- Proposing a novel crack tip element to simulate stress singularity around the crack tip. This element will be used instead of quarter-point elements of singular FEM.

- Increasing the computational efficiency by proposing a new technique which uses a combined mesh of linear elements and novel crack tip elements with an ensured compatibility in the whole displacement field and guaranteed satisfaction of "partition of unity" property in the entire domain.
- Improving the accuracy of results by using "smoothing technique" to resolve the overly-stiff property of FEM.

The new ideas of present study may have significant impact on both accuracy and computational efficiency compared to the available approach of singular FEM for fracture problems by:

- Proposing novel crack tip elements with special shape functions to successfully simulate the stress singularity around the crack tip**,**
- Using "linear elements" instead of "quadratic ones" and "interpolation method" instead of "isoparametric mapping procedure", which may lead to more efficient computational analysis**,** and
- Using "smoothing technique" on the domains associated with the edges and faces of elements (for, respectively, 2-D and 3-D problems) which may provide a method with a higher accuracy and convergence rate than singular FEM.

To narrow the scope in the field of fracture mechanics, this study only focuses on different aspects of linear elastic fracture mechanics (LEFM) and not on the challenges of non-linear fracture mechanics (NLFM). Moreover, considering the fact that "partition of unity" is locally lost in the blending area of X-FEM and referring to our objective of developing a method that satisfies this property everywhere in the

domain, comparing the results of our method with X-FEM is out of scope of this study.

This thesis is outlined as follows. In chapter 2 a brief review on the foundations of linear elastic fracture mechanics is provided followed by a survey on finite element method (FEM) and smoothed finite element method (S-FEM) in chapter 3 and chapter 4, respectively. Then, the method of singular ES-FEM for crack analysis in homogenous materials is introduced in chapter 5, precisely addressing relevant details such as novel crack tip elements, new proposed shape functions, smoothing domains creations and numerical approach for J-integral calculation. The method is then examined through several examples to verify its power in dealing with different problems compared to other approaches. In chapter 6, the newly proposed method of singular ES-FEM is customized for the interfacial crack problems and the performance is investigated through several numerical examples. Next, the quasi-static crack growth using the singular ES-FEM is formulated based on a Delaunay triangulation algorithm and is addressed in chapter 7. The crack trajectories for some benchmark problems are then investigated using the current method and are compared with the experimental observations. Next, the developed approach is used to simulate the more practical case of fatigue crack growth and the results are verified with the reference observations. Later on, in chapter 8, the method of singular faced-based smoothed finite element method (singular FS-FEM) for three dimensional spaces is introduced and formulated with the similar foundations to that of singular ES-FEM. Finally, some conclusions are drawn in chapter 9 and recommendations for future work are presented.

Chapter 2: Linear Elastic Fracture Mechanics

"Problems cannot be solved by the same level of thinking that created them."

Albert Einstein

2.1 Introduction

For a perfect non-defective solid material, stresses are considered to vary smoothly and mechanical behavior is explained based on the theory of elasticity equipped with proper tools to evaluate yield stresses. These stresses are then exerted in the established failure criteria to predict the material failure under loading conditions. For the defective materials like those containing cracks, however, the existence of local discontinuity in the stress field is not properly describable by theory of elasticity; resulting in a non-reliable analysis.

For these kinds of problems, fortunately, another powerful theory of "*fracture mechanics*" has been developed to compensate the deficiency of classical approaches in analyzing crack problems. This theory is usually classified into two major categories named; "*linear elastic fracture mechanics (LEFM)"* which was developed on the basis of linear elastic theory and "*plastic fracture mechanics"* which was established by taking the crack-tip plastic deformation into account.

When the linear elastic principles are applied, it is presumed that the stress is sharply increased by approaching to the crack tip and goes to infinity at the crack-tip point. In reality, however, the resultant plastic deformation due to the high amount of stress prevents the stress values from really going to infinity (e.g. in ductile material). Although considering this plastic behavior is crucial in dealing with problems with a large plastic deformation, for those with a small plastic zone at the vicinity of crack LEFM has been accepted as a reliable method to provide accurate and reasonable predictions of crack behavior.

In this study we will only focus on the LEFM problems, wherein a parameter called "*stress intensity factor"* is introduced to describe the stability behavior of crack based on the state of stress in the vicinity of crack tip. On the other hand, because of the fact that state of stress is solely analytically-available for a very limited number of problems with the very simple "geometries", "loading" and "boundary conditions", implementing a numerical approach to evaluate the stress field for the case of generic problems seems unavoidable.

Responding the mentioned fundamental requirements for the LEFM analysis, in the following sections, a very brief review on the concepts of LEFM is provided, followed by the next chapter as a background survey on the finite element method (FEM) which has come to be known as one of the most popular techniques in the field of solid mechanics computations.

2.2 The Development of fracture mechanics

The "elastic stress concentration" formulation proposed by Ingliss [14] can be known as the first effort in developing theory of fracture mechanics. According to his studies, the local stress for an elliptical hole located inside a solid body shown in Figure 2.1 is amplified to the value of

$$\left(\sigma_y\right)_{max} = \left(2\sqrt{\frac{d}{\rho}}\right)\sigma_y \tag{2.1}$$

In which $\rho = c^2 / d$ is the curvature radius.

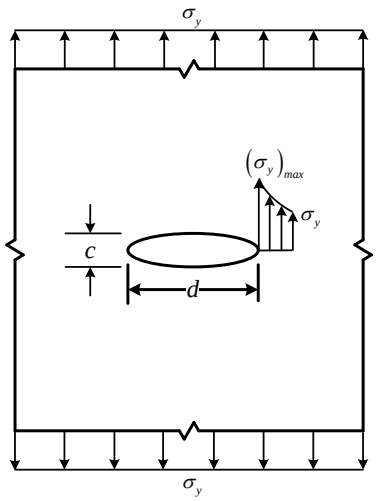

Figure 2.1. A typical elliptical hole inside a body with a remote uniform stress

The elliptical hole will turn to a sharp crack for the limiting case in which one axis (let say, axis *c*) approaches to an infinitesimal value, meaning that Inglis equation predicts an infinite local stress at the crack tip in such a case. Knowing the fact that no real material is capable of sustaining infinite amount of stress, some concerns were created after Inglis's theory.

Later, In 1921, Griffith [15] developed a fracture theory based on energy balance rather than the local stress. He implemented energy conservation principles to a centrally-cracked glass plate. According to his mindset, a crack would start to propagate only when the elastic strain release rate, due to crack extension, exceeded the rate of increase in surface energy associated with the newly formed crack surface.

After calculating the amount of balanced energy U of cracked body and solving $dU/da = 0$ (a stands for the crack length), he obtained the critical crack size a_c as

$$a_c = \frac{(2\gamma_s)E}{\pi\beta\sigma^2} \tag{2.2}$$

Where $2\gamma_s$ is the total surface energy per unit area, E is the Young's modulus, and σ_f is the remote stress. In addition;

$$\beta = \begin{cases} 1 & plane\ \ stress \\ 1-\nu^2 & plane\ \ strain \end{cases} \tag{2.3}$$

For the case of $a \le a_c$, the crack is stable; meaning that it is not extended without an input amount of energy. When $a > a_c$, however, the crack propagation occurs in an unstable manner.

The total surface energy per unit area ($2\gamma_s$) and the remote stress σ_f at failure time can then be found using the equation (2.4) and (2.5). It should be noted that these equations were all derived only based on the energy balance regardless the stress distribution inside the material and around the crack.

$$\gamma_s = \frac{\pi\beta a\sigma^2}{2E} \tag{2.4}$$

$$\sigma_f = \sqrt{\frac{2E\gamma_s}{\pi\beta a}} \tag{2.5}$$

Based on several experimental verifications, it was found that the fracture strength of glass shows a very good agreement with that given by equation (2.5), while for the metals this equation does not provide reasonable estimates of the real fracture strength. In the other word, Griffith approach is only successful in describing fracture behavior of brittle materials and not the non-brittle ones.

Therefore, several investigations were further conducted by other researchers to improve Griffith theory and analyze the fracture of ductile materials as well.

Irwin [16] and Orowan [17] independently modified the Griffith formulation to the following equation which includes an additional term of γ_p that stands for plastic work per unit area of created surface. This term brings the plastic deformation of material into account.

$$\sigma_f = \sqrt{\frac{2E\left(\gamma_s + \gamma_p\right)}{\pi\beta a}} \tag{2.6}$$

Nevertheless, since equation (2.6) is based on the assumptions of Griffith model, the global behavior of the structure must be elastic. In the other words, the plasticity effect must be confined to a small region at the vicinity of crack tip. Using the principles of linear elastic theory, it is possible to derive closed-form solutions for the stress distribution field in some simple cracked solids with special loading and boundary conditions. Westergaard [18], Sneddon [19], Irwin [16] and Williams [20] were among the first researchers to publish such solutions.

To propose a fracture model with capability of explaining behavior of metals, Irwin then focused on stress field rather than the energy balance method of Griffith. He categorized the general behavior of a cracked body based on the geometry of crack and loading conditions by means of introducing three basic different fracture modes called *in-plane opening mode* (due to a symmetric loading), *in-plane sliding mode* (due to an anti-symmetric loading), and *out-of-plane tearing mode* (due to an anti-symmetric loading) as shown in Figure 2.2.

In general, any cracked body is configured as a superposition of these three modes. Using the semi-inverse method of Westergaard, Irwin then expressed the stress components in the vicinity of crack tip as

$$\begin{aligned} \sigma_y &= \frac{K_I}{\sqrt{2\pi r}} f_1(\theta) \\ \tau_{xy} &= \frac{K_{II}}{\sqrt{2\pi r}} f_2(\theta) \\ \sigma_{yz} &= \frac{K_{III}}{\sqrt{2\pi r}} f_3(\theta) \end{aligned} \tag{2.7}$$

Where r is the radial distance from the crack tip and terms $f_i(\theta)$; $(i=1,2,3)$ are functions of polar angle θ. The parameters K_I, K_{II} and K_{III} are also known as the stress intensity factors corresponding to the three fracture modes.

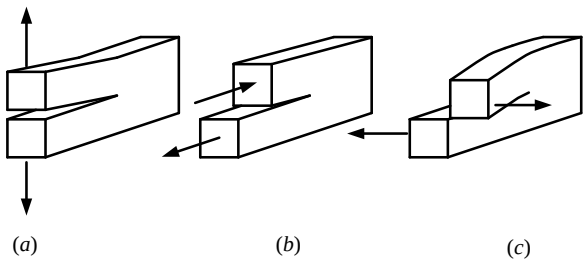

Figure 2.2: The three basic modes of crack extension. (*a*) Opening mode (Mode I), (*b*) Sliding mode (Mode II), (*c*) Tearing mode (Mode III).

As it can be seen in equation(2.7), for a linear elastic fracture problem, Irwin formulation produces a mathematically infinitive stress at the crack tip ($r = 0$) by simply introducing a $1/\sqrt{r}$ term in the stress field. Moreover, the stress intensity factor thoroughly characterizes crack tip condition by relating the remote applied stress to the local stress near the crack tip. The stability condition of crack is then examined by comparing the stress intensity factor with a critical value called fracture toughness, K_c, which is a material parameter depending on thickness of specimen and temperature. Normally K_c can be determined from Izod and Charpy impact test.

2.2.1 Energy Method (J-Integral)

The famous approach of contour integral for the energy release rate was later proposed by Rice [21] to characterize the behavior of non-linear fracture problems. The method was quickly flourished among the researchers all around the world because of its brilliant feature of "*path-independency*". According to this technique, under the assumption of small displacement gradient for a two-dimensional, planar, elastic solid including a sharp crack, a *J* parameter is defined in a line-path integration as [21]:

$$J = -\int_{\Gamma_J} (\sigma_{ij} \frac{\partial u_i}{\partial x_1} - w\delta_{1j}) n_j d\Gamma \tag{2.8}$$

where, w is the strain energy density, δ_{ij} is the kronecker delta, and Γ_J is any path beginning at the bottom crack face and ending on the top face as shown in Figure 2.3. In addition, n_j, σ_{ij} and u_i are, respectively, components of outward unit normal vector **n** on Γ_J, stress tensor, and displacement vector referred to a Cartesian coordinate system located at the crack tip point.

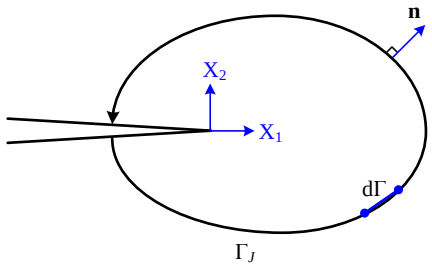

Figure 2.3. Typical closed line-path around the crack tip

As it was mentioned earlier, the significant property of *J*-integral in dealing with crack problems is its "path independency". In numerical calculations, however, a path dependent behavior is usually observed in the results. To cope the case; a smoothing weighting function *q* is multiplied by the integrand of Equation (2.8) as

$$J = -\int_{\Gamma_J} (\sigma_{ij} \frac{\partial u_i}{\partial x_1} - w\delta_{1j}) n_j q d\Gamma \tag{2.9}$$

In addition, to build up a more path independent nature for numerical results, it is strongly recommended to evaluate the integration over an area domain in lieu of a line path [22]. To obtain such an area-domain integration formula, consider a typical two

dimensional sharp-cracked body with an assumed closed contour Γ_J around its crack tip as shown in Figure 2.4, where $\Gamma_J = \Gamma_{J1} \cup \Gamma_- \cup \Gamma_{J2} \cup \Gamma_+$. The area A_J is enclosed by line segments $\Gamma_{J1}, \Gamma_-, \Gamma_{J2}$ and Γ_+. The segments Γ_- and Γ_+ are, respectively, the boundaries of the lower and upper crack face. For such a closed contour, *J*-integral can then be defined in the form of area-integration as [21]:

$$J = \int_{A_J} (\sigma_{ij} \frac{\partial u_i}{\partial x_1} - w\delta_{1j}) \frac{\partial q}{\partial x_j} dA \tag{2.10}$$

where Γ_{1j} is the Kronecker delta and q is now a sufficiently smoothing function defined on A_J . Later on, it will be discussed how q is defined for our -FEM model.

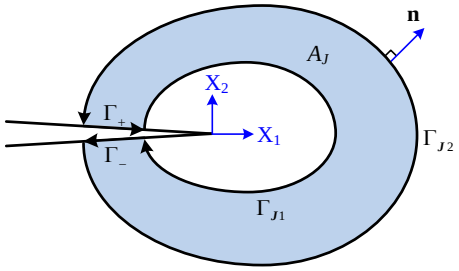

Figure 2.4. Typical closed area- path around the crack tip

2.2.2 More on contour integral and area integral in the numerical analysis

Early use of J-integral with finite element method (FEM) focused on a direct evaluation of equation (2.8) along a contour with the scheme of Figure 2.3 in the FEM mesh. Calculating such a contour integral is quite unfavorable in FEM codes as coordinates and displacements refer to nodal points and stresses and strains to Gaussian integration points. Stress fields are generally discontinuous over element boundaries and extrapolation of stresses to nodes requires additional assumptions [23]. Usually, the

contour is selected to pass through element Gauss integration points, where stresses are expected to be most accurately evaluated. Unfortunately, such an implementation rarely exhibits path independence of the integral**.**

Li *et al.* [22] showed how the contour *J*-integral can be transformed to an equivalent area integral, which is much simpler to implement in a FEM context. The method is quite robust in the sense that accurate values are obtained even with quite coarse meshes; because the integral is taken over a domain of elements, so that errors in local solution parameters have less effect [24].

It is worth of mentioning that, in theory, calculating the integral of equation (2.8) (that contains no *q* parameter as smoothing function) along a closed path contour like the one in Figure 2.4 will produce nothing but zero; since $J_{\Gamma_{J+}} = J_{\Gamma_{J-}} = 0$ (Because, along these lines $n_1 = 0$ and $\sigma_{ij} n_j = 0$) and $J_{\Gamma_{J1}} = -J_{\Gamma_{J2}}$ (Because, J-integral is supposed to be path independent). Therefore, the theoretical value would be $J_{\Gamma_{J+}} + J_{\Gamma_{J-}} + J_{\Gamma_1} + J_{\Gamma_2} = 0$.

Therefore, the equivalent area form of integration produced by divergence theorem will also be equal to zero. In the other words, in the case of having no smoothing function *q*, for an area A_J enclosed by $\Gamma_J = \Gamma_{J1} \cup \Gamma_- \cup \Gamma_{J2} \cup \Gamma_+$, one can write

$$\int_{A_J} \frac{\partial}{\partial x_j} \underbrace{(\sigma_{ij} \frac{\partial u_i}{\partial x_1} - w\delta_{1j})}_{P} dA = \int_{A_J} \frac{\partial P}{\partial x_j} dA = 0 \tag{2.11}$$

In the case of introducing the smoothing function *q* as in equation (2.9), one will be able to get the following relation through the divergence theorem [22, 24]

$$J = \int_{A_J} \frac{\partial}{\partial x_j} (Pq)\, dA = \int_{A_J} (q \frac{\partial P}{\partial x_j} + P \frac{\partial q}{\partial x_j})\, dA \tag{2.12}$$

Using a direct calculation shows that $\frac{\partial P}{\partial x_j} = 0$ over A_J [22], meaning that $\int_{A_J} (q \frac{\partial P}{\partial x_j}) dA$ has no contribution in the foregoing integral. This also means that $\int_{A_J} (\frac{\partial P}{\partial x_j}) dA = 0$ which is identical to what mentioned in equation (2.11); meaning that without using q parameter the area form of integral over a closed path around the crack tip will yield zero value. By implementing the q function, however, one would be able to express the area form of J-integral parameter as $\int_{A_J} (P \frac{\partial q}{\partial x_j}) dA$ (that is nothing but what was mentioned earlier in equation (2.10)). Such a formulation suggests some average value for the J-integral based on the variations of q parameter in the domain.

2.2.3 Relations between Stress Intensity Factors (SIF) and J-integral

Based on the concepts of linear elastic fracture mechanics, for a general mixed mode problem in three dimensional spaces, the following relationships exist between the value of *J*-integral and components of stress intensity factors.

$$\begin{aligned} J &= \frac{K_I^{\,2}}{E^*} + \frac{K_{II}^{\,2}}{E^*} + \frac{K_{III}^{\,2}}{2\mu} && ;\ general\ problem \\ J &= \frac{K_I^{\,2}}{E^*} && ;\ pure\ mode\ I \\ J &= \frac{K_{II}^{\,2}}{E^*} && ;\ pure\ mode\ II \\ J &= \frac{K_{III}^{\,2}}{2\mu} && ;\ pure\ mode\ III \end{aligned} \qquad (2.13)$$

where E^* is defined in terms of material parameters E (Young's modulus) and ν (Poisson's ratio) as equation (2.14)

$$E^* = \begin{cases} E & \textit{plane stress} \\ \dfrac{E}{1-\nu^2} & \textit{plane strain} \end{cases} \quad \& \quad \mu = \frac{E}{2(1+\nu)} \tag{2.14}$$

To extract the values of stress intensity factors from the evaluated amount of *J*-integral in a generic problem, the method of interaction integral method can be used. The method introduces an auxiliary state with the parameters ($\sigma_{ij}^{(aux)}, \varepsilon_{ij}^{(aux)}, u_i^{(aux)}$) to be added to the real state of problem. with the parameters ($\sigma_{ij}^{(1)}, \varepsilon_{ij}^{(1)}, u_i^{(1)}$). For the cases that auxiliary state is chosen as pure mode I, II, or III, one can write

$$\begin{cases} (K_I^{aux} = 1 \ \& \ K_{II}^{aux} = 0 \ \& \ K_{III}^{aux} = 0) & ; \ (\textit{for pure mode I}) \\ (K_I^{aux} = 0 \ \& \ K_{II}^{aux} = 1 \ \& \ K_{III}^{aux} = 0) & ; \ (\textit{for pure mode II}) \\ (K_I^{aux} = 0 \ \& \ K_{II}^{aux} = 0 \ \& \ K_{III}^{aux} = 1) & ; \ (\textit{for pure mode III}) \end{cases} \tag{2.15}$$

In addition, the following relations can be written due to the linearity of problem.

$$\begin{cases} \sigma_{ij}^{(1+aux)} = \sigma_{ij}^{(1)} + \sigma_{ij}^{(aux)} \\ \varepsilon_{ij}^{(1+aux)} = \varepsilon_{ij}^{(1)} + \varepsilon_{ij}^{(aux)} \\ u_i^{(1+aux)} = u_i^{(1)} + u_i^{(aux)} \end{cases} \quad \& \quad \begin{cases} K_I^{(1+aux)} = K_I^{(1)} + K_I^{(aux)} \\ K_{II}^{(1+aux)} = K_{II}^{(1)} + K_{II}^{(aux)} \\ K_{III}^{(1+aux)} = K_{III}^{(1)} + K_{III}^{(aux)} \end{cases} \tag{2.16}$$

After substituting equation (2.16) into equation (2.13), a new term $I^{(1+aux)}$ appears.

$$\begin{aligned} J^{(1+aux)} &= \frac{\left(K_I^{(1)} + K_I^{(aux)}\right)^2}{E^*} + \frac{\left(K_{II}^{(1)} + K_{II}^{(aux)}\right)^2}{E^*} + \frac{\left(K_{III}^{(1)} + K_{III}^{(aux)}\right)^2}{2\mu} \\ &= \underbrace{\frac{\left(K_I^{(1)}\right)^2}{E^*} + \frac{\left(K_{II}^{(1)}\right)^2}{E^*} + \frac{\left(K_{III}^{(1)}\right)^2}{2\mu}}_{J^{(1)}} + \underbrace{\frac{\left(K_I^{(aux)}\right)^2}{E^*} + \frac{\left(K_{II}^{(aux)}\right)^2}{E^*} + \frac{\left(K_{III}^{(aux)}\right)^2}{2\mu}}_{J^{(aux)}} \\ &\quad + \underbrace{\frac{2K_I^{(1)}K_I^{(aux)}}{E^*} + \frac{2K_{II}^{(1)}K_{II}^{(aux)}}{E^*} + \frac{2K_{III}^{(1)}K_{III}^{(aux)}}{2\mu}}_{I^{(1+aux)}} \end{aligned} \tag{2.17}$$

Or

$$J^{(1+aux)} = J^{(1)} + J^{(aux)} + I^{(1+aux)} \tag{2.18}$$

In which $I^{(1+aux)}$ is called the interaction integral between the real state and the auxiliary one and has the following relation with the stress intensity factors associated with real and auxiliary states,

$$I^{(1+aux)} = \frac{2}{E^*}\left(K_I^{(1)}K_I^{(aux)} + K_{II}^{(1)}K_{II}^{(aux)}\right) + \frac{1}{\mu}K_{III}^{(1)}K_{III}^{(aux)} \tag{2.19}$$

The asymptotic case for equation (2.19) occurs when the auxiliary state is set to be one the three pure fracture modes. In such a case the stress intensity factors are calculated as

$$\begin{aligned}\left(K_I^{(1)}\right)^2 &= \frac{E^* I^{(1+pure\,mode\,I)}}{2}\\ \left(K_{II}^{(1)}\right)^2 &= \frac{E^* I^{(1+pure\,mode\,II)}}{2}\\ \left(K_{III}^{(1)}\right)^2 &= \mu I^{(1+pure\,mode\,III)}\end{aligned} \tag{2.20}$$

Based on this equation, the calculation of stress intensity factors for the general mixed mode problem is quite straightforward if the parameter $I^{(1+aux)}$ is given. This parameter is yet to be determined. In the following section, the computational procedure to evaluate the parameter in the two dimensional space is described.

2.2.4 Interaction integral procedure

In the two dimensional space, using the definition of *J*-integral along a path like Γ_J that was previously shown in Figure 2.3, the corresponding *J* value for the state (1+*aux*) is expressed as

$$J^{(1+aux)} = \int_{\Gamma_J} \left(\frac{1}{2}(\sigma_{ij}^{(1)} + \sigma_{ij}^{(aux)})(\varepsilon_{ij}^{(1)} + \varepsilon_{ij}^{(aux)})\delta_{lj} - (\sigma_{ij}^{(1)} + \sigma_{ij}^{(aux)}) \frac{\partial (u_i^{(1)} + u_i^{(aux)})}{\partial x_1} \right) n_j \, d\Gamma \quad (2.21)$$

which can be expanded and re-arranged in the form of equation (2.18) by setting $J^{(1)}$, $J^{(aux)}$, and an $I^{(1+aux)}$ as the following expressions,

$$\begin{aligned} J^{(1)} &= \int_{\Gamma_J} \frac{1}{2}\sigma_{ij}^{(1)}\varepsilon_{ij}^{(1)}\delta_{lj} - \sigma_{ij}^{(1)} \frac{\partial u_i^{(1)}}{\partial x_1} n_j \, dS \\ J^{(aux)} &= \int_{\Gamma_J} \frac{1}{2}\sigma_{ij}^{(aux)}\varepsilon_{ij}^{(aux)}\delta_{lj} - \sigma_{ij}^{(aux)} \frac{\partial u_i^{(aux)}}{\partial x_1} n_j \, dS \\ I^{(1+aux)} &= \int_{\Gamma_J} \left[w^{(1,aux)}\delta_{lj} - \sigma_{ij}^{(1)} \frac{\partial u_i^{(aux)}}{\partial x_1} - \sigma_{ij}^{(aux)} \frac{\partial u_i^{(1)}}{\partial x_1} \right] n_j dS \end{aligned} \quad (2.22)$$

in this equation $w^{(1,aux)}$ is called interaction strain energy and is defined as

$$w^{(1,aux)} = \sigma_{ik}^{(1)}\varepsilon_{ik}^{(aux)} = \sigma_{ik}^{(aux)}\varepsilon_{ik}^{(1)} \quad (2.23)$$

Using the obtained integral form for parameter $I^{(1+aux)}$,and converting it to the area integration form which is given in the following equation, one will be able to calculate the stress intensity factors.

$$J = \int_{A_J} (\sigma_{ij} \frac{\partial u_i}{\partial x_1} - w\delta_{1j}) \frac{\partial q}{\partial x_j} dA \quad (2.24)$$

2.3 Fatigue analysis

One of the most important failure types under the service loading condition is fatigue failure in which the structure undergoes variable amplitude of load. Numerous investigations have been conducted on fatigue crack growth and different models of this behavior have been proposed to date. However, there is no general agreement among the

researchers about the possibility of introducing a unique model for all the materials and problems [25]. In other words, different studies have reported different parameters affecting the fatigue behavior of the structures. Some studies, for instance, highlighted the significance of environmental influences [26, 27], while some others focused on the role of stress ratio R defined by the ratio of minimal to maximal stress of a loading cycle applied in the far field ($R = \frac{S_{\min}}{S_{\max}}$) [28, 29]. Paris and Erdogan were the first to propose a model that assumes fatigue crack growth rate (*FCGR*) da/dN is a function of stress intensity factor range ΔK [30]. According to this model

$$\frac{da}{dN} = C_P(\Delta K)^{n_P} \tag{2.25}$$

Where C_P and n_P are the scaling constants of the log-log plot of da/dN versus ΔK. According to the experimental investigations, the typical logarithmic curve of da/dN versus ΔK consists of three regions as shown in Figure 2.5. The first region represents the early development of fatigue crack growth, while the second and third regions present the stable and accelerated growth zones, respectively. Paris-Erdogan relationship, however, is only able to model the second region, where the equation represents a straight line on the log-log plot. In addition, for some materials like titanium and its alloy, this criterion does not model the actual behavior since the transition point from region two to region three is a function of fracture toughness K_c and stress ratio R beside the value of ΔK [31].

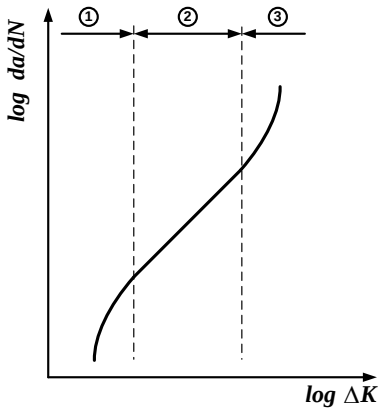

Figure 2.5. Three regions of logarithmic FCGR versus stress intensity factor range

Forman [32] improved the Paris-Erdogan model in such a way that the third region can also be modeled. The mathematical expression of Forman model is

$$\frac{da}{dN} = \frac{C_F(\Delta K)^{n_F}}{(1-R)K_c - \Delta K} \tag{2.26}$$

In which coefficients C_F and n_F are the Forman constants. Later, Walker [33] proposed a similar model for aluminum alloys 2024-T3 and 7075-T6 with driving terms of *R*-ratio and maximum stress intensity factor ($K_{\max}$) as

$$\frac{da}{dN} = C_w\left[(1-R)^m K_{\max}\right]^{n_w} \tag{2.27}$$

The well-known concept of crack closure effect was introduced later by Elber [34] to justify his experimental observations of interfering opposite surfaces during tensile portions of load cycles [35]. Since then, several studies have been conducted on the crack closure phenomenon for different materials and loading conditions [36-42]. On the other hand, in a paper published by Kujawski [43] it was stated that there is no general agreement among all researchers regarding the significance of the crack closure concept.

He proposed a $\left(\Delta K^{+}.K_{max}\right)^{0.5}$ fatigue growth model, instead, which yielded an excellent agreement with the experimental data previously published by Pang et al.[38] and Lee et al. [44], where the plotted data for a given material collapsed on an almost straight line, showing almost no effect of *R* [45]. According to the kujawski's model, the driving force for fatigue crack growth is a combination of $\left(\Delta K^{+}.K_{max}\right)^{0.5}$, where ΔK^{+} is the positive part of the applied stress intensity factor. This method works well for most of aluminum alloys and some other materials [43, 46, 47]. The mathematical expression for the Kujawski's model is as follows:

$$\frac{da}{dN} = C_K (PK)^{m_K} \tag{2.28}$$

Where C_K and m_K are Kujawski's constants and

$$\begin{aligned} PK &= (\Delta K^{+}.K_{max})^{0.5} \\ K_{max} &= \frac{\Delta K}{1-R} \\ &\begin{cases} \Delta K^{+} = \Delta K & for\ R \geq 0 \\ \Delta K^{+} = K_{max} & for\ R < 0 \end{cases} \end{aligned} \tag{2.29}$$

Chapter 3: Finite Element Method (FEM)

" Never try to solve all the problems at once
— make them line up for you one-by-one"

Richard Sloma

3.1 Introduction

Since the numerical approach that will be proposed in the present dissertation is partially built up on the basis of finite element method (FEM), an essential abstract of standard FEM is briefly presented in this chapter by employing a simple mathematical language. The governing equations (including strong and weak formulation) and domain discretization are also discussed. In addition, advantages and disadvantages of FEM are reviewed. For the sake of simplicity in discussion, two-dimensional (2D) problems are chosen as the default. All the formula, however, are generally applicable to linear solid mechanics problems in higher dimension spaces.

3.2 Governing equations for elastic solid mechanics problems

The equilibrium equation for a 2D elastic solid mechanics problem in a physical domain of $\Omega \in \mathbb{R}^2$ bounded with a Lipschitz-continuous boundary Γ with $\Gamma = \Gamma_u + \Gamma_t$, $\Gamma_u \cap \Gamma_t = \emptyset$, is governed by

$$\nabla_s^T . \boldsymbol{\sigma} + \mathbf{b} = \mathbf{0} \quad in \quad \Omega \tag{3.1}$$

In which $\boldsymbol{\sigma} = [\sigma_{xx} \;\; \sigma_{yy} \;\; \sigma_{xy}]^T$ is the stress vector, $\mathbf{b} = [b_x \;\; b_y]^T$ is the vector of external body forces, and ∇_s^T is a symmetric differential operator matrix given by

$$\nabla_s^T = \begin{bmatrix} \dfrac{\partial}{\partial x} & 0 \\ 0 & \dfrac{\partial}{\partial y} \\ \dfrac{\partial}{\partial y} & \dfrac{\partial}{\partial x} \end{bmatrix} \tag{3.2}$$

The essential boundary condition (Dirichlet boundary condition) is given as

$$\mathbf{u} = \mathbf{w_0} \quad on \;\; \Gamma_u \tag{3.3}$$

Where $\mathbf{u} = [u \;\; v]^T$ is the displacement vector with the displacement components of *u* and *v* in the *x* and *y* directions, respectively, and $\mathbf{w_0} = [w_{0x} \;\; w_{0y}]^T$ is the prescribed displacement vector on the essential boundary condition. For more simplicity in discussion, we only consider the problems with the homogenous boundary condition, meaning that

$$\mathbf{u} = 0 \qquad on \;\; \Gamma_u \tag{3.4}$$

The natural boundary or Newman condition is also given as follows

$$\mathbf{n}^T \boldsymbol{\sigma} = \mathbf{t} \quad on \; \Gamma_t \tag{3.5}$$

Where $\mathbf{t} = [t_x \;\; t_y]^T$ is the prescribed traction vector on the natural boundary Γ_t, and $\mathbf{n}$ is the unit outward normal matrix with the components of n_x and n_y in the *x* and *y* directions.

$$n = \begin{bmatrix} n_x & 0 \\ 0 & n_y \\ n_y & n_x \end{bmatrix} \tag{3.6}$$

On the other hand, strain vector of the form $\boldsymbol{\varepsilon} = [\varepsilon_{xx} \;\; \varepsilon_{yy} \;\; \varepsilon_{xy}]^T$ can be calculated using the strain-displacement relation of

$$\boldsymbol{\varepsilon} = \nabla_s \mathbf{u} \tag{3.7}$$

Subsequently, the stress can be evaluated based on the Hook' law

$$\boldsymbol{\sigma} = \mathbf{D}\boldsymbol{\varepsilon} \tag{3.8}$$

In which $\mathbf{D}$ is a symmetric positive definite matrix of material constants.

3.3 Hilbert Spaces

The Hilbert spaces $\mathbb{H}^m(\Omega;\mathbb{R}^1)$ is defined as a set of functions with a square integrable derivatives up to m^{th} order as

$$\mathbb{H}^m(\Omega;\mathbb{R}^1) = \left\{ v \,|\, D^\alpha v \in \mathbb{L}^2(\Omega;\mathbb{R}^1), \forall |\alpha| \le m \right\} \tag{3.9}$$

In which m is a non-negative integer and Ω is a bounded domain in $\mathbb{R}^2$. Besides, $\mathbb{L}^2(\Omega;\mathbb{R}^1)$ is defined as a set of scalar functions $v \in \mathbb{R}^1$ which are piecewise continuous and square integrable over Ω.

$$\mathbb{L}^2(\Omega;\mathbb{R}^1) = \left\{ v \,|\, v \in \mathbb{R}^1 \textit{ is defined on } \Omega \textit{ and } \int_\Omega v^2 d\Omega < \infty \right\} \tag{3.10}$$

$\mathbb{L}^2(\Omega;\mathbb{R}^1)$ is associated with scalar inner product $(v,w)_{\mathbb{L}^2(\Omega;\mathbb{R}^1)}$ as given in equation (3.11). It is also equipped with the corresponding norm $\|v\|_{\mathbb{L}^2(\Omega;\mathbb{R}^1)}$ of equation (3.12):

$$\left(v,w\right)_{\mathbb{L}^2(\Omega;\mathbb{R}^1)}=\int_{\Omega} vwd\Omega \tag{3.11}$$

$$\left\|v\right\|_{\mathbb{L}^2(\Omega;\mathbb{R}^1)}=\left(\int_{\Omega} v^2 d\Omega\right)^{1/2}\equiv\left(v,v\right)^{1/2} \tag{3.12}$$

In addition, $D^{\alpha}v$ is the notation for the general differentiation and is defined as

$$D^{\alpha}v=\frac{\partial^{|\alpha|}v}{\partial x^{\alpha_1}\partial y^{\alpha_2}} \tag{3.13}$$

In which $\alpha=(\alpha_1,\alpha_2)$ and a non-negative integer and $\left|\alpha\right|=\alpha_1+\alpha_2$.

Similar to $\mathbb{L}^2(\Omega;\mathbb{R}^1)$, Hilbert spaces $\mathbb{H}^m(\Omega;\mathbb{R}^1)$ is associated with the scalar inner product $\left(v,w\right)_{\mathbb{H}^m(\Omega;\mathbb{R}^1)}$ and is equipped with the corresponding norm $\left\|v\right\|_{\mathbb{H}^m(\Omega;\mathbb{R}^1)}$ as follows:

$$\left(v,w\right)_{\mathbb{H}^m(\Omega;\mathbb{R}^1)}=\sum_{|\alpha|<m}\int_{\Omega}(D^{\alpha}v)(D^{\alpha}w)d\Omega \tag{3.14}$$

And

$$\left\|v\right\|_{\mathbb{H}^m(\Omega;\mathbb{R}^1)}=\left(\sum_{|\alpha|<m}\int_{\Omega}\left|D^{\alpha}v\right|^2 d\Omega\right)^{1/2} \tag{3.15}$$

It might seem interesting to note that $\mathbb{H}^0(\Omega;\mathbb{R}^1)=\mathbb{L}^2(\Omega;\mathbb{R}^1)$ [48]. Moreover, the most relevant space to the 2-D solid elastic mechanics problems governed by equation (3.1) is the $\mathbb{H}^1(\Omega;\mathbb{R}^1)$ space expressed as:

$$\mathbb{H}^1(\Omega;\mathbb{R}^1)=\left\{v\,|\,v\in\mathbb{L}^2(\Omega;\mathbb{R}^1),\partial v/\partial x_i\in\mathbb{L}^2(\Omega;\mathbb{R}^1),x_i=x,y\right\} \tag{3.16}$$

With the scalar product $\left(u,w\right)_{\mathbb{H}^1(\Omega;\mathbb{R}^1)}$ of the form

$$\left(v,w\right)_{\mathbb{H}^1(\Omega;\mathbb{R}^1)}=\int_{\Omega}(vw+\nabla v.\nabla w)d\Omega \tag{3.17}$$

And the corresponding norm of

$$\|v\|_{\mathbb{H}^1(\Omega;\mathbb{R}^1)} = \left(\int_\Omega \left(v^2 + |\nabla v|^2 \right) d\Omega \right)^{1/2} \tag{3.18}$$

Where in these equations $\nabla v = [\frac{\partial v}{\partial x} \quad \frac{\partial v}{\partial y}]^T$ is denoted as the gradient of v. In addition to the foregoing spaces, a subset of $\mathbb{H}^1(\Omega;\mathbb{R}^1)$ with the vanishing values on the Γ_u is further defined as $\mathbb{H}_0^1(\Omega;\mathbb{R}^1) = \left\{ v \in \mathbb{H}^1(\Omega;\mathbb{R}^1) \,|\, v = 0 \ on \ \Gamma_u \right\}$ and is equipped with the same scalar inner product and norms as $\mathbb{H}^1(\Omega;\mathbb{R}^1)$.

Since the field variable $\mathbf{v}$ for 2-D solid mechanics problems takes a vector form constructed by its components as $\mathbf{v} = \begin{bmatrix} v_x & v_y \end{bmatrix}^T$, the foregoing spaces can be re-written in a more precise form as

$$\mathbb{L}^2(\Omega;\mathbb{R}^2) = \left\{ \mathbf{v} = (v_x, v_y); v_i \in \mathbb{L}^2(\Omega;\mathbb{R}^1), i = x, y \right\} \tag{3.19}$$

And similarly,

$$\mathbb{H}^1(\Omega;\mathbb{R}^2) = \left\{ \mathbf{v} = (v_x, v_y); v_i \in \mathbb{H}^1(\Omega;\mathbb{R}^1), i = x, y \right\} \tag{3.20}$$

With the corresponding norm of

$$\|v\|_{\mathbb{L}^2(\Omega;\mathbb{R}^2)} = \left(\sum_{i=1}^{2} \|v_i\|^2_{\mathbb{L}^2(\Omega;\mathbb{R}^1)} \right)^{1/2} \tag{3.21}$$

And

$$\|v\|_{\mathbb{H}^1(\Omega;\mathbb{R}^2)} = \left(\sum_{i=1}^{2} \|v_i\|^2_{\mathbb{H}^1(\Omega;\mathbb{R}^1)} \right)^{1/2} \tag{3.22}$$

3.4 Variational formulation and weak form

Considering the governing equilibrium equation of (3.1) for a 2-D elastic solid mechanics, the variational formulation and week form is derived as will be briefly discussed in this section.

After multiplying Equation (3.1) with a test function belonging to the Hilbert space ($\mathbf{v} \in \mathbb{H}_0^1(\Omega;\mathbb{R}^2)$) and integrating over the entire problem domain Ω, one can obtain the following relationship

$$\int_{\Omega} \mathbf{v}^T \nabla_s^T \boldsymbol{\sigma} d\Omega + \int_{\Omega} \mathbf{v}^T \mathbf{b} d\Omega = 0, \quad \forall \mathbf{v} \in \mathbb{H}_0^1(\Omega;\mathbb{R}^2) \tag{3.23}$$

Using the Green's divergence theorem [48] and the boundary conditions, the foregoing integral equation can be converted to the following form

$$\int_{\Omega} \left(\nabla_s \mathbf{v}\right)^T \mathbf{D} \left(\nabla_s \mathbf{u}\right) d\Omega = \int_{\Omega} \mathbf{v}^T \mathbf{b} d\Omega + \int_{\Gamma_t} \mathbf{v}^T \mathbf{t} d\Gamma, \quad \forall \mathbf{v} \in \mathbb{H}_0^1(\Omega;\mathbb{R}^2) \tag{3.24}$$

In which the left side of equation has a bilinear form and the right side term is a linear functional. The well-known weak formulation for a typical 2-D solid governed by equation (3.1) and exposed to the boundary condition of equation (3.4) and (3.5) can then be simply stated as "finding a $\mathbf{u} \in \mathbb{H}_0^1(\Omega;\mathbb{R}^2)$ such that equation (3.24) be satisfied".

This single equation consisting of governing equilibrium equation and boundary conditions is the well-known weak formulation statement for a typical 2-D solid governed by equation (3.1) and exposed to the boundary condition of equation (3.4) and (3.5). The advantage of this equation is that it only needs the first derivatives for the trial function $\mathbf{u}$ since the second order derivative terms of $\mathbf{u}$ has been transferred to the test

function $\mathbf{v}$. In the other words, the continuity requirement for the trial function is one order *weakened* in comparison with strong formulation (equation (3.1)) which demands $\mathbf{u}$ to be a second order differentiable term.

3.5 Finite element discretization of problem domain

As it was mentioned before, the test function $\mathbf{v}$ and trial function $\mathbf{u}$ in the variational formulation belong to the Hilbert space $\mathbb{H}_0^1(\Omega;\mathbb{R}^2)$ which is an infinite-dimensional space. For the sake of simplicity, from now on, we let $\mathbb{V}_0 \equiv \mathbb{H}_0^1(\Omega;\mathbb{R}^2)$.

Generally speaking, it is almost impossible to analytically solve the governing equation and provide the *exact* solution; no matter which formulation is used (strong form or weak form). The *approximate* solution, however, can be naturally sought using a variational formulation in the framework of FEM.

In such a case, the approximated solution $\mathbf{u}^h \in \mathbb{V}_0^h$ is introduced on a discrete solution space of finite-dimentsional $\mathbb{V}_0^h$ in which *h* stands for the finite dimension. The above space is a subspace of infinite-dimensional space $\mathbb{V}_0$ ($\mathbb{V}_0^h \subset \mathbb{V}_0$) and we expect that $\mathbb{V}_0^h \to \mathbb{V}_0$ and $\mathbf{u}^h \to \mathbf{u}$ when $h \to 0$. In other words, using the finite-dimensional space $\mathbb{V}_0^h$ instead of $\mathbb{V}_0$ in the varaitional formulation, an approximation error term will be appeared in the analysis process.

For the discretization purpose, the whole domain can be properly decomposed using the polygonal elements for each domain $\Omega \in \mathbb{R}^2$. The domain is covered with N_n non-

duplicating nodes and N_e non-overlapping and no-gaping polygonal elements, that is; $\Omega = \bigcup_{i=1}^{N_e} \Omega_i^e$ and $\Omega_i^e \cap \Omega_j^e = \varnothing$ for $i \neq j$ in which Ω_i^e is the domain of i^{th} element.

Using these assumptions, a set of linearly independent nodal shape functions $\mathbf{N}_1, \mathbf{N}_2, \mathbf{N}_3, ..., \mathbf{N}_{N_n}$ are introduced as a basis for spanning the FEM space $\mathbb{V}_0^h$, where $\mathbf{N}_I(\mathbf{x}) = \begin{bmatrix} N_I(\mathbf{x}) & 0 \\ 0 & N_I(\mathbf{x}) \end{bmatrix}$ is the matrix of shape functions for node *I*. The displacement field is then assumed to be a linear combination of nodal shape functions multiplied by the nodal displacements.

$$\mathbf{u}^h = \sum_{I=1}^{N_n} \mathbf{N}_I(\mathbf{x}) \mathbf{d}_I \tag{3.25}$$

where $\mathbf{x} = \begin{bmatrix} x & y \end{bmatrix}^T$, $\mathbf{d}_I = \mathbf{u}^h(\mathbf{x}_I)$ is the nodal displacement vector of I^{th} node and $\mathbf{x}_I$ is the coordinate of I^{th} node of element housing $\mathbf{x}$. Substituting the discretized displacements in the variational equation, one needs to obtain an $\mathbf{u}^h \in \mathbb{V}_0^h$ such that

$$\int_\Omega \left(\nabla_s \mathbf{v}^h\right)^T \mathbf{D} \left(\nabla_s \mathbf{u}^h\right) d\Omega = \int_\Omega (\mathbf{v}^h)^T \mathbf{b} d\Omega + \int_{\Gamma_t} (\mathbf{v}^h)^T \mathbf{t} d\Gamma, \quad \forall \mathbf{v}^h \in \mathbb{V}_0^h \tag{3.26}$$

Using the shape functions and nodal displacements for the displacement interpolation, the foregoing equation will yield the following system of N_{n} equations

$$\sum_{J=1}^{N_n} \left(\int_\Omega \left(\nabla_s \mathbf{N}_I\right)^T \mathbf{D} \left(\nabla_s \mathbf{N}_J\right) d\Omega \right) \mathbf{d}_J = \int_\Omega (\mathbf{N}_I)^T \mathbf{b} d\Omega + \int_{\Gamma_t} (\mathbf{N}_I)^T \mathbf{t} d\Gamma, \quad I = 1, ..., N_n \tag{3.27}$$

In the conventional FEM framework, the above formulation is re-written in the following matrix form

$$\mathbf{Kd} = \mathbf{f} \tag{3.28}$$

In which **K**, **d**, and **f** are, respectively, the stiffness matrix, nodal displacement vector and nodal external force vector associated with the whole nodes of the model. The stiffness matrix can be calculated using the so-called strain gradient matrix $\mathbf{B}(\mathbf{x})$ as

$$\mathbf{K}_{IJ} = \int_{\Omega} \mathbf{B}_I^T \mathbf{D} \mathbf{B}_J \mathrm{d}\Omega \tag{3.29}$$

In which $\mathbf{B}_I(\mathbf{x})$ is the strain gradient matrix associated with I^{th} node and is calculated as

$$\mathbf{B}_I(\mathbf{x}) = \begin{bmatrix} \dfrac{\partial N_I(\mathbf{x})}{\partial x} & 0 \\ 0 & \dfrac{\partial N_I(\mathbf{x})}{\partial y} \\ \dfrac{\partial N_I(\mathbf{x})}{\partial y} & \dfrac{\partial N_I(\mathbf{x})}{\partial x} \end{bmatrix} \tag{3.30}$$

The entries of external force vector is also computed using the following relation

$$\mathbf{f}_I = \int_{\Omega} (\mathbf{N}_I)^T \mathbf{b} d\Omega + \int_{\Gamma_t} (\mathbf{N}_I)^T \mathbf{t} d\Gamma \tag{3.31}$$

3.6 Advantages and disadvantages of FEM

Using the finite element method for different solid mechanics has been widely popular due to several advantages that it offers including the capability of easily handling different problems with complicated geometries or boundary conditions, multi material domains or non-linear properties. Furthermore, because of its clear structure it seems feasible to develop general purpose FEM software packages.

Nevertheless, FEM is not successful in providing accurate results when the problem domain is discretized with lower order elements. For instance, in the case of using linear elements with triangular or tetrahedral shapes, an overly-stiffness property will be observed in the model behavior. This causes an inaccuracy in the stress solution and needs to be treated either by refining the mesh or using higher order elements. Adopting higher order elements, however, will increase the computational time and reduce the computational efficiency.

This deficiency problem along with some other issues has raised the motivation for the *smoothed finite element method* (S-FEM) to be born. In the next chapter, we will briefly review the S-FEM for the continuous solid domains.

3.7 Mesh Generation (Adaptive Procedure)

When a partial differential equation (PDE) is about to be solved through a commonly used computational approach like finite element method (FEM), first step seems to be nothing but creating a high quality mesh. Generally, mesh can be generated in the *structured* (*uniform*) or *unstructured* form based on the size and shape of distributed elements. Contradictory to the former type that is more suitable to characterize the simplex problems, the latter one is more powerful in dealing with complicated cases, especially when locally large variations are expected in the solution domain of governing PDEs. Moreover, a variety of elements can be used to provide a discretized solution for the unknown variables. In two-dimensional space, for instance, triangular element is very popular since it can be easily used to discretize any arbitrary geometry. To automatically creating triangular meshes, hence, numerous numbers of algorithms have been developed

by the mathematicians and computer scientists around the world. These algorithms are mostly based on the well-known technique of *Delaunay triangulation procedure* proposed in 1934 by Delaunay [49] as a dual approach of the so-called *Voronoi diagrams* previously had established by Voronoi [50]. For a given set of generator points, Delaunay triangulation method deals with decomposing a planar domain into a number of triangular regions at which min-max angle property is assured. According to this property; the minimum angle of all possible Delaunay triangles is maximized, resulting in a higher quality of mesh in which all triangles are very close to the ideal case of congruent with no long thin triangle. Using this idea, several algorithms have been developed by computer scientists and mathematicians to obtain a higher quality of mesh with less running time and expected storage. For instance, "Incremental algorithm" [51-55] is known as one of simplest algorithms among the developed ones, and is based on adding nodes to the body of mesh, one by one, and updating the mesh after each node is added. The process is continued to the point that quality of all the created triangles is sufficiently high. Another type of algorithm proposed by Fortune in the late 1980s [56] is called "Sweepline" and is based on keeping track of a set of edges called "*frontier*" while a conceptual sweep line sweeps up the domain. The method has been even further improved by other researchers [57, 58], showing a good performance when the initial nodes are well-distributed on the problem domain. Other researchers also tried to develop another algorithms similar to the so-called "gift wrapping algorithm for convex hulls" by growing a triangle at a time [59-61]. Later in 1992, Barber [62] presented an algorithm which is based on lifting the nodes into three dimensional space and compute their convex hull. Another approach which is also known as one of the most popular methods is called divide and conquer (D&C)

algorithm. The algorithm is used to recursively break down a complicated problem into several smaller sub-problems of the same type which are simple enough to be directly solved. The solution of the original problem is then obtained as a combination of those for the sub-problems. Although the proper implementation of algorithm is complicated, it usually guarantees the computational efficiency which is very important for complex problems. The first efforts for the construction of Delaunay triangulation with D&C strategy can be affiliated to Hoey and Shamos in the late 1970s when they proposed a D&C algorithm for the construction of Voronoi diagrams with time complexity O(nlogn) in the two dimensional space [63]. Later, the method was modified by Lee and Schachter to directly construct the Delaunay triangulation instead of Voronoi diagrams [64]. Since then, several researchers have proposed different D&C-based algorithms for Delaunay triangulation [51, 60, 65-70].

The mentioned algorithms are only some examples of the massive number of proposed algorithms to create Delaunay triangulation. For more information about the most popular algorithms, the surveys by Bern and Plassmann [71] and Owen [72] can be studied.

3.7.1 Voroni diagrams

The concept of Voronoi diagrams associated with *n* given points in a plane (Assume, *n* is a finite number and let address the given points as generator points for future reference) is a way to decompose that plane into *n* non-overlap and no-gap regions (each is associated with only one generator point) such that any arbitrary point located inside a region is closer to the corresponding generator point than any other one. Mathematically

expressing, if $S \subseteq \mathbb{R}^2$ be a set of *n* given points, then i^{th} voroni region associated with i^{th} point ($i \in S$) is a set of points $x \in \mathbb{R}^2$ with no greater distance from point *i* than from any other point in S; that is,

$$V_i = \left\{ x \in \mathbb{R}^2 \mid \|x - i\| \leq \|x - j\|, \ \forall j \in S \right\} \tag{3.32}$$

Using the perpendicular bisectors, these regions are geometrically constructed as shown in Figure 3.1.

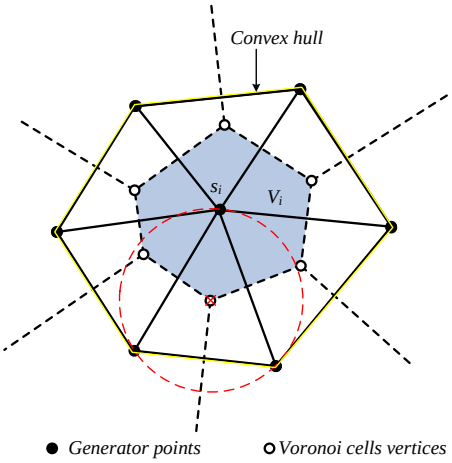

Figure 3.1. Creation of Voronoi diagram for a set of given points in plane; the black dashed lines are the prependicular bisectors of connector lines of two given neigber points, the red circle line shows the circumcircle passing through three given neigber points. The colored area shows the Voroni diagram V_i associated with point s_i.

In this figure, dashed black lines represent the corresponding perpendicular bisectors which create the Voronoi diagram and the colored area show the typical cell V_i associated with point s_i. In addition, a typical circumcircle passing through three generator points is shown in the figure by a red circular line. As it can be observed in the figure, each typical Voronoi cell V_i associated with i^{th} point creates a convex polygonal region with at most *n-1* edges. Each point $x \in R^2$ belongs to at least one Voronoi cell

(meaning that the set of all Voronoi cells cover the entire domain), and at most two Voronoi cells (it only happens when the point *x* lies on the on corresponding bisector). The combination of all Voronoi cells together with their vertices and edges create the Voronoi diagram of generator points *S*.

3.7.2 Delaunay triangulation

For a set of generator points $S = \{s_1, s_2, s_3, \ldots, s_n\}$ (that, hereafter, will be addresses as "*nodes"*), a dual graph of Voronoi diagram $\mathcal{V}(S)$ is constructed by drawing straight lines between any two nodes S with a common edge in their corresponding Voronoi cells. The dual graph for the nodes S is called *Delaunay Triangulation* $\mathcal{D}(S)$ and is typically shown with solid lines in Figure 3.1. For such a Delaunay triangulation structure, the following characteristic can be highlighted as the most important properties:

- There is a one to one correspondence between $\mathcal{V}(S)$ and $\mathcal{D}(S)$, meaning that every triangle of $\mathcal{D}(S)$ is associated with one vertex of $\mathcal{V}(S)$ and vice versa. Similarly, every edge of $\mathcal{D}(S)$ is associated with one edge of $\mathcal{V}(S)$, and every node of $\mathcal{D}(S)$ is associated with one cell of $\mathcal{V}(S)$.
- Using the principles of planar graph theory, it is simply proved that no two edges of $\mathcal{D}(S)$ cross each other [73].
- $\mathcal{D}(S)$ is triangulation if no more than three nodes lie on a common circumcircle. Otherwise, a so-called degeneracy happens which can be resolved with some proper treatments.

- The number of edges for a $\mathcal{D}(S)$ with at least three vertices ($n \geq 3$) could be at most $3n-6$ based on Euler's formulation [73].
- As it is shown in Figure 3.1, the boundary of $\mathcal{D}(S)$ creates a convex hull over the domain in which nodes *S* are distributed.
- The interior region of any triangle contains no other node *S*. This property is equivalently stated by saying that the circumcircle of every three nodes contains no other node.

The last property is practically used in the Delaunay triangulation algorithms as follows; Considering a set of four nodes A, B, C, and D as shown in Figure 3.2, two choices of triangulation can be made based on the circumcircles passing through each three nodes. If the first choice is made and edge *CD* is drawn, the circles *ACD* or *BCD* will, respectively, contain the other node *B* or *A*. In such a case the constructed edge *CD* is considered as illegal and is, therefore, flipped to other choice of *AB*, ensuring the resultant circles of ABC and ABD not containing the fourth node *D* or *C*.

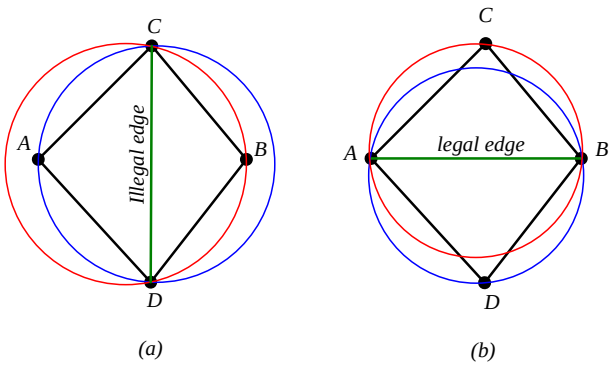

Figure 3.2. two choices of triangulation based on the circumcircles passing through three nodes of each possible traingle

A triangulation assumed to be Delaunay if and only if any arbitrary edge is *locally Delaunay*, meaning that:

i. It belongs to only one triangle (in another word, to the boundary convex hull), or

ii. It is a common edge between two triangles with the corresponding circumcircles that are empty of any other vertex.

Regardless of the way that different algorithms adopt to distribute the vertices or initiate the triangulation, they all implement the simple criterion of flipping edges until all the edges in the domain become locally Delaunay.

A *degeneracy* or *special case*, however, occurs for the set of nodes in Figure 3.2 if all the four nodes locate on the same circumcircle. Such case can be resolved by applying a small perturbation to slightly shift one node, as shown in the following figure in which neither edge *AB* nor *CD* is acceptable since the corresponding circumcircle for any three node passes through the fourth one as well. The problem can be coped with slightly perturbing node *B* from its former position as shown in part (*c*) of figure.

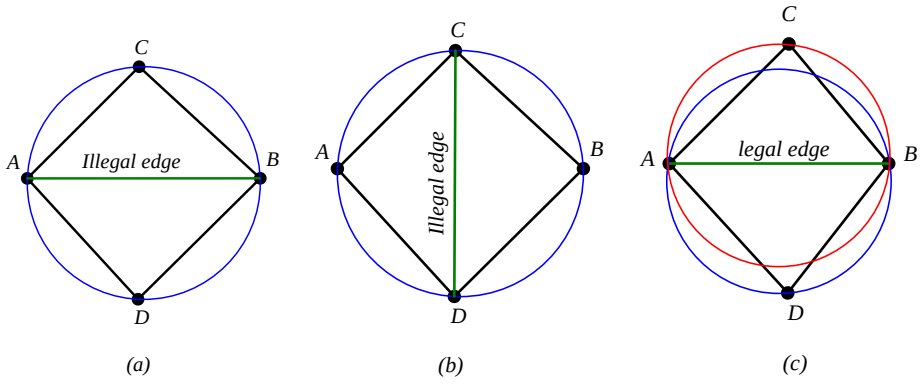

Figure 3.3. (*a*) and (*b*) Special case (degeneracy) when the foure typical nodes *A*,*B*,*C* and *D* are on the same circumcircule (*c*) resolving the degeneracy by a small shift in the location of node *B*

3.8 Finite Element Method for Linear Elastic Fracture Mechanics

Over the last two decades, the finite element method has become firmly established as a standard procedure for the solution of practical fracture problems. There are a number of simulation programs have been developed and even commercialized. Generally, a fundamental difficulty in simulation of linear elastic fracture problems using standard FEM is known as deficiency of conventional elements with the polynomial basis functions in modeling theoretical singular behavior of stress and strain field at the vicinity of crack tip.

Several researchers started to present different FEM models containing special basis functions at the early seventies which none of them was general enough to be used for the general cases of crack problems [74-78]. To produce such an essential singularity in a finite element setting Tracey introduced a $1/\sqrt{r}$ stress singularity within a triangular element. His approach is known as one earliest works to incorporate this fractional term in the simple strain field. Later on, he generalized his approach from triangular elements to another types of elements and created a family of elements with the desired singularity in the stress field [79]. The proposed family of elements, however, was unsuccessful in properly modeling the problems with thermal stresses. Another type of triangular and quadrilateral elements with special singular shape functions of arbitrary order (r^{-p}) were developed by Akin [80]. For $p=1/2$ the resulting shape function is identical to that previously given by Blackburn [81] when he had proposed a singular strain field for triangular elements. For simulating the essential singularity using quadrilateral elements, Benzley [82] also introduced some supplementary terms to the displacement field.

However, the significant milestone in the development of finite element method for the linear elastic fracture problems was the simultaneous and independent discovery of "quarter-point" elements proposed by Henshell and Shaw [83] and Barsoum [2] as shown in Figure 3.4 (a) and Figure 3.4(b) ,respectively.

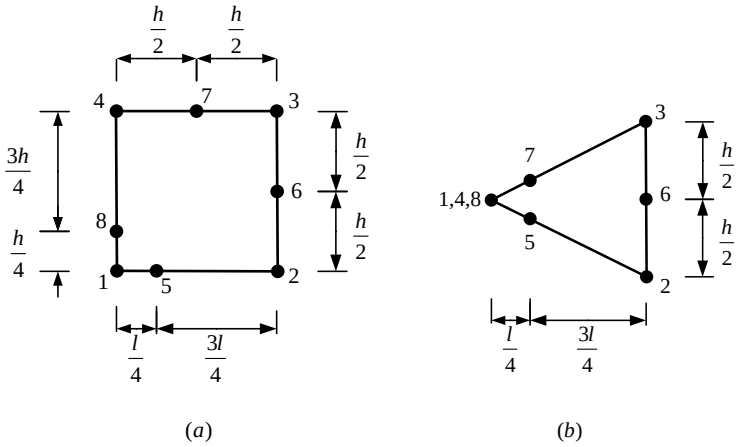

Figure 3.4. (*a*) Quadrilateral Quarter-Point element proposed by Henshel and Shaw (*b*)) Collapsed Quadrilateral Quarter-Point element proposed by Barsoum

They showed that a proper $1/\sqrt{r}$ singularity in the strain and stress field can be created by simply using the standard quadratic order isoparametric finite elements and shifting the mid-side nodes of the edges directly connected to the crack tip to the position one-quarter of that edge. Using this simple shifting method along with the isoparametric mapping procedure, produces a desired singularity.

Instead of using collapsed quadrilateral elements, Freese and Tracy [84] also suggested to directly use the so-called "natural triangular quarter-point element" which is nothing but 6-node crack tip element as shown in Figure 3.5. In the following sections a brief review on the quarter-point elements is presented to provide a better understanding about the effect of shifting method. A typical quadratic 1-D element is explained first,

and the algebraic principles for higher dimensionality elements are derived in the same way as 1-D element. They only differ in the appearance of final equations which are more complicated for the higher order elements.

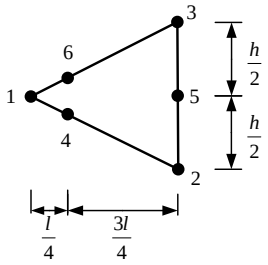

Figure 3.5. The natural triangular quarter-point element (6-node crack tip element)

3.8.1 One dimensional quarter-point element

A one dimensional element is shown in Figure 3.6 in both parametric space and Cartesian space. In this figure, the crack tip is located at $r = 0$, and α is introduced as the parameter that controls middle node position in the settings of Cartesian coordinates.

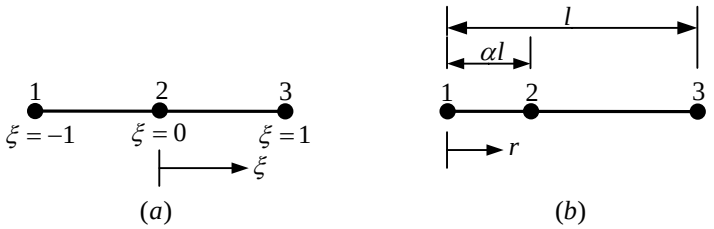

Figure 3.6. One dimensional quadratic element (a) natural coordinate (parametric space) of element (b) Cartesian space of element

Using the parametric coordinate of the element, the displacement component u at any point of the element can be evaluated using the nodal values and the shape functions as

$$u(\xi) = \sum_{i=1}^{3} N_i(\xi) u_i = \frac{1}{2}\xi(1-\xi)u_1 + (1-\xi^2)u_2 + \frac{1}{2}\xi(\xi+1)u_3 \tag{3.33}$$

Which can be re-written as

$$u(\xi) = u_2 + \frac{1}{2}(u_3 - u_1)\xi + (\frac{1}{2}(u_3 + u_1) - u_2)\xi^2 \tag{3.34}$$

Using the similar approach, the following relation can be found between Cartesian coordinate r and parametric coordinate ξ

$$r = \sum_{i=1}^{3} N_i(\xi) r_i = \alpha l + \frac{1}{2} l\xi + l(\frac{1}{2} - \alpha)\xi^2 \tag{3.35}$$

After using the above relation and setting $\alpha = \frac{1}{4}$, one can express ξ as $\xi = \frac{2\sqrt{lr}}{l} - 1$. The interpolated displacement u at any point of Cartesian coordinate can then be obtained by substituting ξ into equation (3.34) as

$$u(r) = u_1 + 2(u_1 - 2u_2 + u_3)\frac{r}{l} + (-3u_1 + 4u_2 + u_3)\frac{\sqrt{lr}}{l} \tag{3.36}$$

The strain can then be evaluated by differentiating the displacement as

$$\varepsilon(r) = \frac{du(r)}{dr} = \frac{2}{l}(u_1 - 2u_2 + u_3) + \frac{1}{2\sqrt{l}}(-3u_1 + 4u_2 + u_3)\frac{1}{\sqrt{r}} \tag{3.37}$$

As it is clearly observed based on the derived equation; the expression for the strain field contains a singular term $\frac{1}{\sqrt{r}}$ which resembles the lead term for the stress and strain in the LEFM. This is the term that simulates the desired singular behavior of the crack

problems and can be produced only through a mapping procedure when the middle node is located in a special location of one-quarter of the element ($\alpha = \frac{1}{4}$).

For instance, let assume $\alpha = \frac{1}{2}$ which results in the mapping relation $\xi = \frac{2r}{l} - 1$. Following the similar foregoing procedure to obtain the displacement and strain field in the Cartesian coordinate, one can find

$$u(\xi) = u_1 + (-3u_1 + 4u_2 - u_3)\frac{r}{l} + 2(u_1 - 2u_2 + u_3)\frac{r^2}{l^2}$$
$$\varepsilon = \frac{du}{dr} = \frac{1}{l}(-3u_1 + 4u_2 - u_3) + \frac{4}{l^2}(u_1 - 2u_2 + u_3)r \tag{3.38}$$

Meaning that strain field around the crack tip is assumed to vary in a linear fashion which does not conform to the theory of LEFM.

3.8.1 Two dimensional quarter-point element

Referring to the two dimensional elements shown in Figure 3.7, two edges 1-5-2 and 1-7-4 resemble the 1-D quarter-point element described in the previous section, meaning that desired singular strain field along these edges is created in the similar fashion as in 1-D element. This may not necessarily happen along other straight lines radially connected to the crack tip node. For his proposed collapsed quadrilateral element, however, Barosoum [85] showed that for the case in which node 6 is exactly located at the mid-side of edge 2-3 (See, Figure 3.4 (b)), the proper singular form is generated along all radial straight lines emanating from crack tip. A similar singular behavior was also predicted by Freese and Tracey [84] for the natural triangular quarter-point elements shown in Figure 3.5. In their study, they also explained that if a quadrilateral element with the natural

coordinates ξ and η of Figure 3.7 (a) is collapsed, for all paths in which η remains constant the strain varies in the similar singular fashion of 1-D quarter-point element. According to them, these paths form a set of radial straight lines emanating from crack tip node for the case that node 6 is exactly at the mid-side point of edge 1-2 as shown in Figure 3.7(b). It is obvious that this finding confirms Barsoum's justification about the singular field inside the collapsed quadrilateral elements.

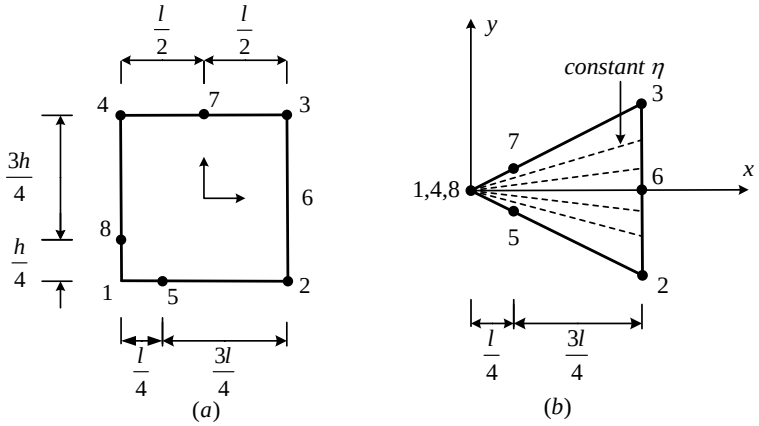

Figure 3.7. (*a*) The parametric coordinates for a typical quadratic quarter-point element (b) striaght lines with the constant η inside the collapsed element if node 6 is exactly located at the mid-side of edge 1-2.

According to the studies conducted by Banks-Sills and Bortman [86, 87], it was demonstrated that a quadrilateral quarter-point element also has a singular behavior along all the lines emanating from crack tip node, but only in a very small region around the crack tip and only if the element has the rectangular shape as shown in Figure 3.8.

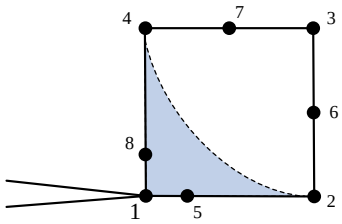

Figure 3.8. The singular region inside the quadrilateral quarter-point element

Generally, triangular elements (collapsed quadrilateral or 6-node crack tip element) are more popular, in practice, comparing to the quadrilateral elements. The main reason is that it is much easier to properly generate and refine the mesh when triangular elements are used. On the other hand, less number of quadrilateral elements can be created around the crack tip which can leads to the less accurate estimation of trigonometric functions of displacement and stress field in the circumferential direction.

Chapter 4: Smoothed Finite Element Method

"Do not seek to follow in the footsteps of the men of old; seek what they sought."

Basho

4.1 Introduction

As it was mentioned in previous chapter, by implementing discretized form of weak formulation in the framework of finite element method (FEM), one will be able to compute the energy potential functional based on the compatible strain field $\boldsymbol{\varepsilon}^h(\mathbf{x})$ which is evaluated using the derivatives of assumed displacement field $\mathbf{u}^h \in \mathbb{V}_0^h$ as

$$\boldsymbol{\varepsilon}^h(\mathbf{x}) = \nabla_s \mathbf{u}^h(\mathbf{x}) \tag{4.1}$$

$\boldsymbol{\varepsilon}^h(\mathbf{x})$ is then used to create the stiffness matrix and estimate the nodal displacement values. In the smoothed finite element method (S-FEM), however, a modified compatible strain field is created based on the strain smoothing technique [88] to define a proper weak energy form that does not demand the derivatives of displacement field for the stiffness matrix calculation. It can be computed, instead, only by using the values of displacement field.

4.2 General Formulation of S-FEM

In the S-FEM, a background mesh of elements is required and can be generated in the same manner as in FEM. Based on the generated elements, the problem domain Ω is then divided into N_s number of non-overlap and no-gap smoothing domains such that $\Omega = \bigcup_{k=1}^{N_s} \Omega_k^s$ and $\Omega_i^s \cap \Omega_j^s = \varnothing$ for $i \neq j$ in which Ω_k^s is the domain of k^{th} smoothing domain. Based on the way that smoothing domains are created, various S-FEM models with different properties have been developed. Some of the most popular S-FEMs consist of cell-based S-FEM (CS-FEM) [11, 12, 89], node-based S-FEM (NS-FEM) [90], edge-based S-FEM (ES-FEM) [91], alpha-FEM [92] and face-based S-FEM (FS-FEM) [93].

Generally, in order to smoothing the compatible strain field $\boldsymbol{\varepsilon}^h(\mathbf{x})$ of FEM to be fit in the S-FEM settings, a smoothing function $\Phi_k(\mathbf{x})$ is introduced to generate the smoothed strain $\bar{\boldsymbol{\varepsilon}}_k(\mathbf{x})$ in each smoothing domain k as

$$\bar{\boldsymbol{\varepsilon}}_k(\mathbf{x}) = \int_{\Omega_k^s} \boldsymbol{\varepsilon}^h(\mathbf{x}) \Phi_k(\mathbf{x}) d\Omega \tag{4.2}$$

In which area of Ω_k^s is evaluated as $A_k^s = \int_{\Omega_k^s} d\Omega$, and $\Phi_k(\mathbf{x})$ satisfies unity property as

$$\int_{\Omega_k^s} \Phi_k(\mathbf{x}) d\Omega = 1 \tag{4.3}$$

Setting the smoothing function to a piecewise constant step function as equation (4.4), the smoothed strain will be expressed as equation (4.5)

$$\Phi_k(\mathbf{x}) = \begin{cases} 1/A_k^s & \mathbf{x} \in \Omega_k^s \\ 0 & \mathbf{x} \notin \Omega_k^s \end{cases} \tag{4.4}$$

$$\bar{\boldsymbol{\varepsilon}}_k(\mathbf{x}) = \frac{1}{A_k^s} \int_{\Omega_k^s} \boldsymbol{\varepsilon}^h(\mathbf{x}) d\Omega = \frac{1}{A_k^s} \int_{\Omega_k^s} \nabla_s \mathbf{u}^h(\mathbf{x}) d\Omega \tag{4.5}$$

The assumed displacement field is continuous over the problem domain covered with N_s smoothing domains Ω_k^s that, in general, each of them can consist of more than one subdivision named sub-smoothing domain $\Omega_{k,p}^s$.

In the two dimensional space, by applying the divergence theorem on equation (4.5), the domain integration over the smoothing domain will be converted to the line integration along the boundaries of smoothing domain as

$$\bar{\boldsymbol{\varepsilon}}_k(\mathbf{x}) = \frac{1}{A_k^s} \int_{\Gamma_k^s} \mathbf{n}_k^s \mathbf{u}_k^h d\Gamma \tag{4.6}$$

Where Γ_k^s is the boundary of k^{th} smoothing domain Ω_k^s, and $\mathbf{n}_k^s$ is a matrix of outward normal vector on that boundary represented in the following form:

$$\mathbf{n}_k^s = \begin{bmatrix} n_{kx}^s & 0 \\ 0 & n_{ky}^s \\ n_{ky}^s & n_{kx}^s \end{bmatrix} \tag{4.7}$$

In which n_{kx}^s and n_{ky}^s are the components of outward normal vector in the *x* and *y* axis, respectively. Now by substituting the discretized displacement field of equation (3.25) into equation (4.6), one can obtain the following matrix form for the smoothed strain

$$\bar{\boldsymbol{\varepsilon}}_k(\mathbf{x}) = \sum_{I=1}^{N_n^s} \bar{\mathbf{B}}_I \bar{\mathbf{d}}_I \tag{4.8}$$

Where N_n^s is the number of nodes associated with smoothing domain, $\bar{\mathbf{d}}_I$ and $\bar{\mathbf{B}}_I$ are, respectively, the smoothed displacement vector and smoothed strain gradient matrix associated with I^{th} node of the smoothing domain. $\bar{\mathbf{B}}_I$ can be represented as

$$\bar{\mathbf{B}}_I = \frac{1}{A_k^s} \int_{\Gamma_k^s} \mathbf{n}_k^s \mathbf{N}_I d\Gamma = \begin{bmatrix} \bar{b}_{Ix} & 0 \\ 0 & \bar{b}_{Iy} \\ \bar{b}_{Iy} & \bar{b}_{Ix} \end{bmatrix} \tag{4.9}$$

In which

$$\bar{b}_{Ih} = \frac{1}{A_k^s} \int_{\Gamma_k^s} n_{kh}^s N_I d\Gamma \qquad (h = x, y) \tag{4.10}$$

This equation is numerically re-written in the following form

$$\bar{b}_{Ih}(x_k) = \frac{1}{A_k^s} \sum_{i=1}^{M} \sum_{j=1}^{N_{GP}} N_I(x_{i,j}^{GP}) w_{i,j}^{GP} n_{ih}^k \quad ; (h = x, y) \tag{4.11}$$

where *M* is the number of (line) boundary segments of Γ_k^s, $x_{i,j}^{GP}$ is the Gaussian point location on the ith boundary segment, $w_{i,j}^{GP}$ is the Gaussian weight associated with the Gaussian point $x_{i,j}^{GP}$, N_{GP} is the number of Gaussian points on the i^{th} boundary segment, and n_{ih}^k is the h^{th} component of the unit outward vector on the i^{th} boundary segment.

After calculation of strain gradient components, the stiffness matrix and algebraic system of equations for the S-FEM solution can be formulated using the same procedural steps followed to develop the FEM system of equations. The final formulation differs from FEM only in some parameters which are substituted with their smoothed peers; for

instance, compatible strain $\boldsymbol{\varepsilon}^h$, element domain Ω_i^e, total number of elements N_e, and strain gradient matrix $\mathbf{B}_I$ are, respectively, replaced with smoothed strain $\bar{\boldsymbol{\varepsilon}}$, smoothing domain Ω_k^s, number of smoothing domains N_s and smoothed gradient matrix $\bar{\mathbf{B}}_I$. As a result, the final formulation for the S-FEM will be in the form of equation

$$\bar{\mathbf{K}}\bar{\mathbf{d}} = \mathbf{f} \tag{4.12}$$

$\bar{\mathbf{K}}$ is called the smoothed stiffness matrix and is calculated in the similar way to the FEM stiffness matrix. The entities of $\bar{\mathbf{K}}$ over k^{th} smoothing domain is given by

$$\mathbf{K}_{IJ(k)} = \int_{\Omega} \bar{\mathbf{B}}_I^T \mathbf{D} \bar{\mathbf{B}}_J \mathrm{d}\Omega \tag{4.13}$$

This equation can be more simplified as equation (4.14) based on the strain smoothing assumption over each smoothing domain that will yield to the constant matrix for $\bar{\mathbf{B}}_I$

$$\bar{\mathbf{K}}_{IJ(k)} = A_k^s \bar{\mathbf{B}}_I^T \mathbf{D} \bar{\mathbf{B}}_J \tag{4.14}$$

The total stiffness matrix is then constructed using an assembly procedure similar to that in FEM. In summary, the numerical algorithm for a S-FEM can be outlined as follow:

1. The domain is discretized using a background mesh in the same manner as in FEM.
2. Based on the information for the nodes and elements connectivity, new smoothing domains are created and the information for nodes contributing to each smoothing domain is identified.

3. For each smoothing domain:
    - For each segment of the smoothing domain boundary, the outward unit normal vector is determined.
    - The strain gradient matrix $\bar{\mathbf{B}}_I$ is calculated using equations (4.11) and (4.9).
    - The stiffness matrix entries associated with the smoothing domain is then calculated using equation (4.14).
4. The global stiffness matrix is calculated by assembling the stiffness matrices of smoothing domains.
5. The boundary conditions and nodal load vector are applied.
6. The linear system of equations is solved to calculate the nodal displacement vector.

As it was mentioned before, based on the way that smoothing domains are created different types of S-FEM are developed with the similar computational steps listed above. These different types of S-FEM are briefly addressed as follows.

4.3 Cell-Based Smoothed Finite Element Method (CS-FEM)

In the CS-FEM, the number of smoothing domains N_s can be the same as the number of elements N_e , meaning one element is assumed to be one smoothing domain. More number of smoothing domains, however, can be created by further subdividing each element into more cells. Figure 4.1 shows the smoothing domain construction in a typical CS-FEM. As it can be seen, the smoothing domains can be simply created by

connecting mid-edge points of opposite segments in parent smoothing domain to each other.

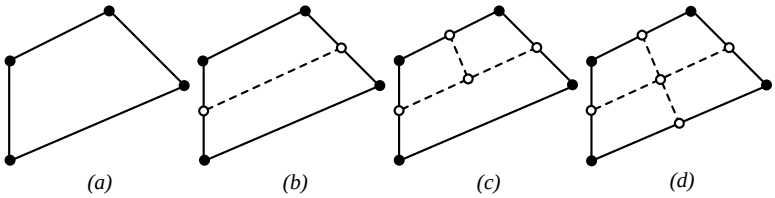

Figure 4.1. Creation of different number of smoothing domains (SDs) inside a quadrilateral element in the CS-FEM; (a) 1 SD (b) 2 SD (c) 3 SD (d) 4 SD

4.4 Node-Based Smoothed Finite Element Method (N-FEM)

In the NS-FEM settings, per each node *k* of the background mesh one smoothing domain Ω_k^s is created by sequentially connecting the mid-edge points to the central points of the elements surrounding node *k* as shown in Figure 4.2 for a typical n-sided polygonal base mesh. The boundary path Γ_k^s in the figure is formed by the lines *AB*, *BC*, *CD*, *DE*, *EF*, *FG*, *GH*, and *HA*.

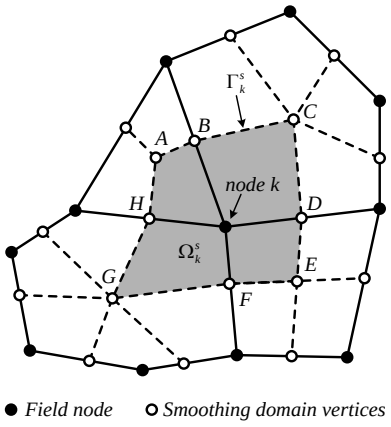

Figure 4.2. Creation of smoothing domain in the NS-FEM for a typical mesh of n-sided polygonal elements

4.5 Edge-Based Smoothed Finite Element Method (ES-FEM)

In the ES-FEM framework, per each edge k of the background element one smoothing domain Ω_k^s is constructed by connecting two endpoints of that edge to the central points of its adjacent elements as typically shown in Figure 4.3. Colored area in the figure shows the Ω_k^s with the boundary path Γ_k^s when edge *AC* is assigned as k^{th} edge. Γ_k^s is formed by sequent lines *AB*, *BC*, *CD* and *DA*.

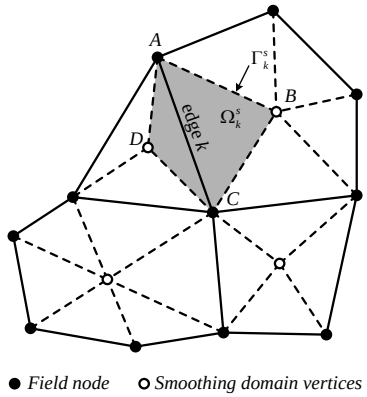

Figure 4.3. Creation of smoothing domain in the ES-FEM for a typical mesh of n-sided polygonal elements

4.6 Alpha-based Finite Element Method (Alpha-FEM)

The method of α-FEM is developed by a rational combination of upper bound behavior of NS-FEM and the lower bound behavior of standard FEM models with a scaling factor α using triangular and tetrahedral elements in 2-D and 3-D, respectively(α FEM-T3, α FEM-T4).

Figure 3.3 shows the schematic way of crating smoothing domains in the ES-FEM for a typical mesh of n-sided polygonal elements.

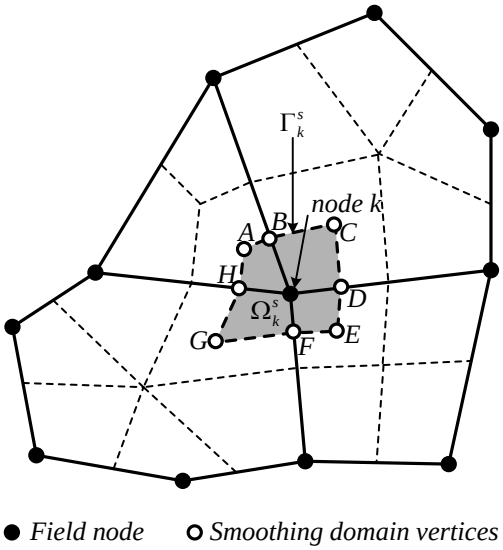

Figure 4.4. Creation of smoothing domain in the α FEM for a typical mesh of n-sided polygonal elements

Figure 4.5 also shows this scheme in more details for the case of 3-node triangular elements. As it can be seen in this figure, a fractional portion of each element is assumed as the smoothing domain associated with each node of the element, and the strain is then smoothed over this domain. The rest part of the element, however, is treated as the same way of standard FEM.

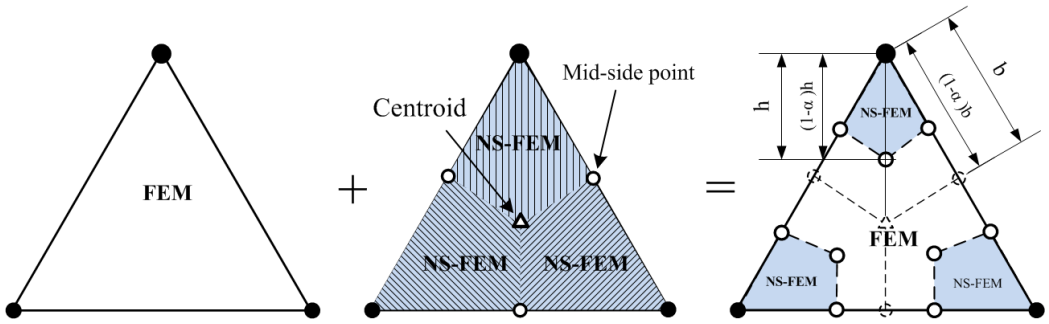

Figure 4.5. An α FEM-T3 element: combination of the triangular elements of FEM-T3 and NS-FEM-T3. The NS-FEM-T3 is used for three quadrilaterals sub-domain, and the FEM-T3 is used for the *Y*-shaped sub-domain in the center.

4.7 Faced-Based Smoothed Finite Element method (FS-FEM)

In the FS-FEM framework, per each element face *k* of the tetrahedral background mesh one smoothing domain Ω_k^s is constructed which can be created by connecting three field nodes of that face to the centers of the adjacent elements as shown in Figure 4.6. In this figure, the colored face *ABC* is the common face between two tetrahedrons *ABCD* and *ABCE* with the center points *G* and *H*, respectively. The volume of smoothing domain is created with the surfaces *ACG*, *CGB* and *BGA* from upper tetrahedron and *AHC*, *HCB* and *BAH* from lower tetrahedron.

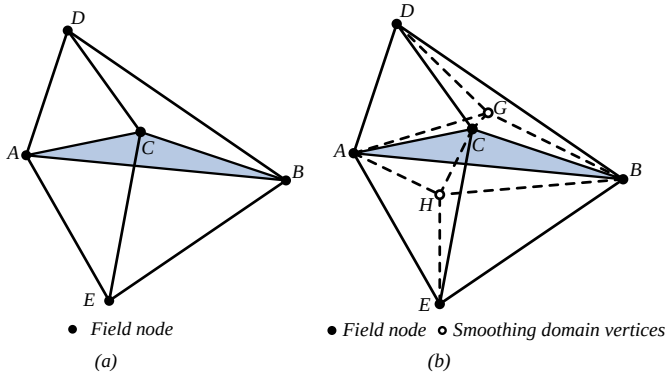

Figure 4.6. (a) Two typical tetrahedrons sharing a face (b) Creation of smoothing domain for a FS-FEM model

Chapter 5: Singular Edge-based Smoothed Finite Element Method (Singular ES-FEM) for the LEFM problems

"There's a way to do it better—find it."

Thomas Edison

5.1 Introduction

Several studies on the edge-based smoothed finite element method indicate that using the ES-FEM with triangular elements provides the more accurate results than those obtained from FEM with the quadrilateral elements [91] . Moreover, the displacement field is evaluated by a simple interpolation method and no mapping procedure is required, resulting in an improved computational efficiency. The method is stable and straightforward to be implemented. It only works properly for the domains containing no discontinuity, though. The main objective of introducing new technique of singular edge-based smoothed finite element method is to cope with deficiency of standard ES-FEM in analyzing discontinuous domains like the problems including cracks. A special type of triangular element is proposed to be used at the crack tip. The element is designed to be

compatible with the standard linear triangular element which is used at the rest of the domain. The strain smoothing technique is then implemented on the smoothing domains associated with edges of all elements including the proposed one. Finally, the strain gradient and stiffness matrix are accordingly computed, and the resultant system of equations is solved to get the nodal displacement values. The stress intensity factors can be also evaluated by adopting the method of interaction integral in the framework of singular ES-FEM.

5.2 Idea of singular ES-FEM for reproducing stress singularity at the crack tip

5.2.1 Displacement interpolation along the element edge

When a linear fracture mechanics problem is simulated using a numerical approach, the theoretical requirement of singular stress field near the crack tip should be justified. In the finite element method, the most widely used technique to simulate this kind of stress singularity is the so-called (quadratic) 6-node crack-tip element in which the mid-edge nodes are shifted by a quarter edge-lengths toward the crack-tip. The singularity is then achieved nicely by the well-known iso-parametric mapping procedure [94, 95].

In the present singular ES-FEM method, however, no mapping is needed and only the shape function values (not the derivatives) are required. Making use of this important feature of ES-FEM, the stress singularity at the crack tip can be created by a simple point interpolation method with extra basis functions of proper fractional order polynomials. Figure 5.1 shows an ES-FEM model for a fracture problem with a horizontal opening

crack. As it can be observed in the figure, the domain is discretized using two different types of triangular elements including the “new 5-node triangular elements” located at the crack tip (distinguished with the colored area), and the “standard 3-node triangular elements” typically used in the standard ES-FEM. The new 5-noded elements of present singular ES-FEM are simply generated by adding-in one additional node on each edge of standard 3-node triangular elements connected to the crack tip node, as shown in Figure 5.2.

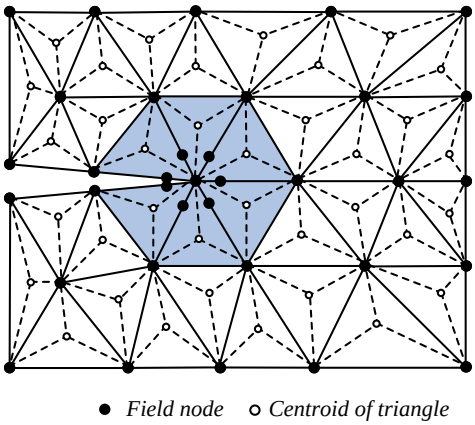

Figure 5.1. A singular ES-FEM model for domains including a crack

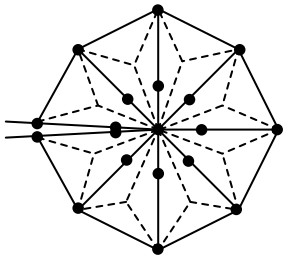

Figure 5.2. Node arrangement near the crack tip. Dash lines show the boundary of a smoothing domain for an edge directly connected to the crack tip node

Besides, in spite of FEM approach to produce the singularity by using the quarter-point elements, in the singular ES-FEM the location of added intermediate node can be in general at any point on the edge, as shown in Figure 5.3.

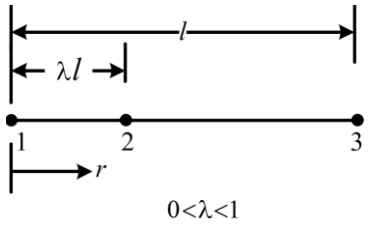

Figure 5.3. Coordinate for an edge connected to the crack-tip

Then, the displacement field, for example, the component *u*, at any point of interest on an edge directly connected to the crack tip is suggested to be approximated using:

$$u = c_0 + c_1 r + c_2 \sqrt{r} \tag{5.1}$$

Where *r* is the radial coordinate originated at the crack-tip (node 1 in Figure 5.3), and c_i ($i = 1,2,3$) are the constants yet to be determined. Clearly, the assumed displacement using equation (5.1) is at least linearly complete. Using equation (5.1), displacements at node 1, 2 and 3 can be expressed as:

$$u_1 = c_0 \quad ;(r = 0 \; at \; node \; 1) \tag{5.2}$$

$$u_2 = c_0 + c_1 \lambda l + c_2 \sqrt{\lambda l} \quad ;(r = \lambda l \; at \; node \; 2) \tag{5.3}$$

$$u_3 = c_0 + c_1 l + c_2 \sqrt{l} \quad ;(r = l \; at \; node \; 3) \tag{5.4}$$

Where u_i ($i = 1,2,3$) are the nodal displacements, *l* is the length of the element edge, and $\lambda \in (0 \quad 1)$ controls the location of node 2. Solving this simultaneous system of three equations (5.2)- (5.4) for c_i, we shall have:

$$\begin{cases} c_0 = u_1 \\ c_1 = \dfrac{1}{\lambda l}\left[\left(-1+\dfrac{(1-\lambda)\sqrt{\lambda l}}{\sqrt{\lambda l}-\lambda\sqrt{l}}\right)u_1 + (1-\dfrac{\sqrt{\lambda l}}{\sqrt{\lambda l}-\lambda\sqrt{l}})u_2 + \dfrac{\lambda\sqrt{\lambda l}}{\sqrt{\lambda l}-\lambda\sqrt{l}}u_3\right] \\ c_2 = \dfrac{1}{\sqrt{\lambda l}-\lambda\sqrt{l}}\left[(\lambda-1)u_1 + u_2 - \lambda u_3\right] \end{cases} \tag{5.5}$$

After substituting c_i ($i = 1,2,3$) back into Equation(5.1), we obtain:

$$u = \begin{Bmatrix} \underbrace{1+\dfrac{r}{\lambda l}(-1+\dfrac{(1-\lambda)\sqrt{\lambda l}}{\sqrt{\lambda l}-\lambda\sqrt{l}})+\dfrac{\sqrt{r}}{\sqrt{\lambda l}-\lambda\sqrt{l}}(\lambda-1)}_{\phi_1} \\ \underbrace{\dfrac{r}{\lambda l}\left(1-\dfrac{\sqrt{\lambda l}}{\sqrt{\lambda l}-\lambda\sqrt{l}}\right)+\dfrac{\sqrt{r}}{\sqrt{\lambda l}-\lambda\sqrt{l}}}_{\phi_2} \\ \underbrace{\dfrac{r}{\lambda l}\left(\dfrac{\lambda\sqrt{\lambda l}}{\sqrt{\lambda l}-\lambda\sqrt{l}}\right)-\dfrac{\lambda\sqrt{r}}{\sqrt{\lambda l}-\lambda\sqrt{l}}}_{\phi_3} \end{Bmatrix}^T \begin{Bmatrix} u_1 \\ u_2 \\ u_3 \end{Bmatrix} \tag{5.6}$$

where ϕ_i ($i = 1,2,3$) are the basis nodal shape functions for these three nodes on the edge connected to the crack tip and can be written in the following row-matrix form:

$$\Phi = \begin{Bmatrix} \underbrace{1+\dfrac{r}{\lambda l}\left(-1+\dfrac{(1-\lambda)\sqrt{\lambda l}}{\sqrt{\lambda l}-\lambda\sqrt{l}}\right)+\dfrac{\sqrt{r}}{\sqrt{\lambda l}-\lambda\sqrt{l}}(\lambda-1)}_{\phi_1} \\ \underbrace{\dfrac{r}{\lambda l}\left(1-\dfrac{\sqrt{\lambda l}}{\sqrt{\lambda l}-\lambda\sqrt{l}}\right)+\dfrac{\sqrt{r}}{\sqrt{\lambda l}-\lambda\sqrt{l}}}_{\phi_2} \\ \underbrace{\dfrac{r}{\lambda l}\left(\dfrac{\lambda\sqrt{\lambda l}}{\sqrt{\lambda l}-\lambda\sqrt{l}}\right)-\dfrac{\lambda\sqrt{r}}{\sqrt{\lambda l}-\lambda\sqrt{l}}}_{\phi_3} \end{Bmatrix}^T \tag{5.7}$$

In which

$$\begin{cases} \phi_1 = 1 + \dfrac{r}{\lambda l}\left(-1 + \dfrac{(1-\lambda)\sqrt{\lambda l}}{\sqrt{\lambda l} - \lambda\sqrt{l}} \right) + \dfrac{\sqrt{r}}{\sqrt{\lambda l} - \lambda\sqrt{l}}(\lambda - 1) \\ \phi_2 = \dfrac{r}{\lambda l}\left(1 - \dfrac{\sqrt{\lambda l}}{\sqrt{\lambda l} - \lambda\sqrt{l}} \right) + \dfrac{\sqrt{r}}{\sqrt{\lambda l} - \lambda\sqrt{l}} \\ \phi_3 = \dfrac{r}{\lambda l}\left(\dfrac{\lambda\sqrt{\lambda l}}{\sqrt{\lambda l} - \lambda\sqrt{l}} \right) - \dfrac{\lambda\sqrt{r}}{\sqrt{\lambda l} - \lambda\sqrt{l}} \end{cases} \tag{5.8}$$

It is clear that the shape functions are (complete) linear in *r* and "enriched" with $\sqrt{r}$ that is capable of producing a strain (hence stress) singularity field of an order of ½ near the crack-tip, because the strain is evaluated from the derivatives of the assumed displacements. Note also that in this formulation the intermediate edge node can be at any position on the edge controlled by factor λ, which is very general and different from the usual FEM crack tip elements where the intermediate nodes are located at a quarter of lengths to the crack tip. Moreover, the usual FEM crack tip element achieves the singularity by coordinate mapping, while the singular ES-FEM achieves the singularity via direct interpolation with a proper fractional order basis term and without demanding any mapping procedure.

5.2.2 Displacement interpolation within a crack-tip element

As it was mentioned before, in the present ES-FEM, we use a base mesh of 3-node linear triangle elements for areas without singularity, and one layer of the specially designed singular 5-node triangular elements containing the crack-tip to produce the desired stress singularity behavior at the crack tip, as shown in Figure 5.1. The same procedure described in section 5.2.1 can be properly implemented within a crack-tip

element by using the basic nodal shape functions derived in Equation (5.8) for a one-dimensional element.

We first assume that in the radial directions originated from the crack tip, the displacements vary in the same fashion as given in equation (5.1). In the tangential direction, however, it is assumed to vary linearly. This assumption ensures the compatibility along the edges which are common between the 3-node linear triangular elements and the 5-node crack tip elements. Figure 5.4 shows two 5-node elements, parts of which form one edge-based smoothing domain.

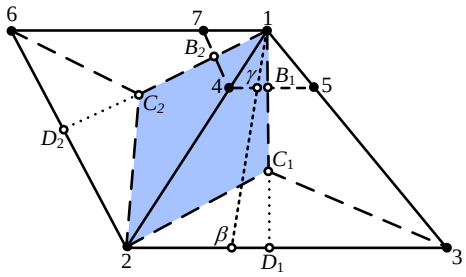

Figure 5.4 . Two 5-node elements connected to the crack tip node 1(colored area shows the smoothing domain associated with edge 1-4-2)

Points D_1 and B_1 in this figure are, respectively, the midpoints of lines 2-3 and 4-5. The displacements at these two points can be evaluated simply by averaging (because of linear variation assumption on the tangential direction):

$$u_{B_1} = \frac{1}{2}(u_4 + u_5) \tag{5.9}$$

$$u_{D_1} = \frac{1}{2}(u_2 + u_3) \tag{5.10}$$

At any point on the line $1-B_1-D_1$ displacement is then evaluated using the shape functions for edges given in equation (5.8):

$$u = u_1\phi_1 + u_{B_1}\phi_2 + u_{D_1}\phi_3 \tag{5.11}$$

Substituting Equations (5.9) and (5.10) into equation (5.11), we have:

$$u = u_1\phi_1 + \frac{1}{2}(u_4 + u_5)\phi_2 + \frac{1}{2}(u_2 + u_3)\phi_3 \tag{5.12}$$

Hence, the interpolation at any point on line $1-B_1-D_1$ can be given as follows:

$$u = u_1\phi_1 + \frac{1}{2}\phi_3 u_2 + \frac{1}{2}\phi_3 u_3 + \frac{1}{2}\phi_2 u_4 + \frac{1}{2}\phi_2 u_5 \tag{5.13}$$

Similarly, at any point on line 1-γ-β (see, Figure 5.4), the displacement can be calculated as

$$u = u_1\phi_1 + u_\gamma\phi_2 + u_\beta\phi_3 \tag{5.14}$$

where

$$u_\gamma = \left(1 - \frac{l_{\gamma-4}}{l_{4-5}}\right)u_4 + \frac{l_{\gamma-4}}{l_{4-5}}u_5 \tag{5.15}$$

$$u_\beta = \left(1 - \frac{l_{\beta-2}}{l_{2-3}}\right)u_2 + \frac{l_{\beta-2}}{l_{2-3}}u_3 \tag{5.16}$$

in which l_{i-j} is the distance between points *i* and *j*. Because of the simple fact that $\frac{l_{\gamma-4}}{l_{4-5}} = \frac{l_{\beta-2}}{l_{2-3}} = \alpha$, we finally arrive at

$$u = \underbrace{\phi_1}_{N_1} u_1 + \underbrace{(1-\alpha)\phi_3}_{N_2} u_2 + \underbrace{\alpha\phi_3}_{N_3} u_3 + \underbrace{(1-\alpha)\phi_2}_{N_4} u_4 + \underbrace{\alpha\phi_2}_{N_5} u_5 \tag{5.17}$$

The general form of the nodal shape functions for the interpolation at any point within the 5-node crack-tip element can then be written as:

$$\begin{cases} N_1 = 1+\dfrac{r}{\lambda l}\left(-1+\dfrac{(1-\lambda)\sqrt{\lambda l}}{\sqrt{\lambda l}-\lambda\sqrt{l}}\right)+\dfrac{\sqrt{r}}{\sqrt{\lambda l}-\lambda\sqrt{l}}(\lambda-1) \\ N_2 = (1-\alpha)\left(\dfrac{r}{\lambda l}\left(\dfrac{\lambda\sqrt{\lambda l}}{\sqrt{\lambda l}-\lambda\sqrt{l}}\right)-\dfrac{\lambda\sqrt{r}}{\sqrt{\lambda l}-\lambda\sqrt{l}}\right) \\ N_3 = \alpha\left(\dfrac{r}{\lambda l}\left(\dfrac{\lambda\sqrt{\lambda l}}{\sqrt{\lambda l}-\lambda\sqrt{l}}\right)-\dfrac{\lambda\sqrt{r}}{\sqrt{\lambda l}-\lambda\sqrt{l}}\right) \\ N_4 = (1-\alpha)\left(\dfrac{r}{\lambda l}\left(1-\dfrac{\sqrt{\lambda l}}{\sqrt{\lambda l}-\lambda\sqrt{l}}\right)+\dfrac{\sqrt{r}}{\sqrt{\lambda l}-\lambda\sqrt{l}}\right) \\ N_5 = \alpha\left(\dfrac{r}{\lambda l}\left(1-\dfrac{\sqrt{\lambda l}}{\sqrt{\lambda l}-\lambda\sqrt{l}}\right)+\dfrac{\sqrt{r}}{\sqrt{\lambda l}-\lambda\sqrt{l}}\right) \end{cases} \tag{5.18}$$

Because in our singular ES-FEM, we do not need derivatives of shape functions, Equation (5.18) is all we need in computing the stiffness matrix for creating our numerical model.

If the location parameter of λ is set to $\lambda = 1/4$ to have the most similarity with the FEM quarter-point elements, the shape functions for the one-dimensional element shown in figure Figure 5.2 will be reduced to

$$\begin{cases} \phi_1 = 1+2\dfrac{r}{l}-3\sqrt{\dfrac{r}{l}} \\ \phi_2 = -4\dfrac{r}{l}+4\sqrt{\dfrac{r}{l}} \\ \phi_3 = \dfrac{2r}{l}-\sqrt{\dfrac{r}{l}} \end{cases} \tag{5.19}$$

Resulting in the following statements for the shape functions of two dimensional 5-node crack tip element

$$\begin{cases} N_1 = \phi_1 \\ N_2 = (1-\alpha)\phi_3 \\ N_3 = \alpha\phi_3 \\ N_4 = (1-\alpha)\phi_2 \\ N_5 = \alpha\phi_2 \end{cases} \tag{5.20}$$

5.2.3 Creation of smoothing domains in the singular ES-FEM

In order to calculate the stiffness matrix in the present ES-FEM, strain smoothing domains are constructed associated with the edges of each element. Each 3-node triangular element is divided into three sub-triangular areas corresponding to three edges of the triangle and two such sub-triangular areas sharing the same edge form a smoothing domain (SD) associated with that edge. A similar procedure is also used to create smoothing domains for the crack tip elements. For these elements, however, more domains can be constructed. Figure 5.5 shows three cases of one, two and three domains per edge for a typical 5-node crack-tip element. Based on the way that strain gradient matrix and stiffness matrix are calculated, these domains act as different smoothing domains or as sub-domains of the main smoothing domain (Let call them, sub-smoothing domains (S-SDs)). Later we will mention that how smoothing domains are numerically different from sub-smoothing domains. In the numerical example section, we will also show that increasing the number of smoothing domains will not improve the accuracy of results while the use of proper number of sub-smoothing domains might yield in better results.

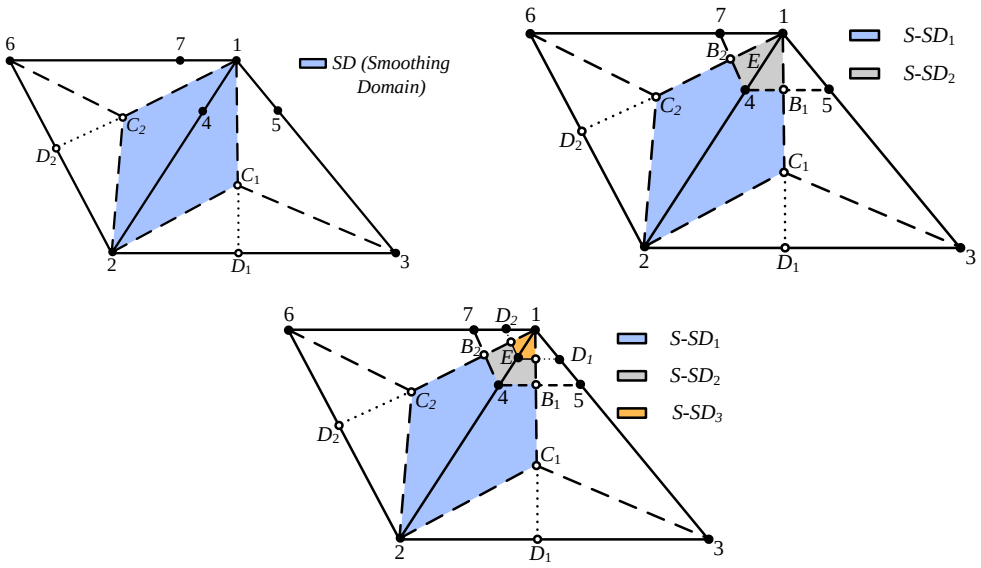

Figure 5.5. Dividing the smoothing domain associated with edge 1-4-2 into smaller domains. For crack tip edges, we may use SD=1 or 2 or 3. For other edges, we use SD=1.

5.3 Stiffness matrix evaluation

As it was mentioned earlier; in the ES-FEM procedure, the stiffness matrix of the whole model is the summation of the sub-matrixes of the stiffness matrix associated with all the strain smoothing domains.

$$\overline{\mathbf{K}}_{IJ} = \sum_{k=1}^{N_s} \overline{\mathbf{K}}_{IJ,k} \tag{5.21}$$

Where $\bar{\mathbf{K}}_{IJ}$ is the assembled stiffness matrix and $\bar{\mathbf{K}}_{IJ,k}$ is the stiffness matrix of the smoothing domain corresponding to edge *k* and is calculated by

$$\bar{\mathbf{K}}_{IJ,k} = \int_{A_k^s} \bar{\mathbf{B}}_I^T \mathbf{D} \bar{\mathbf{B}}_J \mathrm{dA} \tag{5.22}$$

In which A_k^s is the k^{th} strain smoothing area associated with edge *k*. $\bar{\mathbf{B}}_I$ can be calculated using

$$\bar{\mathbf{B}}_I(x_k) = \begin{bmatrix} \bar{b}_{Ix}(x_k) & 0 \\ 0 & \bar{b}_{Iy}(x_k) \\ \bar{b}_{Iy}(x_k) & \bar{b}_{Ix}(x_k) \end{bmatrix} \tag{5.23}$$

Where

$$\bar{b}_{Ih}(x_k) = \frac{1}{A_k^s} \int_{\Gamma_k^s} N_I(x) n_h^k(x) d\Gamma \quad ; (h = x, y) \tag{5.24}$$

In which N_I is the I^{th} shape function of the element, Γ_k^s is the integration domain and n_h^k is the h^{th} component of the outward normal vector matrix on the boundary Γ_k^s.

For the standard 3-node triangular elements with the linear shape functions, the entries of matrix $\bar{\mathbf{B}}_I$ are constants and the relation (5.22) is reduced to

$$\bar{\mathbf{K}}_{IJ(k)} = A_k^s \bar{\mathbf{B}}_I^T \mathbf{D} \bar{\mathbf{B}}_J \tag{5.25}$$

Also equation (5.24) can be numerically calculated by

$$\bar{b}_{Ih}(x_k) = \frac{1}{A_k^s} \sum_{i=1}^{M} \sum_{j=1}^{N_{GP}} N_I(x_{i,j}^{GP}) w_{i,j}^{GP} n_{ih}^k \quad ; (h = x, y) \tag{5.26}$$

Where M is the number of (line) boundary segments of Γ_k^s, $x_{i,j}^{GP}$ is the Gaussian point location on the i$^{\text{th}}$ boundary segment, $w_{i,j}^{GP}$ is the Gaussian weight associated with the Gaussian point $x_{i,j}^{GP}$, N_{GP} is the number of Gaussian points on the i^{th} boundary segment, and n_{ih}^k is the h^{th} component of the unit outward vector on the i^{th} boundary segment.

It should be noticed that for the boundary segments associated with the standard 3-node triangular elements, one Gaussian point at the midpoint of the (line) boundary

segment is sufficient, due to the linear interpolation used. For a 5-node crack tip element, however, more Gaussian points should be used, because the shape functions are no longer linear on the segment.

5.4 Increasing the number of smoothing domains associated with the edges directly connected to crack tip

The numerical approach for calculating stiffness matrix in this case is, in general, very similar to what has been explained in the previous part, except in some details. The stiffness matrix associated with those edges which are directly connected to the crack tip can be calculated by

$$\bar{\mathbf{K}}_{IJ,k} = \sum_{z=1}^{N_{sd,eg}} \bar{\mathbf{K}}^{z}_{IJ,k} \tag{5.27}$$

Where $N_{sd,eg}$ is the number of smoothing domains per edge k and $\bar{\mathbf{K}}^{z}_{IJ,k}$ is the stiffness matrix of z^{th} smoothing domain associated with the edge k and is calculated by

$$\bar{\mathbf{K}}^{z}_{IJ,k} = \int_{A_k^{s,z}} \bar{\mathbf{B}}_I^{z\,T} \mathbf{D} \bar{\mathbf{B}}^{z}_J \mathrm{dA} \tag{5.28}$$

In which $A_k^{s,z}$ is z^{th} strain smoothing area associated with edge k and $\bar{\mathbf{B}}^{z}_I$ can be calculated using

$$\bar{\mathbf{B}}^{z}_I(x_k) = \begin{bmatrix} \bar{b}^{z}_{Ix}(x_k) & 0 \\ 0 & \bar{b}^{z}_{Iy}(x_k) \\ \bar{b}^{z}_{Iy}(x_k) & \bar{b}^{z}_{Ix}(x_k) \end{bmatrix} \tag{5.29}$$

Where

$$\bar{b}_{Ih}^{z}(x_k)=\frac{1}{A_k^{s,z}}\int_{\Gamma_k^{s,z}} N_I(x)n_h^{k,z}(x)d\Gamma \quad ;(h=x,y) \tag{5.30}$$

In this equation $\Gamma_k^{s,z}$ is the boundary of z^{th} smoothing domain of the edge k and $n_h^{k,z}$ is the h^{th} component of the outward normal vector matrix on the boundary $\Gamma_k^{s,z}$.

5.5 Increasing the number of sub-smoothing domains associated with the edges directly connected to crack tip

In this case, only one smoothing domain is created associated with each edge. In order to get a better capture of singular field, however, more partitions are made in the domains corresponding to the crack tip edges by dividing the main SD into more S-SDs. In this case the calculation can be performed as follows. The stiffness matrix of the whole model can be still obtained using equation (5.21) and (5.22). However, the strain matrix of the smoothing domain $\bar{\mathbf{B}}_I$ is calculated by taking average of the strain matrices of S-SDs.

$$\bar{\mathbf{B}}_I=\frac{1}{A_s}\sum_{a=1}^{N_{s-sd,egk}} A_s^a\bar{\mathbf{B}}_I^a \tag{5.31}$$

In which $N_{s-sd,egk}$ is the number of sub-smoothing domains per edge k and $\bar{\mathbf{B}}_I^a$ is the strain matrix of the a^{th} sub-smoothing domain associated with the edge k.

$$\bar{\mathbf{B}}_I^a(x_k)=\begin{bmatrix}\bar{b}_{Ix}^a(x_k) & 0\\ 0 & \bar{b}_{Iy}^a(x_k)\\ \bar{b}_{Iy}^a(x_k) & \bar{b}_{Ix}^a(x_k)\end{bmatrix} \tag{5.32}$$

Where

$$\bar{b}_{Ih}^{a}(x_k) = \frac{1}{A_k^{s,a}} \int_{\Gamma_k^{s,a}} N_I(x) n_h^{k,a}(x) d\Gamma \quad ;(h = x, y) \tag{5.33}$$

In which $A_k^{s,a}$ is the a^{th} sub-smoothing domain area associated with the edge *k*, $\Gamma_k^{s,a}$ is the boundary of a^{th} sub-smoothing domain of the same edge and $n_h^{k,a}$ is the h^{th} component of the outward normal vector matrix on the boundary $\Gamma_k^{s,a}$.

Using this approach will help us to represent the strain value of each smoothing domain as the average value of the strains corresponding to the sub-smoothing domains. In the section of numerical examples it will be seen that this procedure yields a better capture of singular stress field.

5.6 Determination of area-path for the interaction integral calculation

As it was mentioned in chapter 2, for a proper characterization of crack behavior, it is firstly required to evaluate the stress intensity factor (SIF) parameters. Using the domain form of interaction integral, SIFs can be easily derived from the J-integral parameter and through an energy-based method. To this end, an area-path A_J needs to be assigned to the domain over which the integral is calculated.

Because our numerical method of ES-FEM uses a base mesh of linear 3-node triangular elements, a simple scheme can be devised to determine the area-path A_J as shown in Figure 5.6. First, a set of elements having at least one node within a circle of radius r_d is found, and this element set is denoted as N_d. The weighting function q used in the area-path interaction integral (2.24) is then chosen as a piece wisely linear function passing through the nodal values at all the nodes belonging to all the elements in N_d. If a

node n_i belonging to an element $e \in N_d$ lies outside the circle, then the nodal value of the weighting function is set to zero: $q_i = 0$; if a node n_i lies inside the circle, however, the weighting function is set to unit: $q_i = 1$. Since the elements set N_d^{in} has all the nodes inside the circle as shown in Figure 5.6, the weight function will be a constant (unit) within all these elements in set N_d^{in}. Because the gradient of q is used in equation (2.24) , the element set N_d^{in} will contribute nothing to the interaction integral. The non-zero contribution to the integral is obtained only for elements set N_d^{eff} with (two) edges intersecting the circle. Because 3-node elements are used in ES-FEM, any circle will naturally always select a layer of elements that form A_J .

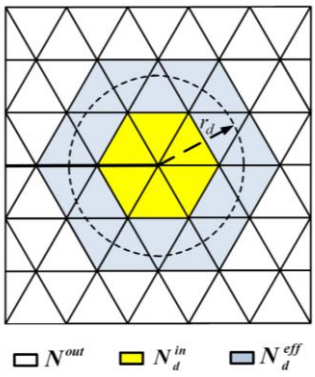

Figure 5.6. A typical method to select the area-path for the interaction integral

5.7 Numerical Examples

In this section some examples are presented to demonstrate the properties of singular ES-FEM for 2-D fracture problems. For comparison, the problems are also analyzed using the FEM with or without 6-node crack tip elements. Moreover, to show the improvements of the method in comparison with standard ES-FEM, the examples were

solved using the ES-FEM (T3) without the present 5-node crack tip elements. The first example is thoroughly analyzed to examine the effect of different number of smoothing domains and sub-smoothing domains on the results accuracy. In addition, a computational efficiency study and a convergence study is conducted for first and fourth example, respectively, to show how computationally efficient and numerically accurate singular ES-FEM is in comparison with other methods. For the stress intensity factor evaluation, the interaction integral method is used and the numerically path independency feature of results is investigated for the mixed mode problems. The reference solution in all the examples has been obtained using the singular FEM with the degrees of freedom that is 20 times the greatest DOF in the numerical analysis.

5.7.1 Rectangular plate with an edge crack under tension

A rectangular plate with an edge crack under tension load has been studied as a benchmark. The plate is assumed to have a unit thickness so that plane stress condition is valid. The rectangular plate has the length of 8*mm* and the width of 4*mm*, and the length of sharp crack at the edge is 0.5*mm*. The bottom edge is fixed while the other edge is subjected to the tension stress of $100\,N/mm^2$. This structure has been shown in Figure 5.7. The solution in terms of strain energy and displacement has been computed using *SD*=1, 2, 3, 4 and *S-SD*=1, 2, 3, 4 for the edges directly connected to the crack tip. The results of strain energy and displacement are plotted in Figure 5.8 and Figure 5.9, respectively.

The computational time at different degrees of freedom has been also recorded and a comparison of the computational efficiency in terms of error in the energy norm has also conducted. The result has been depicted in Figure 5.10.

The horizontal axis in this log-log plot is associated with the computational time, while the vertical axis expresses the error norm of strain energy e_e calculated using the following relation

$$e_e = \left| E_{num} - E_{Re} \right|^{1/2} \tag{5.34}$$

Where E_{num} is the numerical strain energy, and E_{Re} is the reference strain energy.

By considering a horizontal line in this plot and fixing the amount of error, it can be observed that different methods cross the line at different values of computational time; among which singular ES-FEM takes the smallest value; meaning that this method is the fastest one in reaching a certain amount of accuracy.

Likewise; at a fixed computational time, different methods produce different values of error norm in the strain energy, among which singular ES-FEM provides the smallest value; meaning that the method is able to offer the most accurate results at a certain computational time.

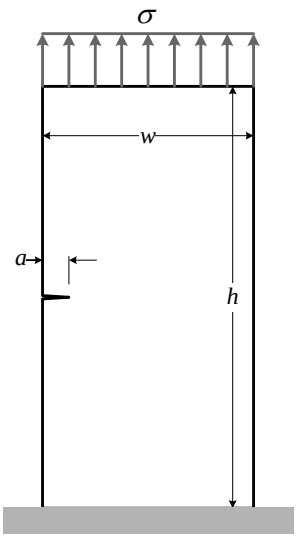

Figure 5.7. Plate with an edge crack under a tension load

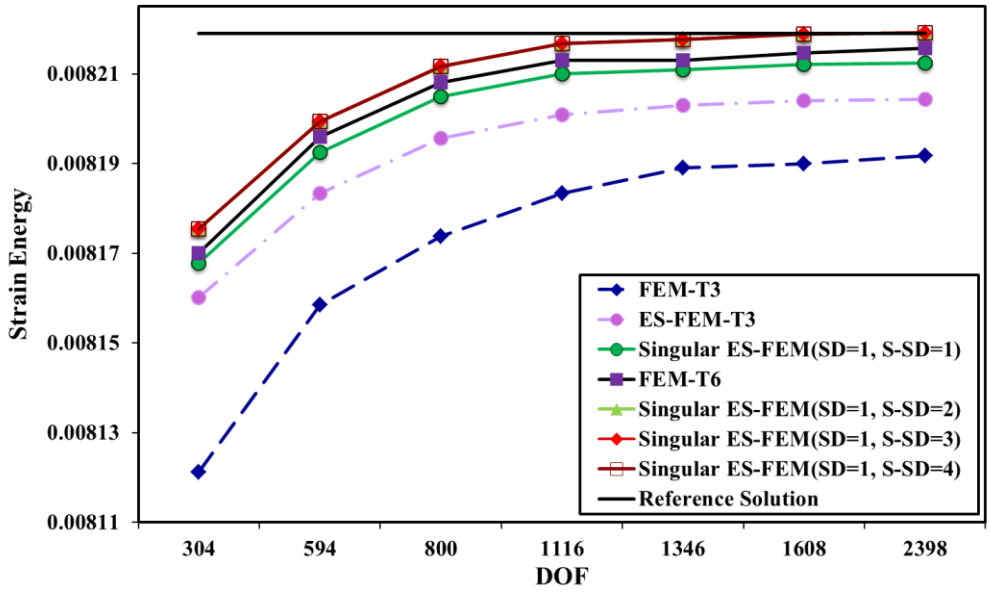

(*a*)

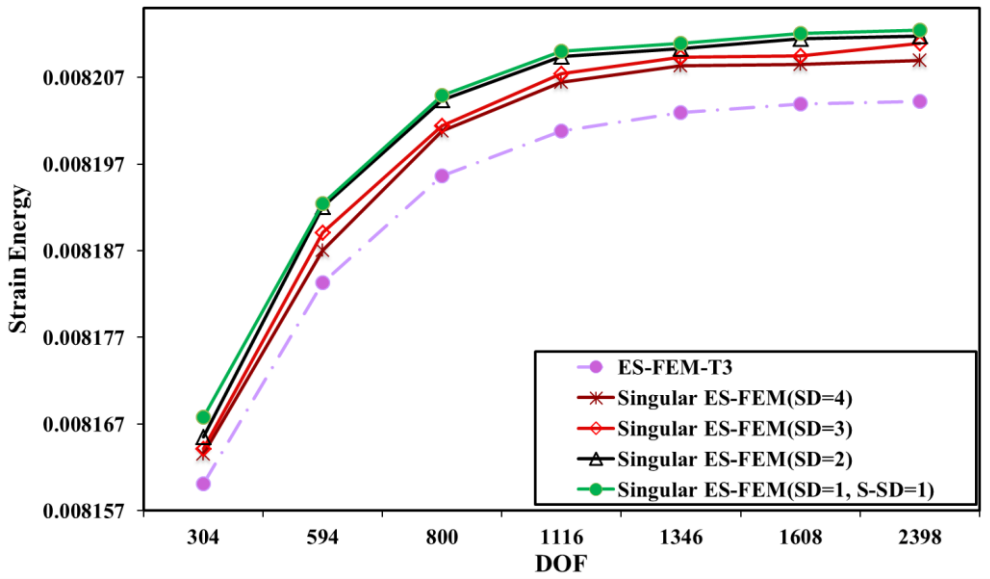

(*b*)

Figure 5.8. Strain energy for the rectangular plate with an edge crack computed using different methods

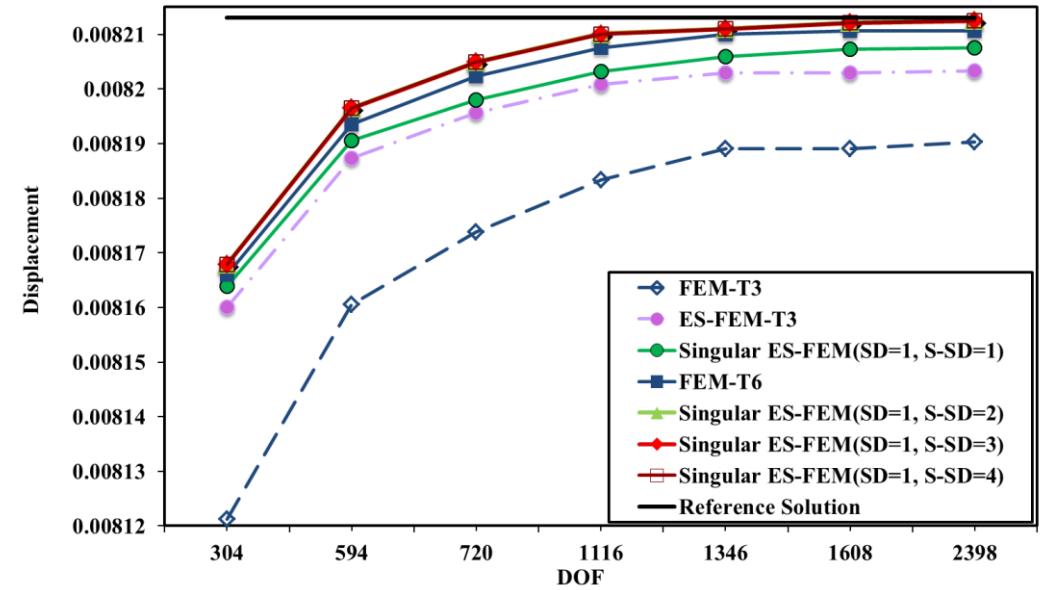

(*a*)

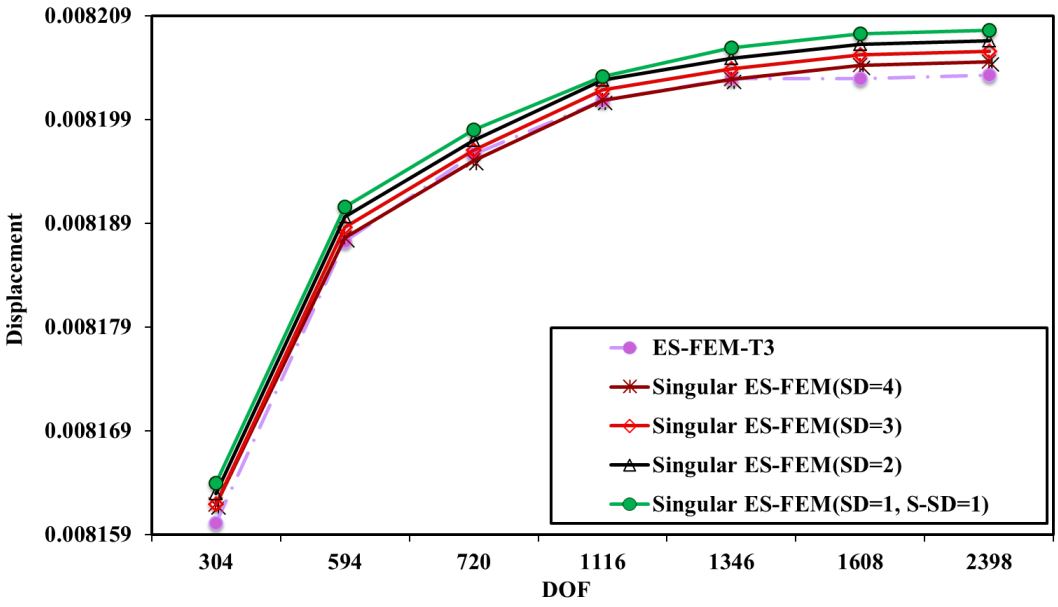

(*b*)

Figure 5.9. Displacements for the rectangular plate with an edge crack computed using different methods

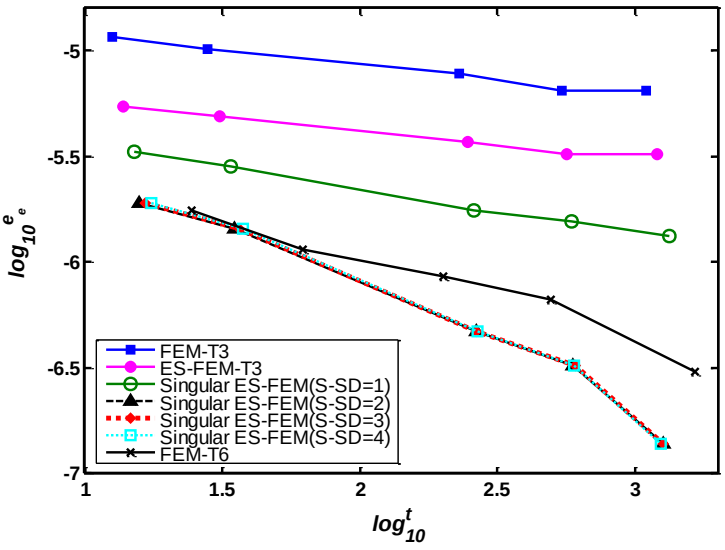

Figure 5.10. Computational efficiency in the norm of energy

From these results it can be seen clearly that

1) the results of the present singular ES-FEM with *SD*=1 at each crack tip edge are much more accurate and convergence much faster than the FEM-T3 and standard ES-FEM;

2) By dividing the smoothing domains at the crack tip into some other sub-smoothing domains (e.g. 2, 3 or 4) the results can be further improved; however, increasing the number of smoothing domains from one to 2, 3 or 4 strain smoothing domains (only for the crack tip elements) makes the model stiffer and the results do not improved

3) When *S-SD*=2 the results are more accurate and converge much faster not only than FEM-T3 and ES-FEM, but also than the FEM-T6 with standard crack tip elements;

4) Based on the comparison conducted among different methods, it can be clearly recognized that the singular ES-FEM with more than one sub-smoothing domain produces higher computational efficiency than FEM-T3, ES-FEM and even FEM-T6 with the crack tip elements. In the other word, singular ES-FEM with $S-SD \geq 2$ is faster in reaching the more accurate results.

5) It can be also observed that there is no significant change in the results when $S-SD \geq 2$ for the each crack tip edges. We therefore recommend the use of $S-SD=2$ in the present singular ES-FEM.

5.7.2 Compact tension specimen

A compact tension specimen with initial crack length a=13.7 *mm* and width w=23.5 *mm* is now analyzed using the singular ES-FEM. Specimen has the elasticity module of $E=2\times10^7\ MPa$ and Poisson's ratio $\nu=0.3$. The diameter of each hole is 1*mm* and the concentrated load is applied to the specimen at the points shown in Figure 5.11. The problem is solved using FEM-T3, FEM-T6 and standard ES-FEM and the results in terms of the strain energy and displacement have been plotted in Figure 5.12 and Figure 5.13, respectively.

The findings from this problem are similar to the findings from the previous example, which reinforces our claims. Our singular ES-FEM with more than 2 sub-smoothing domains presents the best results among all the other methods and even the quadratic FEM with 6-node crack tip elements.

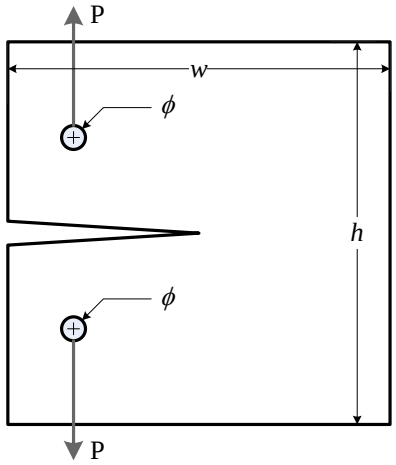

Figure 5.11. Compact tension specimen

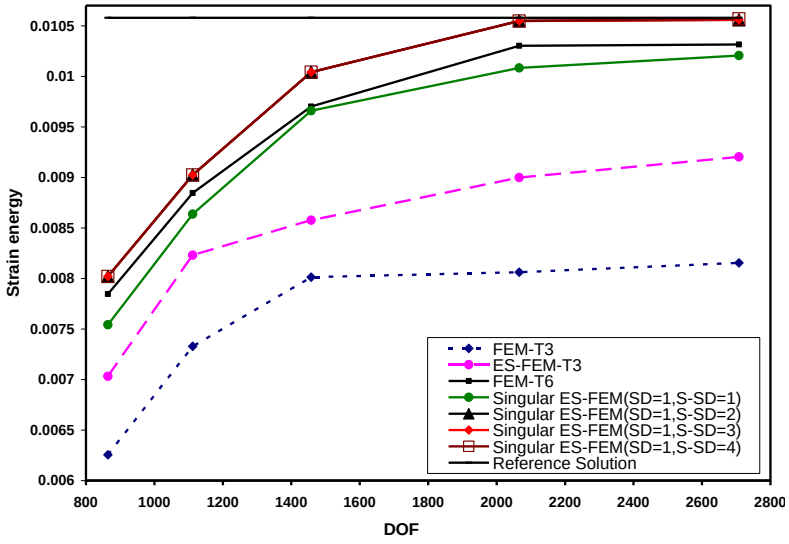

Figure 5.12. Strain energy for the compact tension specimen computed using different methods

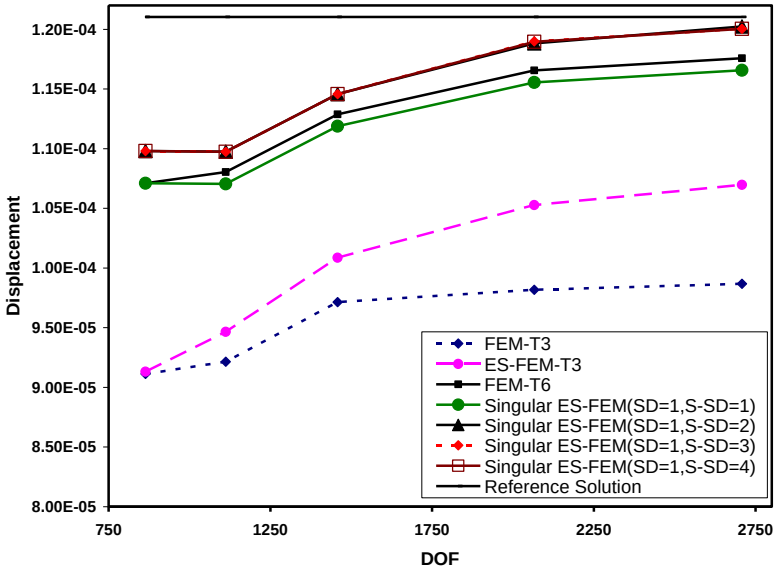

Figure 5.13. Displacement for the compact tension specimen computed using different methods

5.7.3 Double cantilever beam

In this example a double cantilever beam under tension load has been studied. The geometry of the model is shown in Figure 5.14. The plane stress condition is assumed with elastic modulus $E = 2\times10^7\ MPa$ and Poisson's ratio $\nu = 0.3$. The length of the sharp crack is 2*mm*, and the specimen is subjected to the tension load of 10 *N*. The results in term of strain energy are shown in Figure 5.15. The findings from this problem are similar to the findings for the previous two examples, which reinforce again our claims.

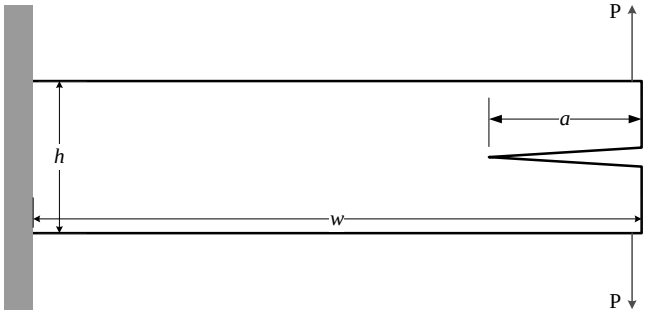

Figure 5.14. Cantilever beam with an edge crack under tension

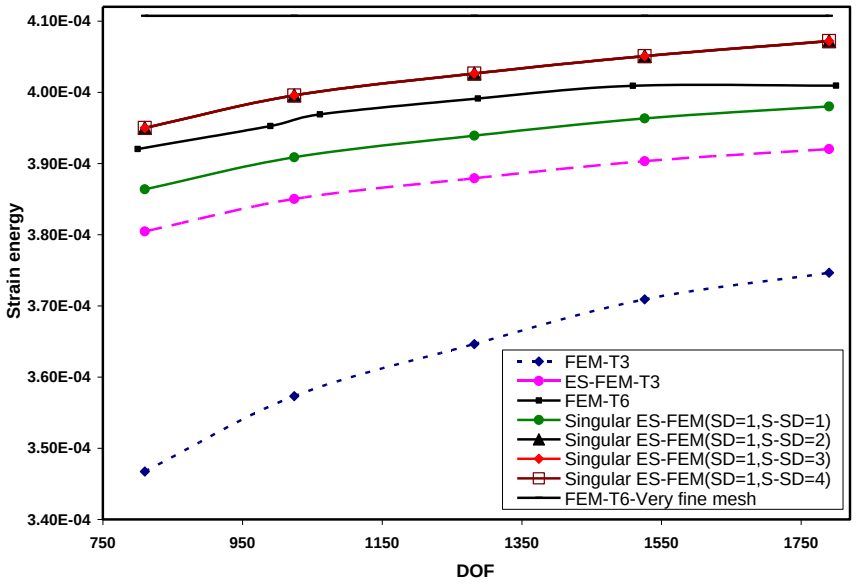

Figure 5.15. Strain energy for the cantilever beam computed using different methods

5.7.4 Rectangular finite plate with a central crack under pure mode I

A rectangular finite plate containing a central crack is analyzed under tension load at its top edge. This problem is of pure mode I. the structure is depicted in Figure 5.16, and the parameters used are $w=10.0\ cm$, $L=25.0\ cm$, $a=4cm$ and $\sigma=1N/cm^2$. The material is isotropic elastic and material constants are $E=3\times10^7\ N/cm^2$ and $\nu=0.25$. The analytical solution of stress intensity factors for such a structure is given by Tada et al. [96];

$$K_I=\sigma\sqrt{\pi a}\left[1-0.025(\frac{a}{w})^2-0.06(\frac{a}{w})^4\right](\sec(\frac{\pi a}{2w}))^{0.5} \tag{5.35}$$

The problem is then solved using FEM-T3, ES-FEM, FEM-T6, and the present singular ES-FEM. In the singular ES-FEM, one smoothing domain (*SD=1*) and two cases of one and two sub-smoothing domains (*S-SD=1* & *S-SD=2*) for the crack tip elements is

used. In addition, for the case of using two sub-smoothing domains, the effects of intermediate node position on the crack tip edges have been examined by choosing different values of λ.

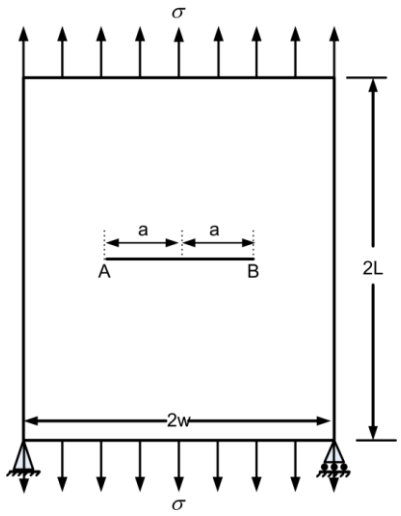

Figure 5.16. Homogenous finite plate with a central crack under tension (pure mode I)

The results in terms of the relative error of both strain energy and stress intensity factors have been illustrated in Figure 5.17, Figure 5.18, and Figure 5.19. In these figures *h* indicates the element size. In addition, the error norm of energy e_e and the error norm of stress intensity factor e_{K_I} are, respectively, calculated by the following formula;

$$e_e = \left| E_{num} - E_{\mathrm{Re}f} \right|^{1/2} \quad , \quad e_{K_I} = \left| \frac{(K_I)_{num} - (K_I)_{\mathrm{Re}f}}{(K_I)_{\mathrm{Re}f}} \right|^{1/2} \tag{5.36}$$

Where E_{num} and $(K_I)_{num}$ are, respectively, the strain energy and stress intensity factor obtained using the numerical method and similarly, $E_{\mathrm{Re}f}$ and $(K_I)_{\mathrm{Re}f}$ are those of reference solution.

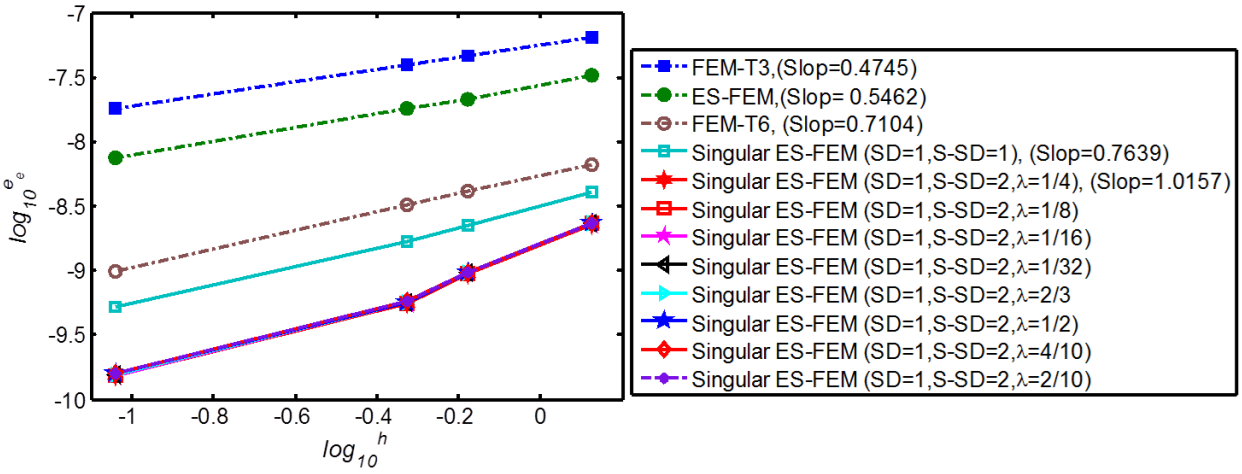

Figure 5.17. Strain energy results for the finite plate under mode I

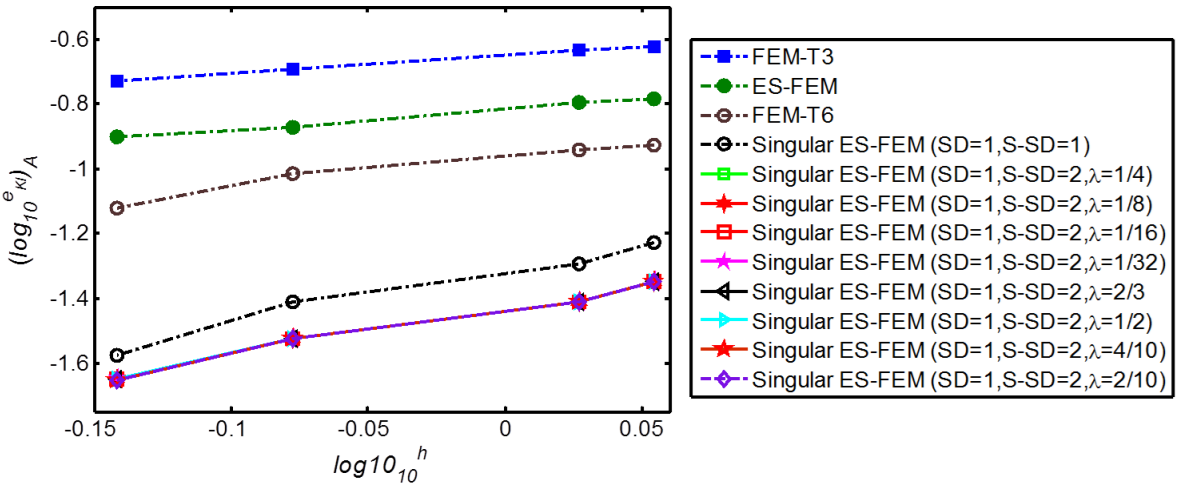

Figure 5.18. Error norm of stress intensity factor at point A for the finite plate under mode I

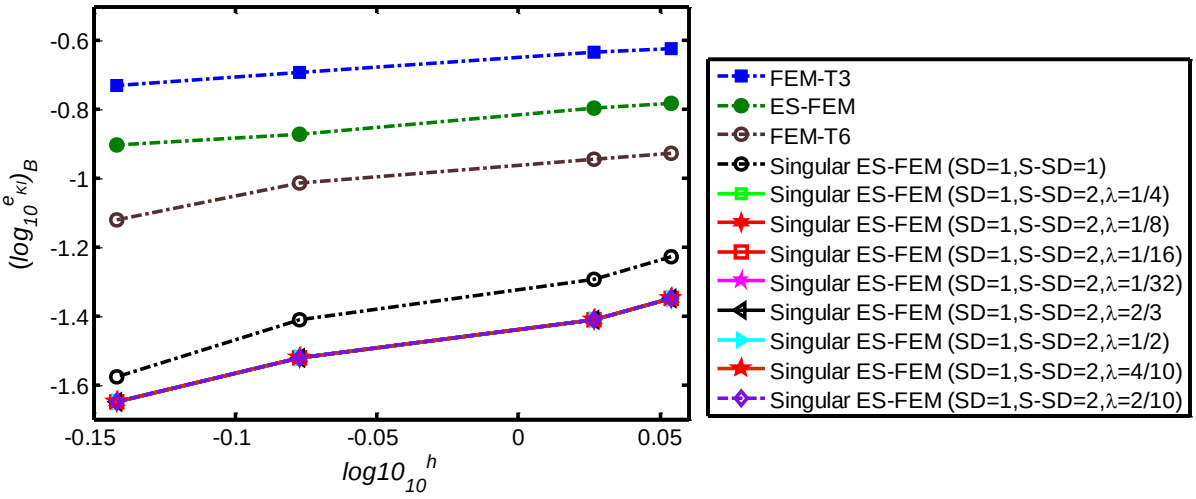

Figure 5.19. Error norm of stress intensity factor at point B for the finite plate under mode I

From these results it can be highlighted that:

1) The results of the singular ES-FEM are almost the same for different values of λ which is the parameter for the intermediate node position on the edges directly connected to the crack tip. Despite of the singular FEM in which strain singularity is generated by setting $\lambda = 1/4$ and using the iso-parametric mapping procedure, our method is independent of the parameter λ. A simple interpolation method is adopted in the present method to produce the singularity with no use of mapping implementation.

2) The results of the singular ES-FEM are more accurate than those obtained from the other methods including FEM-T6. At a mesh size of $h = 1$ the results in terms of the strain energy are about 1.7 times more accurate than FEM-T6 with the singular quarter point elements. At the same mesh, the findings of the stress intensity factors also show that singular ES-FEM yields the results which are about 2.8 times more accurate than FEM-T6.

3) The results in terms of the strain energy also show that our method provides a higher convergence rate compared to all the other methods including FEM-T6. Using just one S-SD can yield the convergence rate of 0.7639 which is more than the peer value from FEM-T6. Increasing the number of S-SD to two can increase the convergence rate to 1.0157 which is greater than the value for FEM-T6.

4) It can be observed from the results that by increasing the number of S-SDs from one to two the accuracy of results will increase and the relative error decreases. It also provides a higher convergence rate.

5) A comparison between Figure 5.18 and Figure 5.19 reveals that the value of stress intensity factors and related numerical error at crack tips A and B are very close to each other and almost identical. This expected result confirms that our method works very well for the domains including more than one crack.

5.7.5 Homogeneous infinite plate with a central crack under pure mode II

In this example, we study the homogeneous infinite plate with the similar geometry but under the pure shear mode. This structure has been shown in Figure 5.20. The analytical solution for this plate when its dimensions go to infinity is available and the stress intensity factor in mode II equals to $K_{II} = \tau\sqrt{\pi a}$, in which τ is the shear stress and a is the crack length. In this example the plate dimensions has been fixed to $a = 10mm$ and $w = 200mm$, and since $w/a = 20$, the solution for the infinite plate with a central crack can be valid. The problem has been solved under pure shear mode using

different methods including FEM-T3, ES-FEM and singular ES-FEM. The results in term of strain energy and stress intensity factor have been tabulated in Table 5.1, Table 5.2 and Table 5.3, and depicted in Figure 5.21 and Figure 5.22.

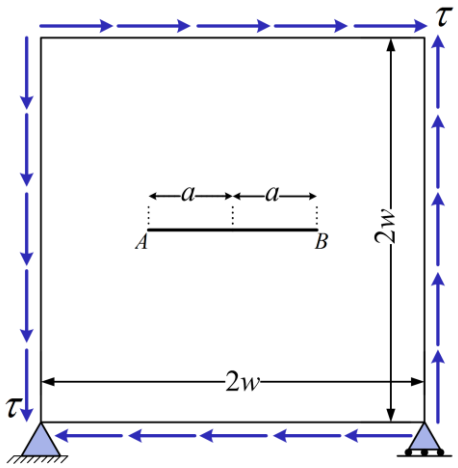

Figure 5.20. Infinite plate with a central crack under pure mode II

Table 5.1.Strain energy for the homogeneous infinite plate with a central crack under pure shear mode

	360	448	504	588	704	2206	5382
FEM-T3	976.2515	976.2797	976.2868	976.2955	976.3033	976.3235	976.3471
ES-FEM	976.4103	976.4339	976.4345	976.4363	976.4362	976.4364	976.4384
FEM-T6	976.5201	976.5517	976.5609	976.5620	976.5635	976.5649	976.5707
Sing ES-FEM	976.5364	976.5639	976.5650	976.5655	976.5660	976.5667	976.5735

Table 5.2. Normalized K_{II} at point A for the homogeneous infinite plate with a central crack under pure shear mode

	360 (Error %)	448 (Error %)	504 (Error %)	588 (Error %)	704 (Error %)	2206 (Error %)	5382 (Error %)
FEM-T3	0.9509 (4.9083)	0.9625 (3.7461)	0.9649 (3.5083)	0.9669 (3.3135)	0.9710 (2.9042)	0.9856 (1.4403)	0.9880 (1.2036)
ES-FEM	0.9847 (1.5301)	0.9879 (1.2098)	0.9894 (1.0580)	0.9922 (0.7765)	0.9933 (0.6701)	0.9937 (0.6313)	0.9937 (0.6287)
FEM-T6	0.9876 (1.2399)	0.9912 (0.8847)	0.9935 (0.6536)	0.9967 (0.3289)	0.9974 (0.2615)	0.9983 (0.1699)	0.9991 (0.0900)
Sing ES-FEM	0.9888 (1.1155)	0.9930 (0.6987)	0.9948 (0.5160)	0.9970 (0.2958)	0.9982 (0.1824)	0.9989 (0.1069)	0.9998 (0.0211)

Table 5.3. Normalized K_{II} at point B for the homogeneous infinite plate with a central crack under pure shear mode

	360 (Error %)	448 (Error %)	504 (Error %)	588 (Error %)	704 (Error %)	2206 (Error %)	5382 (Error %)
FEM-T3	0.9504 (4.9579)	0.9628 (3.7221)	0.9654 (3.4580)	0.9677 (3.2311)	0.9706 (2.9381)	0.9853 (1.4702)	0.9872 (1.2755)
ES-FEM	0.9847 (1.5292)	0.9880 (1.1961)	0.9893 (1.0716)	0.9918 (0.8213)	0.9928 (0.7172)	0.9932 (0.6824)	0.9934 (0.6598)
FEM-T6	0.9878 (1.2245)	0.9915 (0.8511)	0.9934 (0.6569)	0.9963 (0.3666)	0.9974 (0.2587)	0.9980 (0.2049)	0.9990 (0.1010)
Sing ES-FEM	0.9892 (1.0808)	0.9931 (0.6864)	0.9944 (0.5577)	0.9965 (0.3451)	0.9977 (0.2295)	0.9985 (0.1517)	0.9997 (0.0285)

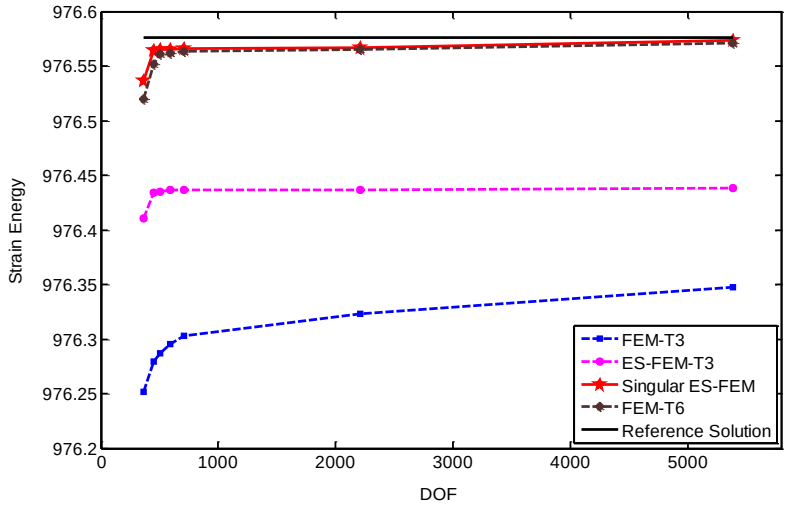

Figure 5.21. Strain energy for the infinite plate under mode *II*

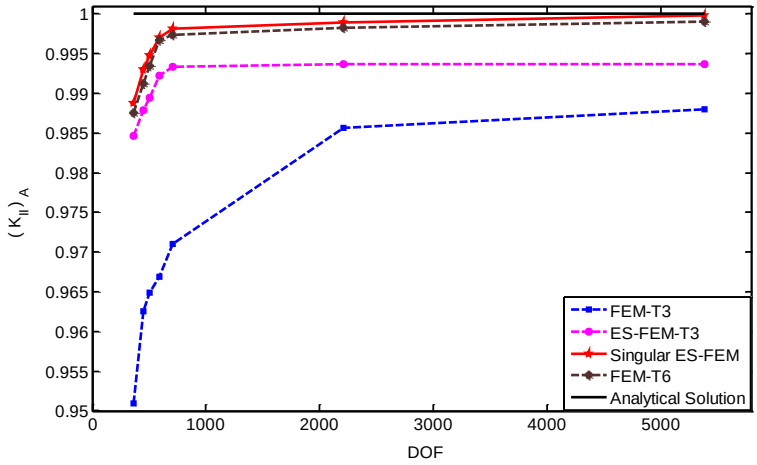

Figure 5.22. Normalized stress intensity factor at point *A*

Similar to the previous example and according to the results tabulated in the tables it can be seen that the value of stress intensity factor at points A and B is very close to each other. Therefore, the stress intensity factor behavior has been plotted only for one of the crack tip points. Based on the results it can be clearly observed that:

1) Singular ES-FEM with *SD*=1 works very well in this example to evaluate the strain energy and stress intensity factors at either of two crack tip points and provides the more accurate results than FEM-T6.

2) Based on Table 5.2 and Table 5.3 it can be clearly observed that by increasing the mesh the value of error declines to 0.02% for singular ES-FEM. It is much less in comparison with FEM and standard ES-FEM.

5.7.6 Double edge crack specimen

The geometry of double edge crack specimen is shown in Figure 5.23. The specimen is subjected to a remoter tensile stress σ at top edge and being fixed at the bottom. The

analytical formula of the stress intensity factor for such a specimen is given by Tada [96] as:

$$K_I = \sigma\sqrt{\pi a}[1.122 - 0.561(\frac{a}{w}) - 0.205(\frac{a}{w})^2 + 0.471(\frac{a}{w})^3 - 0.910(\frac{a}{w})^4] / (1-\frac{a}{w})^{0.5} \quad (5.37)$$

In this example, the parameters used are $w = 4.0\,cm$, $L = 11.0\,cm$, $a = 1.2\,cm$ and $\sigma = 1N/cm^2$. The material is isotropic elastic and material constants are $E = 3\times10^7$ and $\nu = 0.25$. In this example the effect of increasing the number of sub-smoothing domain is also examined. The results have been tabulated in Table 5.4, Table 5.5, and Table 5.6, and depicted in Figure 5.24 and Figure 5.25.

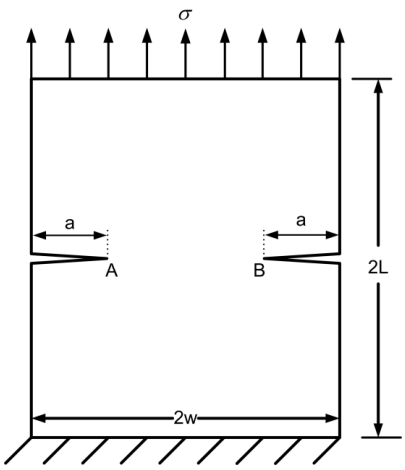

Figure 5.23. Double Edge Crack Specimen

Table 5.4. Strain energy for double edge crack specimen

	336	530	948	1286	1780
FEM-T3	2.8552e-004	2.8756e-004	2.8823e-004	2.8860e-004	2.8880e-004
ES-FEM	2.8862e-004	2.8952e-004	2.8960e-004	2.8975e-004	2.8979e-004
FEM-T6	2.8922e-004	2.9009e-004	2.9019e-004	2.9039e-004	2.9042e-004
Sing ES-FEM (S-SD=1)	2.8930e-004	2.9022e-004	2.9028e-004	2.9043e-004	2.9047e-004
Sing ES-FEM (S-SD=2)	2.8953e-004	2.9046e-004	2.9053e-004	2.9068e-004	2.9072e-004

Table 5.5. Normalized K_I at point *A* for double edge crack specimen

	336 (Error %)	530 (Error %)	948 (Error %)	1286 (Error %)	1780 (Error %)
FEM-T3	0.9249 (7.5073 %)	0.9582 (4.1825 %)	0.9691 (3.0897 %)	0.9722 (2.7782 %)	0.9752 (2.4750 %)
ES-FEM	0.9725 (2.7469 %)	0.9840 (1.5971 %)	0.9843 (1.5716 %)	0.9848 (1.5176 %)	0.9843 (1.5675 %)
FEM-T6	0.9763 (2.3704 %)	0.9896 (1.0399 %)	0.9918 (0.8244 %)	0.9935 (0.6531 %)	0.9990 (0.1001 %)
Sing ES-FEM (S-SD=1)	0.9772 (2.2839 %)	0.9890 (1.1035 %)	0.9924 (0.7596 %)	0.9941 (0.5863 %)	0.9985 (0.1498 %)
Sing ES-FEM- (S-SD=2)	0.9796 (2.0376 %)	0.9916 (0.8378 %)	0.9933 (0.6873 %)	0.9951 (0.4854 %)	0.9994 (0.0564 %)

Table 5.6. Normalized K_I at point *B* for double edge crack specimen

	336 (Error %)	530 (Error %)	948 (Error %)	1286 (Error %)	1780 (Error %)
FEM-T3	0.9333 (6.6730 %)	0.9580 (4.2013 %)	0.9715 (2.8513 %)	0.9730 (2.7045 %)	0.9752 (2.4825 %)
ES-FEM	0.9797 (2.0278 %)	0.9826 (1.7409 %)	0.9835 (1.6539 %)	0.9830 (1.6957 %)	0.9842 (1.5832 %)
FEM-T6	0.9766 (2.3399 %)	0.9882 (1.1846 %)	0.9915 (0.8523 %)	0.9929 (0.7140 %)	0.9989 (0.1111 %)
Sing ES-FEM (S-SD=1)	0.9844 (1.5616 %)	0.9875 (1.2487 %)	0.9923 (0.7601 %)	0.9931 (0.6845 %)	0.9982 (0.1764 %)
Sing ES-FEM- (S-SD=2)	0.9868 (1.3239 %)	0.9901 (0.9903 %)	0.9929 (0.7096 %)	0.9945 (0.5476 %)	0.0.9992 (0.0763 %)

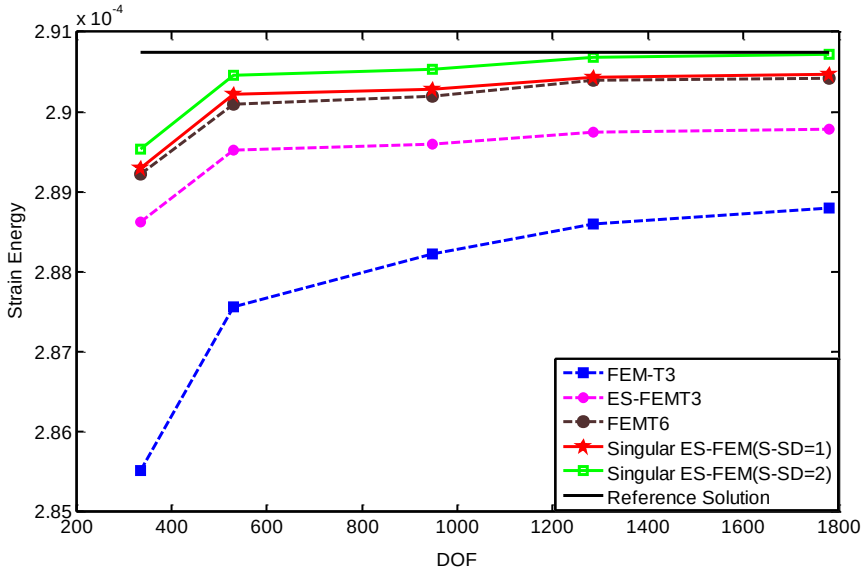

Figure 5.24. Strain energy results for the Double Edge Crack Specimen

Similar to the pervious example the stress intensity factor behavior has been plotted for one of the crack tips. Regarding to the results tabulated in the tables it can be seen that the value of stress intensity factor at points A and B is very close to each other.

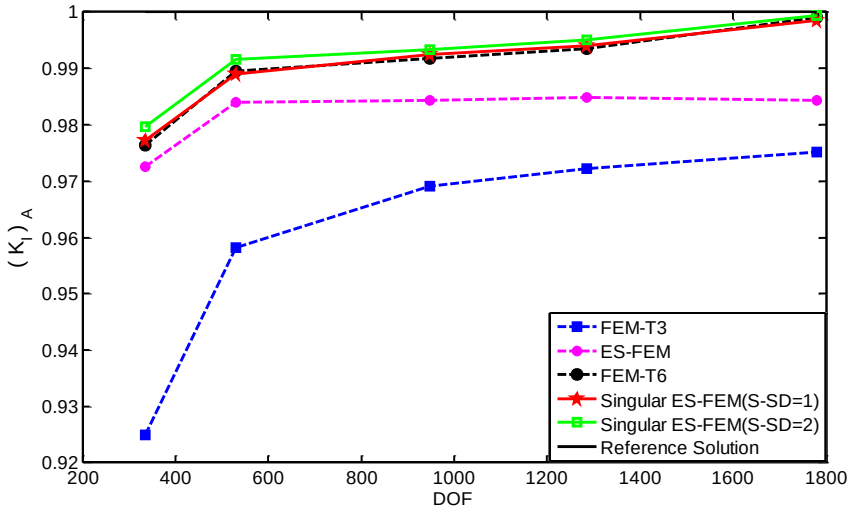

Figure 5.25. Normalized KI at point A for the Double Edge Crack Specimen

From these results it can be seen that:

1) The results of singular ES-FEM are more accurate than FEM-T3 and standard ES-FEM.

2) It also can be observed that using two sub-smoothing domains ($S\text{-}SD = 2$) can yield to the further improvement in the results including either strain energy and stress intensity factors.

Based on Table 5.5 and

3) Table 5.6, it is clear that for this example the value of numerical error for singular ES-FEM is much less than FEM-T3 and standard ES-FEM. This value decreases more by choosing two sub-smoothing domains (*S-SD=2*).

5.7.7 Single edge cracked plate under mixed-mode loading

A rectangular plate with an edge crack under shear load is examined as a plane strain problem with the geometry shown in Figure 5.26. The plate is clamped at the bottom and undergoes a shear load of $\tau = 1MPa$ at its top edge yielding a mixed-mode situation of fracture. The Young's modulus and Poisson's ratio of the plate are equal to $E = 3\times10^7\ N/mm^2$ and $\nu = 0.25$. In this example the dimensions of the plate are considered as $w = 7.0\ mm$, $h = 8.0\ mm$, $a = 3.5\,mm$. The reference solution for the stress intensity factor is available by [97]

$$\begin{aligned} K_I &= 34.0 \quad MPa\sqrt{mm} \\ K_{II} &= 4.55 \ MPa\sqrt{mm} \end{aligned} \tag{5.38}$$

The stress intensity factors in two Modes are calculated using FEM-T3, ES-FEM-T3, FEM-T6 and singular ES-FEM with S-SD=1. The integration domain is identified by a circular closed path around the crack tip as shown in Figure 5.27. As it is clear in this

figure, by changing the value of circle radius (r_d), the integration domain will change. For a common mesh and different integration domains, the results of FEM-T3, ES-FEM, FEM-T6 as well as singular ES-FEM with S-SD=1 have been tabulated in Table 5.7 and Table 5.8. Increasing the number of sub-smoothing domains will yield similar results.

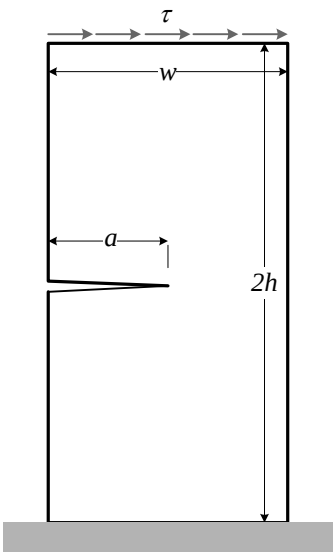

Figure 5.26. The single edge cracked plate under shear mode

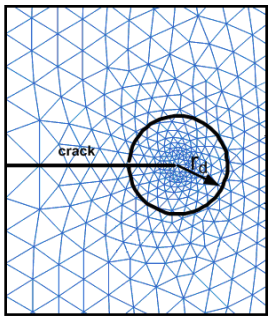

Figure 5.27. A closed up view around the crack tip and the circular path which defines the area for the J-integral and stress intensity factor calculations

Table 5.7. Normalized K_I value for different domain sizes.

Domain sizes r_d	FEM-T3	ES-FEM	FEM-T6	Singular ES-FEM (*S-SD=1*)
0.1 *	0.895895	0.889025	0.9883025	0.24523
0.3	0.961841	0.989298	0.991072	1.001909
0.5	0.958602	0.987162	0.991958	0.996139
0.7	0.956747	0.987214	0.991617	0.996182
0.9	0.956291	0.987206	0.991523	0.996174

* Integration domain is inside the crack tip elements

Table 5.8. Normalized K_{II} value for different domain sizes.

Domain sizes r_d	FEM-T3	ES-FEM	FEM-T6	Singular ES-FEM (S-SD=1)
0.1 *	0.862719	0.880563	0.903601	0.636927
0.3	0.971699	0.981927	0.983637	0.988385
0.5	0.975613	0.982901	0.984284	0.986631
0.7	0.974925	0.982558	0.984077	0.986292
0.9	0.975607	0.983338	0.984164	0.987064

* Integration domain is inside the crack tip elements

From these tables, it can be indicated that singular ES-FEM bring more accurate values of K_I and K_{II} than other methods when the integration domain is outside the crack tip elements. However, when it is inside the crack tip elements, the singular ES-FEM (SD=1) will lead to unstable solutions. It is also observed from these results that singular ES-FEM works very well with interaction integral and the results are nicely path independent.

5.7.8 Homogenous infinite plate with a central inclined crack under mixed mode

Based on the fact that path independency is the most important feature of *J*-integral theory, the stress intensity factors which are calculated in a similar fashion should also be path-independent. It means that using the different paths or domains around the crack tip

should not impose a considerable variation in the value of the stress intensity factors. In order to investigate this characteristic for the singular ES-FEM, an inclined crack under tension load is studied as an example of mixed mode situation. This structure is shown in Figure 5.28. In this example $w = 40\ mm$, $a = \sqrt{2}\ mm$, $\varphi = \frac{\pi}{4}$, and $\sigma = 1 MPa$. The analytical solution for such a structure is available as

$$\begin{cases} K_I = \sigma\sqrt{\pi a}\sin^2\varphi \\ K_{II} = \sigma\sqrt{\pi a}\sin\varphi\cos\varphi \end{cases} \tag{5.39}$$

For this example φ is fixed as $\varphi = \frac{\pi}{4}$ and therefore we will have

$$\frac{K_I}{\sigma\sqrt{\pi a}} = \frac{K_{II}}{\sigma\sqrt{\pi a}} = 0.5000 \tag{5.40}$$

The results of stress intensity factors for this structure has been evaluated using singular ES-FEM with one smoothing domain (*SD=1*) based on different paths around the crack tip and outside the crack tip elements. These results have been tabulated in Table 5.9 and Table 5.10. Similar to previous example; it can be clearly observed that singular ES-FEM presents stable results for different paths chosen around the crack tip.

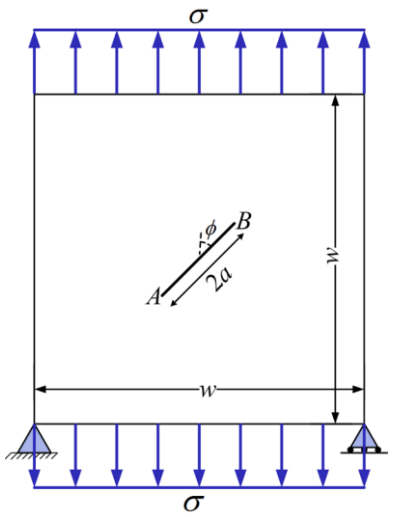

Figure 5.28.the plate with an inclined central crack under tension

Table 5.9. Path independency at point A for the specimen with inclined crack under tension load

	$r_d = 0.4$ (Error)	$r_d = 0.6$ (Error)	$r_d = 0.7$ (Error)	$r_d = 0.9$ (Error)	$r_d = 1$ (Error)
$\frac{K_I}{\sigma\sqrt{\pi a}}$	0.4991 (0.000867)	0.4997 (0.000269)	0.4996 (0.000359)	0.5001 (0.000127)	0.5002 (0.000203)
$\frac{K_{II}}{\sigma\sqrt{\pi a}}$	0.4962 (0.003799)	0.5017 (0.001685)	0.5018 (0.001804)	0.5060 (0.005965)	0.5010 (0.001050)

Table 5.10. Path independency at point B for the specimen with inclined crack under tension load

	$r_d = 0.4$ (Error)	$r_d = 0.6$ (Error)	$r_d = 0.7$ (Error)	$r_d = 0.9$ (Error)	$r_d = 1$ (Error)
$\frac{K_I}{\sigma\sqrt{\pi a}}$	0.4985 (0.001467)	0.4985 (0.001530)	0.4987 (0.001276)	0.4981 (0.001864)	0.4989 (0.001104)
$\frac{K_{II}}{\sigma\sqrt{\pi a}}$	0.4963 (0.003652)	0.5022 (0.002236)	0.5022 (0.002236)	0.5062 (0.006230)	0.5023 (0.002316)

5.8 Summary

In this chapter the novel method of singular ES-FEM was proposed and formulated to analyze linear elastic fracture mechanic problems including the general cases with more than one crack tip undergoing different fracture states of Mode I, Mode II or mixed-Mode configuration. The method uses a strain smoothing technique on a base mesh of linear triangular elements to create a softer model than that of FEM using the same mesh with the same set of nodes and elements. More importantly, the method proposes and establishes a new triangular element with a set of specially designed shape functions to capture the strain singularity at the vicinity of crack tip. Based on the way that smoothed strain gradient matrix is computed, additional smoothing domains and sub-smoothing domains were suggested associated with each edge of 5-node crack tip element, and a study were conducted to examine the effect of new discretization on the accuracy of results. Using the developed method several examples were solved and the results were presented in terms of strain energy, displacement, stress intensity factor, and computational efficiency and convergence rate.

Based on the findings, it can be highlighted that singular ES-FEM with one sub-smoothing domain adopted for each crack tip smoothing domain always provides the more accurate results than standard ES-FEM and FEM using linear triangular elements. However, it is not always superior to singular FEM (with quarter-point elements). To enhance the performance of the proposed approach in comparison with singular FEM, the number of smoothing domains and sub-smoothing domains were increased. Several analyses then revealed that while increasing the number of sub-smoothing domains in the

setting of singular ES-FEM does not improve the results, increasing the number of sub-smoothing domains always leads to the more accurate results than those of singular FEM with quarter-point elements. Therefore, to be on the safe side, one can always use singular ES-FEM with two sub-smoothing domains at each smoothing domain associated with each of the newly- proposed 5-node crack tip element.

Chapter 6: Singular ES-FEM for interfacial crack analysis

"An obstacle is often a stepping stone"

Prescott

6.1 Introduction

In the previous chapter the new approach of singular ES-FEM for isotropic materials was introduced and its performance was thoroughly examined through several examples. In this chapter the method is further developed to make it capable of properly examining the interfacial crack between two dissimilar isotropic materials.

6.2 Interface fracture mechanics

A schematic of two dimensional structures with a bimaterial interface crack along the interface of two semi-infinite planes is shown in Figure 6.1. In this figure, the upper plane is denoted by material 1 with Young's modulus and Poisson's ratio of E_1 and v_1, respectively, and the lower plane is assumed as material 2 with corresponding properties of E_2 and v_2.

The stress intensity factor for an interfacial crack is represented as a complex value

of $\mathbf{K} = K_I + iK_{II}$ [98, 99], where the in-plane traction vector at a distance r ahead of the crack is expressed as:

$$(\sigma_{22} + i\tau_{12})_{\theta=0} = \frac{\mathbf{K} r^{i\varepsilon}}{\sqrt{2\pi r}} \tag{6.1}$$

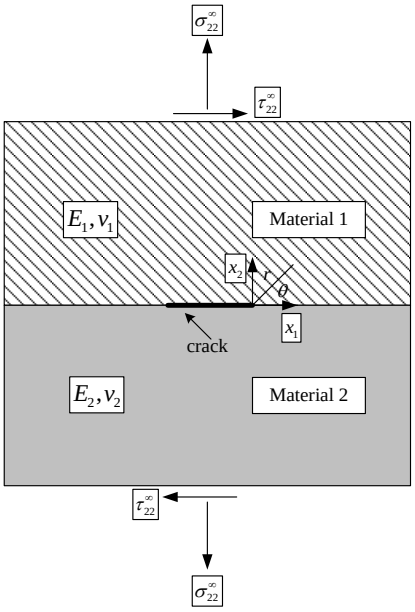

Figure 6.1. Bimaterial interface crack

Where i is assigned as the square root of -1, and ε as a bimaterial constant with the following form

$$\varepsilon = \frac{1}{2\pi} \log\left(\frac{1-\beta}{1+\beta}\right) \tag{6.2}$$

In which β is called "second Dundurs parameter" [100] and in terms of material properties is described as

$$\beta = \frac{\mu_1(k_2 - 1) - \mu_2(k_1 - 1)}{\mu_1(k_2 + 1) + \mu_2(k_1 + 1)} \tag{6.3}$$

Where k_i $(i=1,2)$ is the so-called "Kolosov constant of material" and is calculated in terms of shear modulus (μ_i) and Poisson's ratio (ν_i) of the material

$$k_i = \begin{cases} \dfrac{3-\nu_i}{1+\nu_i} & \textit{(plane stress)} \\ 3-4\nu_i & \textit{(plane strain)} \end{cases} \qquad (i = 1,2) \tag{6.4}$$

Similar to the cracks in isotropic materials, stress intensity factors and *J*-integral parameter for interfacial cracks are also relevant to each other. The relation between these parameters is expressed as the following equation [99],

$$J = G = \frac{1}{E^*}\frac{|\mathbf{K}|^2}{\cosh^2(\pi\varepsilon)}, \qquad |\mathbf{K}|^2 = \mathbf{K}\bar{\mathbf{K}} = K_I^2 + K_{II}^2 \tag{6.5}$$

Where

$$\frac{2}{E^*} = \frac{1}{\bar{E}_1} + \frac{1}{\bar{E}_2}, \qquad \bar{E}_i = \begin{cases} E_i & \textit{(plane stress)} \\ \dfrac{E_i}{1-\nu_i^2} & \textit{(plane strain)} \end{cases} \tag{6.6}$$

The parameter ψ is called "phase angle" and plays an important role in characterization of interfacial crack behavior. For a given loading configuration, it provides a measure of relative proportion of shear to normal tractions at a distance l ahead of the crack tip, in which l is addressed as the characteristic length and is happened to be the smallest specimen dimension. It should be noted that interfacial crack problems are different from isotropic ones in the point that tension and shear effects are inseparable in the vicinity of crack. The phase angle ψ for such an interfacial crack problem can be evaluated then through the following relation [98],

$$\mathbf{K}l^{i\varepsilon} = |\mathbf{K}|e^{i\psi} \tag{6.7}$$

Or

$$\psi = \tan^{-1}\left(\frac{\mathrm{Im}[\mathbf{K}l^{i\varepsilon}]}{\mathrm{Re}[\mathbf{K}l^{i\varepsilon}]}\right) \tag{6.8}$$

In which Re[·] and Im[·] denote the real and imaginary parts of a complex number, respectively.

Formula (6.9) to (6.13) express the Cartesian components of near-crack tip displacement fields (for the upper-half plane) in terms of materials constants, stress intensity factors, and polar coordinates components (r,θ) with the origin at the crack tip [98]. For the lower-half plane the equations are slightly varied due to replacing term $\varepsilon\pi$ by $-\varepsilon\pi$ [99]:

$$u_j = \frac{1}{2u_1}\sqrt{\frac{r}{2\pi}}\left\{\mathrm{Re}[\mathbf{K}l^{i\varepsilon}]\tilde{u}_j^{I}(\theta,\varepsilon,v_1) + \mathrm{Im}[\mathbf{K}l^{i\varepsilon}]\tilde{u}_j^{II}(\theta,\varepsilon,v_1)\right\} \quad (j=1,2) \tag{6.9}$$

$$\tilde{u}_1^{I} = A\left[-e^{2\varepsilon(\pi-\theta)}\left(\cos\frac{\theta}{2}+2\varepsilon\sin\frac{\theta}{2}\right)+k_I\left(\cos\frac{\theta}{2}-2\varepsilon\sin\frac{\theta}{2}\right)+(1+4\varepsilon^2)\sin\frac{\theta}{2}\sin\theta\right] \tag{6.10}$$

$$\tilde{u}_1^{II} = A\left[e^{2\varepsilon(\pi-\theta)}\left(\sin\frac{\theta}{2}-2\varepsilon\cos\frac{\theta}{2}\right)+k_I\left(\sin\frac{\theta}{2}+2\varepsilon\cos\frac{\theta}{2}\right)+(1+4\varepsilon^2)\cos\frac{\theta}{2}\sin\theta\right] \tag{6.11}$$

$$\tilde{u}_2^{I} = A\left[e^{2\varepsilon(\pi-\theta)}\left(\sin\frac{\theta}{2}-2\varepsilon\cos\frac{\theta}{2}\right)+k_I\left(\sin\frac{\theta}{2}+2\varepsilon\cos\frac{\theta}{2}\right)-(1+4\varepsilon^2)\cos\frac{\theta}{2}\sin\theta\right] \tag{6.12}$$

$$\tilde{u}_2^{II} = A\left[e^{2\varepsilon(\pi-\theta)}\left(\cos\frac{\theta}{2}+2\varepsilon\sin\frac{\theta}{2}\right)-k_I\left(\cos\frac{\theta}{2}-2\varepsilon\sin\frac{\theta}{2}\right)+(1+4\varepsilon^2)\sin\frac{\theta}{2}\sin\theta\right] \tag{6.13}$$

In which

$$A = \frac{e^{-\varepsilon(\pi-\theta)}}{(1+4\varepsilon^2)\cosh(\pi\varepsilon)} \tag{6.14}$$

Note that, in the foregoing equations, one can write $r^{i\varepsilon} = \mathrm{e}^{i\varepsilon \log r} = \cos(\varepsilon \log r) + i \sin(\varepsilon \log r)$.

6.3 ES-FEM for bimaterial interface

6.3.1 Governing equations

Consider a 2D static elastic problem governed by the equilibrium equation in the domain $\Omega = \Omega^+ + \Omega^-$ separated by a single interface, Γ_i as shown in Figure 6.2:

$$\nabla \cdot \boldsymbol{\sigma} + \mathbf{b} = 0 \quad in\ \Omega \tag{6.15}$$

where ∇ is the divergence operator, $\boldsymbol{\sigma}$ is the Cauchy stress tensor and $\mathbf{b}$ is the body force term.

The essential and natural boundary conditions are given by:

$$\mathbf{u} = \mathbf{u}_\Gamma \quad on\ \Gamma_u \tag{6.16}$$

$$\boldsymbol{\sigma} \cdot \mathbf{n} = \mathbf{t}_\Gamma \quad on\ \Gamma_t \tag{6.17}$$

where $\mathbf{u}_\Gamma$ and $\mathbf{t}_\Gamma$ are the vectors of the prescribed displacements and tractions respectively, and $\mathbf{n}$ is the outward normal unit vector defined on the boundary Γ.

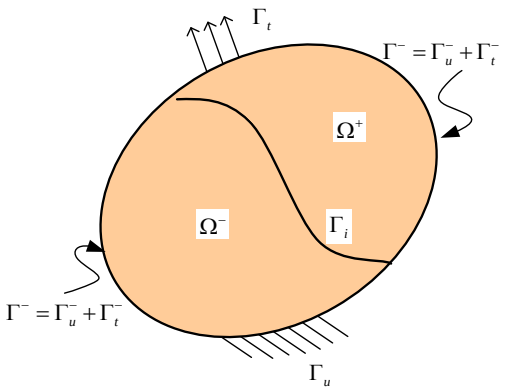

Figure 6.2. Inhomogeneous body with interface subjected loads

On the interface Γ_i, continuity of tractions and displacements requires

$$\langle t_i \rangle = t_i^+ - t_i^- = 0 \tag{6.18}$$

$$\langle u_i \rangle = u_i^+ - u_i^- = 0 \tag{6.19}$$

where $\langle . \rangle$ denotes a jump.

The constitution equation (stress-strain relation) is given by:

$$\boldsymbol{\sigma} = \mathbf{D}\boldsymbol{\varepsilon} \tag{6.20}$$

where $\mathbf{D}$ is the matrix of material constants, and $\boldsymbol{\sigma}^{\mathrm{T}} = \{\sigma_{xx} \quad \sigma_{yy} \quad \tau_{xy}\}$ and $\boldsymbol{\varepsilon}^{\mathrm{T}} = \{\varepsilon_{xx} \quad \varepsilon_{yy} \quad \gamma_{xy}\}$ are the vector forms of the stress and strain tensor respectively. The strain-displacement relation is given by:

$$\boldsymbol{\varepsilon} = \nabla_s \mathbf{u} \tag{6.21}$$

where $\mathbf{u} = \{u_x \quad u_y\}^{\mathrm{T}}$ is the vector of the displacement and $\nabla_s \mathbf{u}$ is the symmetric gradient of the displacement field.

6.4 Edge-based strain smoothing

In the ES-FEM, however, we do not use the compatible strains $\boldsymbol{\varepsilon} = \nabla_s \mathbf{u}$ but the strains "smoothed" over the local smoothing domains. These local smoothing domains are constructed with respect to the edges of triangular elements such that $\Omega = \bigcup_{k=1}^{N_s} \Omega^{(k)}$ and $\Omega^{(i)} \cap \Omega^{(j)} = \varnothing$, $i \neq j$, in which N_s is the number of smoothing domains. The rule is that the problem domain is first divided into two sub-domains based on the assignment of materials as shown in Figure 6.3.

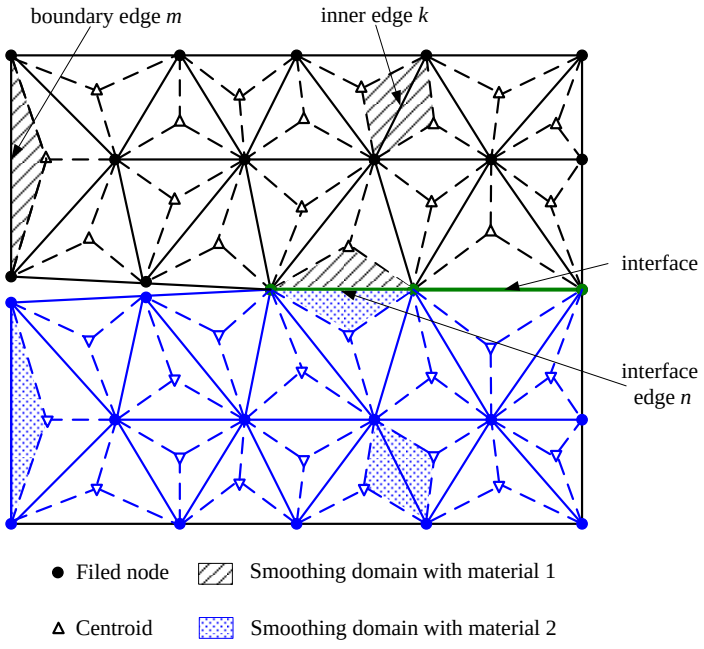

Figure 6.3. Construction of edge-based strain smoothing domains

Then, for each sub-domain with the isotropic material, the smoothing domain corresponding to the inner edge *k*, $\Omega^{(k)}$, is formed by connecting two end points of edge *k* and two centroids of the adjacent triangular elements. The smoothing domain for the

boundary edge *m* or the interface edge *n*, $\Omega^{(m)}$ or $\Omega^{(n)}$, is just one third region of triangular element which contains the edge *m* or the edge *n*.

6.5 Domain Interaction Integral Methods for Bimaterial Interface Cracks

In the linear elasticity, the general form of *J*-contour integral which is identical to the energy release rate, for a two dimensional crack can be written as [101]:

$$J = G = \int_{\Gamma} (\frac{1}{2}\sigma_{ik}\varepsilon_{ik}\delta_{1j} - \sigma_{ij}u_{i,1})n_j d\Gamma \tag{6.22}$$

The *J*-integral remains globally path independent for bimaterial interface crack problems when there exists no material inhomogeneity in the direction parallel to the crack [101]. In this case, the mixed-mode stress intensity factors K_I and K_{II} are evaluated using the domain form of contour interaction integral by considering two states of a cracked body including state 1, $(\sigma_{ij}^{(1)}, \varepsilon_{ij}^{(1)}, u_i^{(1)})$, corresponds to the present state and state 2, $(\sigma_{ij}^{(2)}, \varepsilon_{ij}^{(2)}, u_i^{(2)})$, associated with the auxiliary state. Here, unlike the cracks in homogeneous materials, it is chosen as the asymptotic fields with the oscillatory effect $r^{i\varepsilon}$ at interface crack tip. On summing the *J*-integral of two states, we can obtain the contour interaction integral [6]:

$$I = \int_{\Gamma} (\sigma_{ik}^{(1)}\varepsilon_{ik}^{(2)}\delta_{1j} - \sigma_{ij}^{(1)}u_{i,1}^{(2)} - \sigma_{ij}^{(2)}u_{i,1}^{(1)})n_j d\Gamma \qquad ;(i, j = 1, 2) \tag{6.23}$$

From equation (6.5) , the interaction integral is related to the SIFs through the relation

$$I = \frac{2}{E^*}\frac{K_I^{(1)}K_I^{(2)} + K_{II}^{(1)}K_{II}^{(2)}}{\cosh^2(\pi\varepsilon)} \tag{6.24}$$

Making the judicious choice of state 2 (auxiliary) as the pure Mode I asymptotic

fields, i.e., setting $K_I^{(2)}=1,\ K_I^{(2)}=0$ and evaluating $I=I_1$, we can compute K_I and we proceed in an analogous manner to evaluate K_{II} :

$$K_I=\frac{E^*\cosh^2(\pi\varepsilon)}{2}I_I \qquad K_{II}=\frac{E^*\cosh^2(\pi\varepsilon)}{2}I_{II} \tag{6.25}$$

To extract the mixed-mode stress intensity factors K_I and K_{II} for bimaterial interface cracks, the auxiliary displacement field in the local x_1-x_2 crack-tip co-ordinate system (Figure 6.1) is more complex compared to the cracks in homogeneous materials, and can be written as:

$$u_j=\begin{cases}\dfrac{1}{4u_1\cosh(\pi\varepsilon)}\sqrt{\dfrac{r}{2\pi}}\,f_j(r,\theta,\varepsilon,k_1) & ;\textit{(upper-half plane)}\\ \dfrac{1}{4u_2\cosh(\pi\varepsilon)}\sqrt{\dfrac{r}{2\pi}}\,f_j(r,\theta,\varepsilon,k_2) & ;\textit{(lower-half plane)}\end{cases} \quad (j=1,2) \tag{6.26}$$

where ε is the bimaterial constant that is defined in equation (6.2). To extract K_I, the functions f_1 and f_2 are

$$f_1=D+T_1 \qquad f_2=-C-T_2 \tag{6.27}$$

whereas to compute K_{II}, the expressions for f_1 and f_2 are:

$$f_1=-C+T_2 \qquad f_2=-D+T_1 \tag{6.28}$$

In the above equations δ, φ, C, D, T_1 and T_2 are defined as:

$$C=\beta'\gamma\cos\frac{\theta}{2}-\beta\gamma'\sin\frac{\theta}{2} \qquad D=\beta\gamma\cos\frac{\theta}{2}+\beta'\gamma'\sin\frac{\theta}{2} \tag{6.29}$$

$$T_1=2\delta\sin\theta\sin\varphi \qquad T_2=2\delta\sin\theta\cos\varphi \tag{6.30}$$

$$\delta = \begin{cases} e^{-(\pi-\theta)\varepsilon} & (upper\text{-}half\ \ plane) \\ e^{(\pi+\theta)\varepsilon} & (lower\text{-}half\ \ plane) \end{cases} \qquad ;\varphi = \varepsilon \log r + \frac{\theta}{2} \tag{6.31}$$

$$\beta = \frac{0.5\cos(\varepsilon \log r) + \varepsilon \sin(\varepsilon \log r)}{0.25 + \varepsilon^2} \qquad \beta' = \frac{0.5\sin(\varepsilon \log r) - \varepsilon \cos(\varepsilon \log r)}{0.25 + \varepsilon^2} \tag{6.32}$$

$$\gamma = k\delta - \frac{1}{\delta} \qquad \gamma' = k\delta + \frac{1}{\delta} \tag{6.33}$$

in which

$$k = \begin{cases} k_1 & (upper\text{-}half\ \ plane) \\ k_2 & (lower\text{-}half\ \ plane) \end{cases} \tag{6.34}$$

The auxiliary strain components are the symmetric gradient of the auxiliary displacement components:

$$\varepsilon_{ij}^{(2)} = \frac{1}{2}(u_{i,j}^{(2)} + u_{j,i}^{(2)}) \tag{6.35}$$

On defining

$$E = \beta'\gamma' \cos\frac{\theta}{2} - \beta\gamma \sin\frac{\theta}{2} \qquad F = \beta\gamma' \cos\frac{\theta}{2} + \beta'\gamma \sin\frac{\theta}{2} \tag{6.36}$$

we have

$$C_{,r} = \frac{\varepsilon D}{r} \qquad C_{,\theta} = -\frac{F}{2} + \varepsilon E \tag{6.37}$$

$$D_{,r} = -\frac{\varepsilon C}{r}, \qquad D_{,\theta} = \frac{E}{2} + \varepsilon F \tag{6.38}$$

On setting

$$T_3 = 2\delta \cos\theta \sin\varphi, \qquad T_4 = 2\delta \cos\theta \cos\varphi \tag{6.39}$$

we have

$$T_{1,\,r} = \frac{\varepsilon T_2}{r}, \qquad T_{1,\,\theta} = \varepsilon T_1 + \frac{T_2}{2} + T_3 \tag{6.40}$$

$$T_{2,\,r} = \frac{\varepsilon T_1}{r}, \qquad T_{2,\,\theta} = \varepsilon T_2 - \frac{T_1}{2} + T_4 \tag{6.41}$$

If K_I is to be extracted, then

$$f_{1,\,\alpha} = D_{,\,\alpha} + T_{1,\,\alpha}, \qquad f_{2,\,\alpha} = -C_{,\,\alpha} - T_{2,\,\alpha} \qquad (\alpha = r, \theta) \tag{6.42}$$

whereas if K_{II} is to be computed, then

$$f_{1,\,\alpha} = -C_{,\,\alpha} + T_{2,\,\alpha}, \qquad f_{2,\,\alpha} = -D_{,\,\alpha} - T_{1,\,\alpha} \qquad (\alpha = r, \theta) \tag{6.43}$$

Since $r_{,\,1} = \cos\theta$, $r_{,\,2} = \sin\theta$, $\theta_{,\,1} = -\sin\theta / r$ and $\theta_{,\,2} = \cos\theta / r$, on using the chain rule, we can write the derivatives of f_1 and f_2 in the $x_1 - x_2$ co-ordinate system as:

$$f_{1,\,1} = f_{1,\,r} r_{,\,1} + f_{1,\,\theta}\theta_{,\,1}, \qquad f_{1,\,2} = f_{1,\,r} r_{,\,2} + f_{1,\,\theta}\theta_{,\,2} \tag{6.44}$$

$$f_{2,\,1} = f_{2,\,r} r_{,\,1} + f_{2,\,\theta}\theta_{,\,1}, \qquad f_{2,\,2} = f_{2,\,r} r_{,\,2} + f_{2,\,\theta}\theta_{,\,2} \tag{6.45}$$

Letting

$$A = \begin{cases} \dfrac{1}{4u_1 \cosh(\pi\varepsilon)} & \textit{(upper-half plane)} \\ \dfrac{1}{4u_2 \cosh(\pi\varepsilon)} & \textit{(lower-half plane)} \end{cases} \qquad B = \sqrt{\frac{r}{2\pi}} \tag{6.46}$$

we can now write the gradients of the auxiliary displacements as:

$$u^{(2)}_{1,\,1} = A(Bf_{1,\,1} + \frac{r_{,\,1} f_1}{4\pi B}), \qquad u^{(2)}_{1,\,2} = A(Bf_{1,\,2} + \frac{r_{,\,2} f_1}{4\pi B}) \tag{6.47}$$

$$u^{(2)}_{2,\,1} = A(Bf_{2,\,1} + \frac{r_{,\,1} f_2}{4\pi B}), \qquad u^{(2)}_{2,\,2} = A(Bf_{2,\,2} + \frac{r_{,\,2} f_2}{4\pi B}) \tag{6.48}$$

Finding the differentiations of displacement components, one can easily calculate the auxiliary strain components using equation (6.35). The auxiliary stress is then easily evaluated by substituting the obtained strains in the Hooke's law.

6.6 Numerical examples

6.6.1 Centre-crack in an Infinite bimaterial plate

The problem of an interface crack between two dissimilar elastic semi-infinite planes under remote traction $\mathbf{t} = \sigma_{22}^{\infty} + i\tau_{12}^{\infty}$ as depicted in Figure 6.1 is first studied. The exact solution to this problem was provided by Rice and Sih [98, 102] as:

$$\mathbf{K} = K_I + iK_{II} = (\sigma_{22}^{\infty} + i\tau_{12}^{\infty})(1+2i\varepsilon)\sqrt{\pi a}(2a)^{-i\varepsilon} \tag{6.49}$$

The case of pure tension remote loading is first studied in details. In the computation, only half of the specimen is considered with the appropriate displacement constraint due to symmetry (Figure 6.4). The right edge are constrained in *x* direction to remove the edge singularity [98].

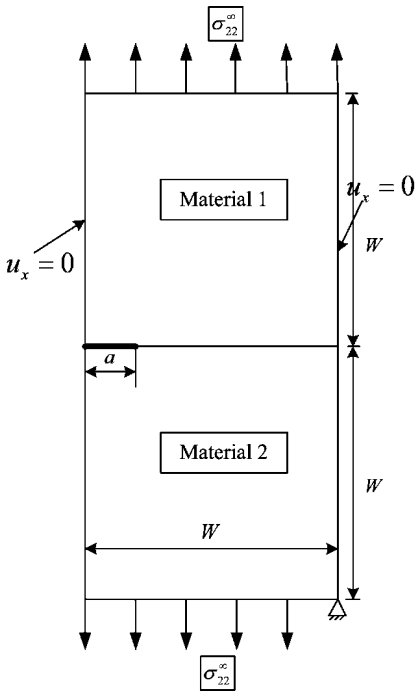

Figure 6.4. Centre-crack under remote tension (half model)

The factors K_0 and G_0 are used to normalize the stress intensity factors and the energy release rate, respectively, as

$$K_0 = \sigma_{22}^{\infty}\sqrt{\pi a} \qquad G_0 = \frac{(\sigma_{22}^{\infty})^2 a}{E_1} \tag{6.50}$$

where $2a$ is the crack length. The material constants used in the numerical computation are: $E_2 / E_1 = 22$, $\nu_1 = 0.3$ and $\nu_2 = 0.2571$, and plane strain conditions are assumed. The exact solutions from equation (6.49) are:

$$\frac{K_I}{K_0} = 1.008 \qquad \frac{K_{II}}{K_0} = 0.1097 \quad \frac{G}{G_0} = 1.4358 \tag{6.51}$$

An in-depth numerical investigation is conducted, with the following objectives:

1) To investigate the influence of the number of gauss points along one segment of

smoothing domains on the SIFs , energy release rate G and strain energy;

2) To compare the SIFs, G and convergence rate of the relative error in energy norm using the standard FEM, ES-FEM and the singular ES-FEM with the same triangular meshes.

3) To study domain independence,

4) To study robustness of the method: accuracy of the SIFs and G under small perturbations of the crack-tip, and finally,

5) To compute SIFs and G for a wide range of material mismatch combinations.

The crack dimension is selected as $a=1$. Since the exact solution is for the infinite domain problem, the sample size $W/a=30$ is used in all models to avoid the effect of finite size. Five structured meshes with a/h: (3.0, 4.0, 6.0, 8.0 and 10.0) and one unstructured mesh from ABAQUS are adopted, where h is the mesh spacing. A sample structured mesh ($a/h=8.0$) and unstructured mesh in the vicinity of crack tip are, respectively, shown in Figure 6.5 and Figure 6.6. All the studies are conducted using the domain radius parameter $r_k=4$, unless stated to be otherwise. The strain energy and the error in energy norm are respectively defined as:

$$\|\mathbf{u}\|_{E(\Omega)}=(\frac{1}{2}\int_{\Omega}\boldsymbol{\varepsilon}^T\mathbf{D}\boldsymbol{\varepsilon}\mathrm{d}\Omega)^{1/2} \tag{6.52}$$

$$e_e=\left\|\mathbf{u}-\mathbf{u}^h\right\|_{E(\Omega)}=(\frac{1}{2}\int_{\Omega}(\boldsymbol{\varepsilon}-\boldsymbol{\varepsilon}^h)^T\mathbf{D}(\boldsymbol{\varepsilon}-\boldsymbol{\varepsilon}^h)\mathrm{d}\Omega)^{1/2} \tag{6.53}$$

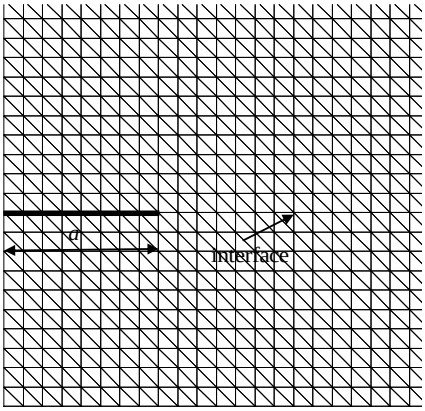

Figure 6.5. Structured meshe in the vicinity of the crack ($a/h=8.0$).

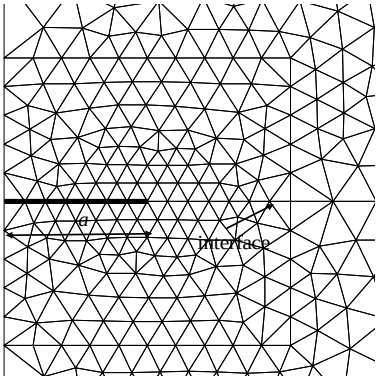

Figure 6.6. Unstructured mesh in the vicinity of the crack ($a=1, W=20$).

Table 6.1 lists the results of the study of number of Gauss points' effects. In this study, the mesh with $a/h=8.0$ is used. It can be seen that strain energy and SIFs keep nearly constant when more than 5 gauss points are used. Thus, all the models discussed later use 5 gauss points along one segment of the smoothing domain. Note that the less the gauss points used, the higher the strain energy and the SIFs. This may be explained that less gauss points bring the effect of the similar reduce integration, and thus lead to over-estimation of results.

In Table 6.2, comparison of the SIFs and the energy release rate using different numerical methods (standard FEM, ES-FEM, singular FEM and singular ES-FEM) are presented.

Table 6.1. Centre-crack under remote tension: the number of Gauss points effects

N_{GP}	$\|\mathbf{u}\|_{E(\Omega)}$	K_I / K_0 (% error)	K_{II} / K_0 (% error)	G / G_0 (% error)
1	0.01049016	1.0063 (0.1)	0.1100 (0.2)	1.4306 (0.3)
3	0.01048783	1.0060 (0.2)	0.1099 (0.1)	1.4297 (0.4)
5	0.01048779	1.0060 (0.2)	0.1098 (0.1)	1.4297 (0.4)
7	0.01048778	1.0060 (0.2)	0.1098 (0.1)	1.4297 (0.4)

Table 6.2. Centre-crack under remote tension: comparison of stress intensity factors and energy release rate using standard FEM, singular FEM, ES-FEM and singular ES-FEM.

Exact solution	a/h / Method	3.0 (% error)	4.0(% error)	6.0(% error)	8.0(% error)	10.0(% error)
$K_1 / K_0 = 1.008$	FEM-T3	0.9740 (3.4)	0.9834 (2.4)	0.9903 (1.8)	0.9939 (1.4)	0.9959 (1.2)
	ES-FEM	0.9944 (1.3)	0.9989 (0.9)	1.0020 (0.6)	1.0033 (0.5)	1.0041 (0.4)
	FEM-T6	1.0030 (0.5)	1.0046 (0.4)	1.0057 (0.3)	1.0059 (0.2)	1.0062 (0.2)
	Sing ES-FEM	1.0039 (0.4)	1.0051 (0.3)	1.0060 (0.2)	1.0061 (0.2)	1.0063 (0.2)
$K_{II} / K_0 = 0.1097$	FEM-T3	0.1244 (13.4)	0.1192 (8.6)	0.1141(4.6)	0.1122 (2.3)	0.1111 (1.3)
	ES-FEM	0.1165 (6.2)	0.1134 (3.4)	0.1118 (1.0)	0.1108 (1.0)	0.1104 (0.6)
	FEM-T6	0.1119 (2.0)	0.1106 (0.9)	0.1105 (0.9)	0.1101 (0.3)	0.1099 (0.2)
	Sing ES-FEM	0.1119 (2.0)	0.1106 (0.9)	0.1105 (0.9)	0.1101 (0.3)	0.1099 (0.2)
	FEM-T3	1.3459 (6.3)	1.3699 (4.6)	1.3872 (3.4)	1.3964 (2.7)	1.4018 (2.4)
	ES-FEM	1.3993 (2.5)	1.4109 (1.7)	1.4188 (1.2)	1.4223 (0.9)	1.4244 (0.8)
	FEM-T6	1.4219 (1.0)	1.4261 (0.7)	1.4292 (0.5)	1.4296 (0.4)	1.4304 (0.4)
	Sing ES-FEM	1.4244 (0.8)	1.4273 (0.6)	1.4296 (0.4)	1.4301 (0.4)	1.4306 (0.3)

It can be highlighted from these results that compared to standard FEM, ES-FEM and even FEM with the singular elements, the SIFs and G of the singular ES-FEM, no matter what mesh size is used, are much closer to the exact values. More importantly, the relative errors of K_I, K_{II} and G using the singular ES-FEM are all within 1 percent for

all the models used in this study, except the case of K_{II} value with the very coarse mesh ($a/h=3.0$). In addition, Figure 6.7 compares the strain energy for different numerical methods. The reference solution has been obtained using the singular FEM with 50×10^4 degrees of freedom (DOF) that is 20 times the greatest DOF adopted in the numerical analysis. Clearly, the convergence of both strain energy and error in energy norm for the singular ES-FEM models is faster than that of the standard FEM, ES-FEM or FEM-T6 with the singular elements. All of these indicate the singular ES-FEM can solve the interface crack problems effectively.

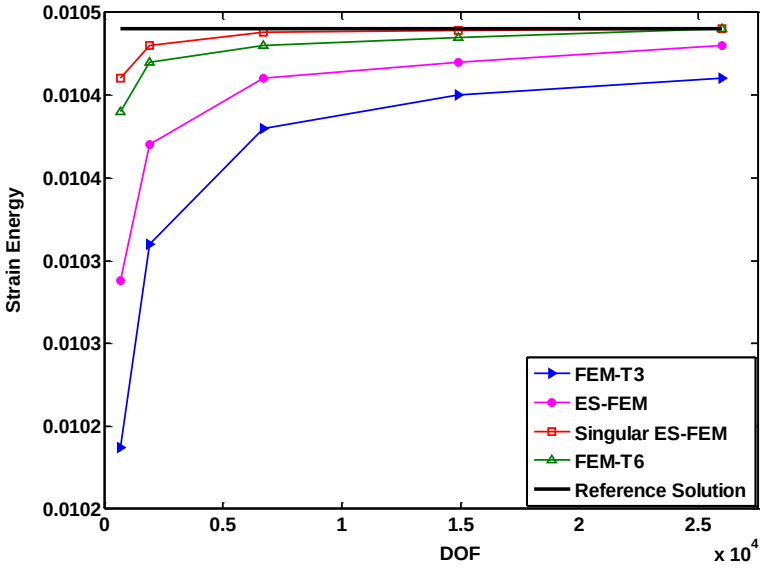

Figure 6.7. Strain energy for the problem of Centre-crack under remote tension.

Table 6.3 provides the results of domain independence study using both the structured mesh and unstructured mesh. We can easily observe domain independence of the SIFs for $r_k > 3$ on both structured and unstructured meshes.

To study the robustness of the singular ES-FEM, a simple test is conducted. The

crack-tip location is perturbed by $\Delta/a = \pm 0.001$ and the results are compared to those when $\Delta = 0$. The mesh parameter is $a/h = 8.0$. The results are shown in Table 6.4. From the results, we can notice clearly that the SIFs and G from all the numerical calculations are in excellent agreement with the corresponding exact solutions.

Table 6.3. Centre-crack under remote tension: domain independence study

Mesh	r_k	K_I / K_0 (% error)	K_{II} / K_0 (% error)	G / G_0 (% error)
Structured $a/h_e = 4.0$	2	1.0123 (0.4)	0.1078 (1.7)	1.4467 (0.8)
	3	1.0052 (0.3)	0.1109 (1.1)	1.4276 (0.6)
	4	1.0048 (0.3)	0.1103 (0.6)	1.4262 (0.7)
Structured $a/h_e = 8.0$	2	1.0129 (0.5)	0.1065 (2.9)	1.4480 (0.9)
	3	1.0059 (0.2)	0.1094 (0.3)	1.4291 (0.5)
	4	1.0060 (0.2)	0.1098 (0.1)	1.4297 (0.4)
	5	1.0061 (0.2)	0.1100 (0.3)	1.4293 (0.4)
	6	1.0061 (0.2)	0.1100 (0.3)	1.4295 (0.4)
Unstructured	2	1.0036 (0.4)	0.1095 (0.2)	1.4229 (0.9)
	3	1.0058 (0.2)	0.1099 (0.2)	1.4289 (0.5)
	4	1.0060 (0.2)	0.1099 (0.2)	1.4293 (0.4)
	5	1.0059 (0.2)	0.1098 (0.1)	1.4292 (0.4)

Table 6.4. Centre-crack under remote tension: robust study.

Crack-tip perturbation Δ / a	K_I / K_0 (% error)	K_{II} / K_0 (% error)	G / G_0 (% error)
0	1.0060 (0.2)	0.1098 (0.1)	1.4297 (0.4)
-0.001	1.0055 (0.3)	0.1098 (0.1)	1.4281 (0.5)
0.001	1.0066 (0.1)	0.1099 (0.2)	1.4314 (0.3)

To study the performance of the singular ES-FEM on interface crack for different material property pairs, the ratio E_1 / E_2 is varied from 2 to 1000 with the constant poison ratios: $v_1 = 0.3$ and $v_2 = 0.2571$. It is observed that the results are also accurate to within a few percent relative errors in Table 6.5, which demonstrates again the effectiveness of

singular ES-FEM for bimaterial interface cracks.

Table 6.5. Centre-crack under remote tension: material mismatch study.

E_1 / E_2	ε	Singular ES-FEM			Exact solution		
		K_I / K_0 (% error)	K_{II} / K_0 (% error)	G / G_0 (% error)	$\frac{K_I}{K_0}$	$\frac{K_{II}}{K_0}$	$\frac{G}{G_0}$
2	0.0249	0.9995 (0.12)	0.0327 (0.64)	2.1497 (0.25)	1.0007	0.0325	2.1551
4	0.0516	1.0016 (0.14)	0.0678 (0.72)	1.7633 (0.29)	1.0030	0.0673	1.7684
8	0.0699	1.0039 (0.17)	0.0915 (0.36)	1.5620 (0.35)	1.0056	0.0912	1.5675
20	0.0833	1.0060 (0.19)	0.1088 (0.16)	1.4375 (0.41)	1.0079	0.1086	1.4434
40	0.0883	1.0072 (0.17)	0.1151 (0.03)	1.3959 (0.39)	1.0089	0.1151	1.4013
100	0.0914	1.0081 (0.14)	0.1192 (0.11)	1.3712 (0.33)	1.0096	0.1191	1.3758
1000	0.0933	1.0089 (0.11)	0.1217 (0.05)	1.3569 (0.26)	1.0100	0.1216	1.3604

Next, the bimaterial plate problem is condidered to be under remote shear tractions with the geometry size, crack configuration and boundary conditions as shown in Figure 6.8. In the computation, full model is considered to demonstrate the computational strategy for problems containing more than two crack tips. The same material parameters as before are used in this case: $E_2 / E_1 = 22$, $\nu_1 = 0.3$ and $\nu_2 = 0.2571$, and plane strain conditions are considered. The exact solution under pure shear loading ($\sigma_{22}^{\infty} = 0$) is obtained from equation (6.49).

$$K_0 = \tau_{22}^{\infty}\sqrt{\pi a} \quad G_0 = \frac{(\tau_{22}^{\infty})^2 a}{E_1} \tag{6.54}$$

$$\frac{K_1}{K_0} = \pm 0.1097 \quad \frac{K_2}{K_0} = 1.008 \qquad \frac{G}{G_0} = 1.4358 \tag{6.55}$$

where K_I is positive at the left crack tip and negative at the right crack tip. The specimen dimensions are set as: $a = 1$ and $W / a = 30$. Similar to the previous test, five

structured meshes with a/h: (3.0, 4.0, 6.0, 8.0 and 10.0) are considered here as well; All the studies, except domain independence study, are conducted using the domain radius parameter $r_k = 4$.

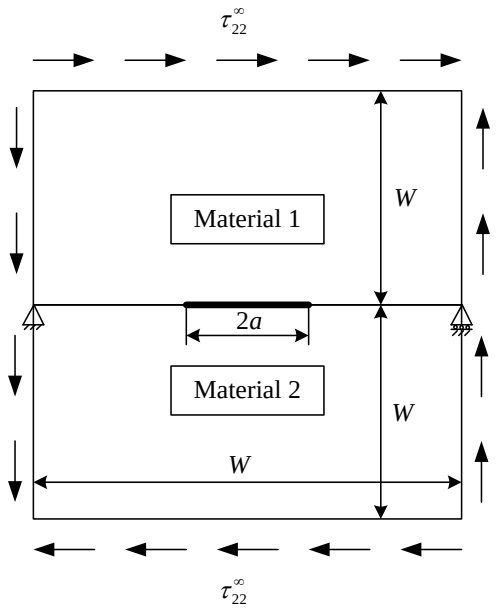

Figure 6.8. Centre-crack under remote shear

The SIFs and the energy release rate obtained using different numerical methods are compared in Table 6.6.

Table 6.6. Centre-crack under remote shear: comparison of stress intensity factors and energy release rate using the singular ES-FEM (SES-FEM), the standard FEM and ES-FEM.

Exact solution	Mesh (a/h)	3.0 (% error)	4.0 (% error)	6.0 (% error)	8.0 (% error)	10.0 (% error)
$K_I / K_0 = -0.1097$	FEM-T3	-0.1310 (19.4)	-0.1284 (17.0)	-0.1240 (13.0)	-0.1214(10.6)	-0.1196 (9.0)
	ES-FEM	-0.1215 (10.7)	-0.1185 (8.0)	-0.1155 (5.3)	-0.1141 (4.0)	-0.1132 (3.2)
	FEM-T6	-0.1109 (1.1)	-0.1108 (1.0)	-0.1105 (0.7)	-0.1104 (0.6)	-0.1103 (0.5)
	Sing ES-FEM	-0.1109 (1.1)	-0.1108 (1.0)	-0.1105 (0.7)	-0.1104 (0.6)	-0.1103 (0.5)
$K_2 / K_0 = 1.008$	FEM-T3	0.9789 (2.9)	0.9823 (2.6)	0.9889 (1.9)	0.9931 (1.5)	0.9957 (1.2)
	ES-FEM	0.9937 (1.4)	0.9977 (1.0)	1.0015 (0.7)	1.0034 (0.5)	1.0045 (0.4)
	FEM-T6	1.0029 (0.5)	1.0041 (0.4)	1.0057 (0.3)	1.0065 (0.2)	1.0069 (0.1)
	Sing ES-FEM	1.0037 (0.4)	1.0050 (0.3)	1.0062 (0.2)	1.0068 (0.1)	1.0072 (0.1)
$G / G_0 = 1.4358$	FEM-T3	1.3611 (5.2)	1.3693 (4.6)	1.3861 (3.5)	1.3967 (2.7)	1.4034 (2.3)
	ES-FEM	1.3984 (2.6)	1.4086 (1.9)	1.4184 (1.2)	1.4233 (0.9)	1.4262 (0.7)
	FEM-T6	1.4214 (1.0)	1.4247 (0.8)	1.4292 (0.5)	1.4314 (0.3)	1.4325 (0.2)
	Sing ES-FEM	1.4231 (0.9)	1.4268 (0.6)	1.4301 (0.4)	1.4318 (0.3)	1.4328 (0.2)

It can be seen again that the SIFs and energy release rate of singular ES-FEM approach the exact solutions more than that of standard FEM and ES-FEM, at the same mesh. Moreover, the maximum relative error of all these values obtained by the singular ES-FEM is only 1.1 % even at the relative coarse mesh.

In Table 6.7 domain independency in the SIFs using the singular ES-FEM is also studied for this shear loading. We can observe domain independence of the SIFs at both the left and right crack tip for $r_k > 3$. Again, the singular ES-FEM results are found to be in good agreement with the reference solutions. Results of the material mismatch study are also conducted and given in Table 6.8. Excellent agreement between the normalized K_I, K_{II} and G computed by the singular ES-FEM and the exact correspondence is realized for a wide range of material combinations ($E_1 / E_2 = 2 \sim 1000$).

Table 6.7. Centre-crack under remote shear: domain independence study

Crack tip	r_k	K_I / K_0 (% error)	K_{II} / K_0 (% error)	G / G_0 (% error)
Left (A)	2	0.1051 (4.26)	1.0085 (0.1)	4.2619 (0.1)
	3	0.1098 (0.04)	1.0051 (0.3)	1.4267 (0.6)
	4	0.1098 (0.08)	1.0054 (0.3)	1.4275 (0.6)
	5	0.1098 (0.06)	1.0053 (0.3)	1.4274 (0.6)
Right (B)	2	-0.1099 (0.1)	1.0122 (0.4)	1.4467 (0.8)
	3	-0.1095 (0.2)	1.0073 (0.1)	1.4329 (0.2)
	4	-0.1104 (0.6)	1.0068 (0.1)	1.4318 (0.3)
	5	-0.1103 (0.5)	1.0067 (0.1)	1.4315 (0.3)

Table 6.8. Centre-crack under remote shear: material mismatch study *.

E_1 / E_2	ε	Singular ES-FEM			Exact solution		
		K_I / K_0 (% error)	K_{II} / K_0 (% error)	G / G_0 (% error)	$\frac{K_I}{K_0}$	$\frac{K_{II}}{K_0}$	$\frac{G}{G_0}$
2	0.0249	-0.0318 (2.2)	0.9989 (0.2)	2.1473 (0.4)	-0.0325	1.0007	2.1551
4	0.0516	-0.0671 (0.3)	1.0013 (0.2)	1.7622 (0.4)	-0.0673	1.0030	1.7684
8	0.0699	-0.0916 (0.5)	1.0040 (0.2)	1.5622 (0.3)	-0.0912	1.0056	1.5675
20	0.0833	-0.1092 (0.6)	1.0066 (0.1)	1.4393 (0.3)	-0.1086	1.0079	1.4434
40	0.0883	-0.1157 (0.6)	1.0078 (0.1)	1.3977 (0.2)	-0.1151	1.0089	1.4013
100	0.0914	-0.1199 (0.6)	1.0085 (0.1)	1.3725 (0.2)	-0.1191	1.0096	1.3758
1000	0.0933	-0.1224 (0.6)	1.0090 (0.1)	1.3573 (0.2)	-0.1216	1.0100	1.3604

* The SIFs and the exact energy release rate are from the right crack tip.

6.6.2 Film/substrate system by the four point bending test

The second example is a film/substrate system with the four point bending test. Owing to symmetry, one half of the specimen is used in the computation. The specimen dimensions, crack orientation, loading and the displacement boundary conditions are given in Figure 6.9. The thickness of film is h_f and that of the substrate is h_s, with the

total thickness denoted by h_t. E_f and v_f are used to denote Young's modulus and Poisson's ratio of film. E_s and v_s are the corresponding properties for the substrate.

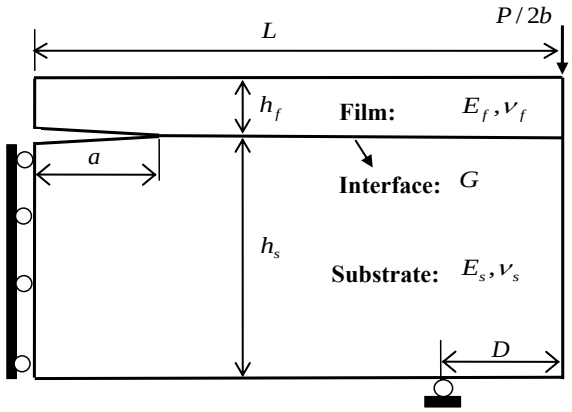

Figure 6.9. Schematic-diagram of film/substrate system by four point bending test (half model)

When the interface crack length significantly exceeds the thickness of the film, steady state conditions are reached and the energy release rate stabilizes to a constant value, G_{ss}, the steady state energy [103]:

$$G_{ss} = \frac{3(1-v_s^2)P^2L^2}{2E_s b^2 h_t^3}\left\{\left(\frac{h_t}{h_s}\right)^3 - \lambda\left[\left(\frac{h_f}{h_t}\right)^3 + \lambda\left(\frac{h_s}{h_t}\right)^3 + 3\lambda\frac{h_f h_s}{h_t^2}\left(\frac{h_f}{h_t} + \lambda\frac{h_s}{h_t}\right)\right]\right\} \quad (6.56)$$

where b is the depth of film/substrate system and λ is defined as:

$$\lambda = \frac{E_s(1-v_f^2)}{E_f(1-v_s^2)} \quad (6.57)$$

The phase angle is computed by taking the characteristic length l given in equation (6.8) to be the total thickness of film/substrate system h_t:

$$\psi = \tan^{-1}\left(\frac{\mathrm{Im}[\mathbf{K}h_t^{i\varepsilon}]}{\mathrm{Re}[\mathbf{K}h_t^{i\varepsilon}]}\right) \quad (6.58)$$

In addition, we also choose the factors K_0 and G_0 are used to normalize the SIFs and the energy release rate, respectively.

$$K_0 = \frac{PL}{bh_t^{3/2}} \qquad G_0 = \frac{(1-\nu_s^2)P^2L^2}{E_s b^2 h_t^3} \tag{6.59}$$

In the numerical model, the depth b is taken to be unity, $h_f = 1$, $h_t / h_f = 10$, $L/D = 2.5$, $D/h_t = 5$ and $a/h_t = 3$. Thus, the problem domain is $L \times h_t = 125 \times 10$ and $a = 30$. The material parameters are $E_f / E_s = 10$ and $\nu_f = \nu_s = 0.3$. The mesh with $h_t / h = 6.0$ and the domain radius parameter $r_k = 4$ are used. Based on this, the exact steady state energy release rate is 1.3632 from equation (6.56). Comparison of energy release rates obtained by standard FEM, ES-FEM and singular ES-FEM are presented in Table 6.9.

Results for K_I, K_{II} and ψ are also indicated for completeness. From the results, it is found again that the singular ES-FEM provide more accuracy of energy release rate compared to the standard FEM, ES-FEM and FEM-T6 using the singular elements. Moreover, the energy release rate obtained by the singular ES-FEM is in good agreement with the exact value [103] with a fraction of percent error.

Table 6.9. Film/substrate system by four point bending test: comparison of stress intensity factors and energy release rate using the singular ES-FEM (SES-FEM), the standard FEM and ES-FEM under the same triangular mesh with $h_t / h = 6.0$ *.

Method	K_I / K_0	K_{II} / K_0	ψ	G / G_0 (% error)
FEM	0.9386	1.2832	43.81	1.3142 (3.6)
ES-FEM	0.9517	1.2946	43.68	1.3423 (1.5)
FEM-T6	0.9564	1.2965	43.54	1.3502 (0.9)
Sing ES-FEM	0.9572	1.2970	43.57	1.3511 (0.8)

* The exact energy release rate from equation (6.56) is 1.3632.

Then, the fixed total thickness $h_t = 10$ is used and the thickness ratio h_f / h_t is varied from 0.1 to 0.5. Also, we varied the material properties combinations of film and substrate. Table 6.9 lists the steady state energy release rate for different thickness ratio and different material combinations. Again, we can observe that all the results by the singular ES-FEM are in excellent agreement with the corresponding reference solutions, and the relative errors are less than 1 percent.

Table 6.10. Film/substrate system by four point bending test: effect of thickness ratio.

		Singular ES-FEM				Exact solution
$\frac{E_f}{E_s}$	$\frac{h_f}{h_s + h_f}$	K_I / K_0	K_{II} / K_0	ψ	G / G_0 (% error)	$\frac{G}{G_0}$
	0.1	0.9572	1.2970	43.57	1.3511 (0.8)	1.3632
	0.2	1.2948	1.6356	41.63	2.2626 (0.7)	2.2793
10	0.3	1.7766	1.9884	38.22	3.6969 (0.7)	3.7254
	0.4	2.4676	2.4454	34.74	6.2754 (0.8)	6.3249
	0.5	3.4789	3.1173	31.86	11.3451 (0.9)	11.4523
	0.1	0.0729	0.1000	63.90	0.0801 (0.9)	0.0807
	0.2	0.1618	0.1787	57.85	0.3022 (0.7)	0.3043
0.1	0.3	0.3024	0.2844	53.25	0.8959 (0.5)	0.9010
	0.4	0.5295	0.4372	49.55	2.4518 (0.5)	2.4655
	0.5	0.8949	0.6661	46.66	6.4706 (0.8)	6.5228

6.7 Summary

In this chapter, a singular edge-based smoothed finite element method (ES-FEM) is used to solve problems with mix-mode interface cracks between two dissimilar isotropic materials. A five-node singular element is designed within the framework of ES-FEM to construct the singular shape functions. To model the oscillatory effect $r^{i\varepsilon}$ at the crack tip,

the mix-mode SIFs are numerically extracted by the domain form of interaction integral with appropriate modifications. Through the formulation and numerical examples, some conclusions can be drawn as follows:

1. In the Gauss integrations for computing the stiffness matrix, at least 5 gauss points should be used along one segment of the smoothing domain for the 5-node singular element to ensure the accurate results.

2. Domain independence of the SIFs are observed for the domain radius excluding the crack tip elements.

3. The singular ES-FEM significantly improves the accuracy of stress intensity factors and energy release rate in comparison with the standard FEM and ES-FEM.

4. Excellent agreement between the numerical results and reference solutions with less than 1 percent relative error was realized for a wide range of material combinations and boundary conditions. This indicates that singular ES-FEM can solve the interface crack problems effectively.

Chapter 7: Crack propagation analysis using Singular Edge-based Smoothed Finite Element Method (Singular ES-FEM)

"It's easy to come up with new ideas; the hard part is letting go of what worked for you two years ago, but will soon be out of date."

Roger von Oech

7.1 Introduction

In the previous chapters, the new method of singular ES-FEM for stationary crack problems in both bimaterial and isotropic materials was introduced and different aspects of the method were investigated through several examples.

In this chapter the method is even further developed to simulate the quasi-static crack growth on top of the stationary crack analysis. For the sake of simplicity in automation of mesh generation, the standard Delaunay triangulation is adopted with a set of unique (no over-lapping and no-gaping) triangles, edges and nodes. In order to implement the singular ES-FEM, one layer of 5-node crack tip elements is then created by adding one additional node on the crack tip edges. Stress intensity factors are computed using the developed method of singular ESFEM developed for the stationary crack problems.

These values are then plugged in the maximum circumferential criterion to predict the crack growth direction.

As a more practical case study, fatigue crack growth is further analyzed using the developed approach. Simulating fatigue problems undergoing varying loads, trajectory and crack growth rate parameter are predicted adopting two different models of Forman and Kujawski. The results are finally compared with the reference observations and an excellent agreement is exhibited in all the studied cases.

Because triangular mesh is used, re-meshing near the crack-tip can be automated. In addition, because of using singular ES-FEM, the stability, accuracy and efficiency are ensured. It will be seen that singular ES-FEM is able to successfully predict sufficiently accurate path of the crack during propagation.

7.2 Formulation

As it was mentioned in previous chapters, the method of area-path interaction integral [97, 104] is properly used in the settings of singular ES-FEM to accurately evaluate the stress intensity factors for the stationary crack problems.

Using the developed method for the stationary crack problems, a quasi-static crack growth can be simulated by dividing the propagation process into several numbers of stationary states, solving each state and predicting the crack growth direction at the next step based on the current solutions and through a criterion for the crack geometry updating. In the present study, the maximum circumferential stress criterion is adopted to determine the crack growth direction [105]. According to this criterion, for isotropic materials under mixed-mode loading, the crack will propagate in a direction normal to

maximum circumferential stress. Since this stress is the principle stress, the direction of crack growth can be evaluated by setting the shear stress to zero and solving the resultant equation

$$K_I \sin\theta + K_{II}(3\cos\theta - 1) = 0 \tag{7.1}$$

Where θ is the crack growth angle and K_I and K_{II} are, respectively, the stress intensity factors related to the first and second fracture mode. This equation yields the crack growth direction as [106]:

$$\theta = \pm\cos^{-1}\left\{\frac{3K_{II}^2 + K_I\sqrt{K_I^2 + 8K_{II}^2}}{K_I^2 + 9K_{II}^2}\right\} \tag{7.2}$$

In which

$$|\theta| \le \frac{\pi}{2} \tag{7.3}$$

In addition, in order to making ensure that the opening stress associated with the crack direction of the crack extension is maximum, the sign of θ should be opposite to the sign of K_{II}, as it is illustrated in Figure 7.1.

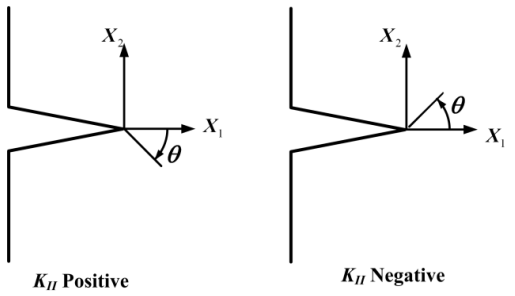

Figure 7.1. direction of crack growth at a typical sub step

In this study, the length of crack increment Δa is the only arbitrary parameter and usually is taken as $10\%-20\%$ of the initial crack length a, inversely proportional to the ratio of $\left|K_{II}/K_{I}\right|$. However, this range of percentage can be changed appropriately depending on the problem. For instance, some researchers used the range $20\%-50\%$ in their studies [107, 108]. Generally, by choosing a smaller length of increment, the trajectory of crack growth will be predicted more precisely, particularly in the regions where ratio of $\left|K_{II}/K_{I}\right|$ is relatively high.

For the fatigue analysis, as it was mentioned before, another additional model is required to predict the fatigue crack growth rate under the loading condition and for different cycles of load. It is almost impossible, however, to introduce a unique model capable of successfully simulating the behavior of all materials under all arbitrary loading condition. Therefore, numerous models have been proposed by researchers. In the present thesis, two different models of Forman and Kujawski are adopted. Based on Forman model, crack growth rate is a function of stress ratio, critical stress intensity factor, and stress intensity factor range as

$$\frac{da}{dN}=\frac{C_F(\Delta K)^{n_F}}{(1-R)K_c-\Delta K} \tag{7.4}$$

While in the Kujawski's model, another term of $\left(\Delta \mathrm{K}^{+}.\mathrm{K}_{\max}\right)^{0.5}$ is introduced as crack growth driving force and is defined as follows;

$$\frac{da}{dN}=C_K(PK)^{m_K} \tag{7.5}$$

In which

$$PK = (\Delta K^{+}.K_{\max})^{0.5} \;;\; \begin{cases} \Delta K^{+} = \Delta K & for\ R \geq 0 \\ \Delta K^{+} = K_{\max} & for\ R < 0 \end{cases} \quad \& \quad K_{\max} = \frac{\Delta K}{1-R} \qquad (7.6)$$

7.3 Adaptive procedure

An algorithm for the propagation analysis using standard Delaunay triangulation procedure is developed that is shown in Figure 7.2. The algorithm contains the following main steps;

1) At the initial stage with given initial crack of length *a*, a mesh is generated including 4 to 5 layers of fine mesh at the crack tip and the coarse one at the rest areas of domain.
2) One more node is then added in each edge directly connected to the crack tip node to create one layer of 5-node specially designed crack tip elements.
3) The singular ES-FEM is then implemented and stress intensity factors are efficiently computed.
4) Based on the stress intensity factors evaluated in the previous step, crack growth direction is predicted using "maximum circumferential stress criterion".
5) In order to coarsen the mesh, a criterion is used to smooth the new portion of crack surface. This criterion compares the predicted crack angle calculated at step 4 with the current crack direction (Let name them θ_{i+1} and θ_i, respectively). Based on this criterion; if $|\theta_{i+1} - \theta_i| > 0.001\ rad$, the current crack tip node is split into two separated nodes and a new crack tip position is assigned using an increment of crack with the length da in the predicated direction θ_{i+1}. If

$\left|\theta_{i+1}-\theta_i\right| \le 0.001\ rad$, however, the new crack tip position is assigned using the increment da in the same direction θ_i. The current crack tip node is then omitted and the new portion will be generated by connecting the new crack tip node to two nodes on the current crack surface which are directly connected to the current crack tip node.

6) Steps 1-5 are repeated until the entire path of the crack growth in problem domain is produced.

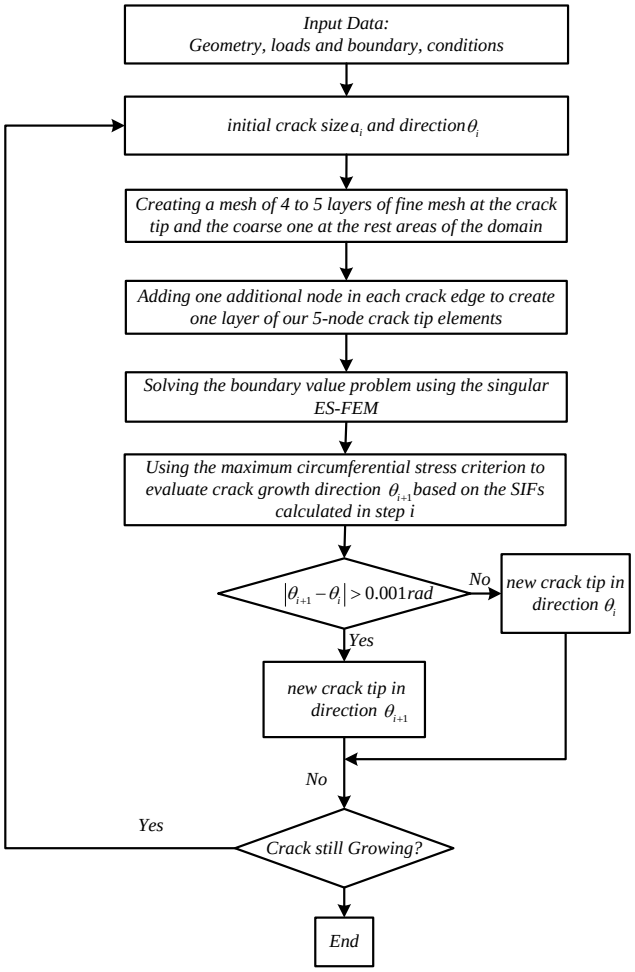

Figure 7.2. The procedure of delaunay triangulation for the singular ES-FEM

In our adaptive simulation process, we use a very coarse mesh in the major part of the problem domain, and only at the vicinity of the crack tip a few layers (4-5 layers) of fine and well controlled mesh is generated. This fine "crack tip mesh" moves together with propagating crack to ensure the quality solution of stress intensity values and, hence, the next crack growth direction. The entire process can be coded with ease and implemented automatically.

For the fatigue analysis, a very similar approach is implemented. Two different models of Forman and Kujawski are used in the present fatigue prediction approach to determine the crack growth rate for the structures under varying-amplitude service load. The procedure is illustrated in flowchart of Figure 7.3.

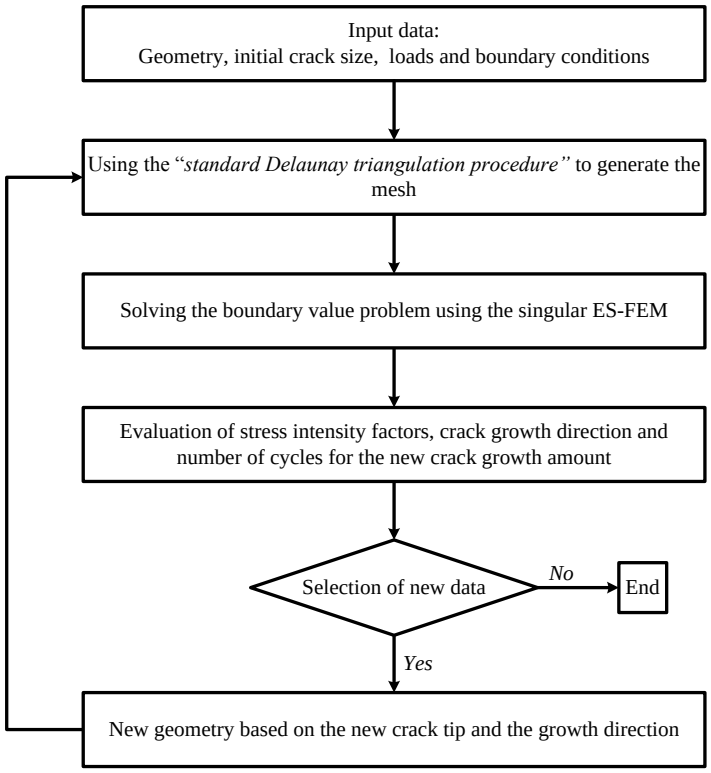

Figure 7.3. The algorithm for the fatigue analysis using the singular ES-FEM

7.4 Numerical examples

In this section some examples are presented to investigate the capability of singular ES-FEM in simulation of crack growth problems through a quasi-static process. A code for crack growth path prediction is developed following the formulation given in section 7.2 and the procedure given in section 7.3. The mesh generations, node creation, mesh smoothing and adaptive re-meshing is based on the standard Delaunay triangulation procedure. A comparison between final state of problems and the reference observations clearly shows that the presented singular ES-FEM is capable of accurately predict crack growth trajectory.

7.4.1 Crack growth in an edge cracked plate

The code is first applied to simulate the crack growth in an edge cracked plate. Geometry, loading, and boundary condition of the plate is exactly identical to the example presented in section 5.7.7; meaning that it is clamped at the bottom and undergoes a shear load at its top edge creating a mixed-mode situation of fracture. The length of crack increment at each step of solution is fixed to $da = 0.1\,mm$. Figure 7.4 shows the predicted crack trajectory using singular ES-FEM at different steps of crack growth as well as final state of problem which closely resembles the numerical solutions in Ref. [108, 109]. As it can be seen in this figure, the crack growth is not symmetrical due to the unsymmetrical loading and boundary condition. The entire crack propagation is gained after 39 steps. The obtained results clearly show that the present singular ES-FEM is able to predict the stress intensity factors and simulate the crack path accurately. Note that, all the results have been obtained using a largely coarse mesh which can save

the computational time. This can be done only because of the high accuracy that singular ES-FEM offers when the linear triangular elements are adopted. In the other words, if the same set of elements and nodes are used for the standard FEM, the results will be of less accuracy.

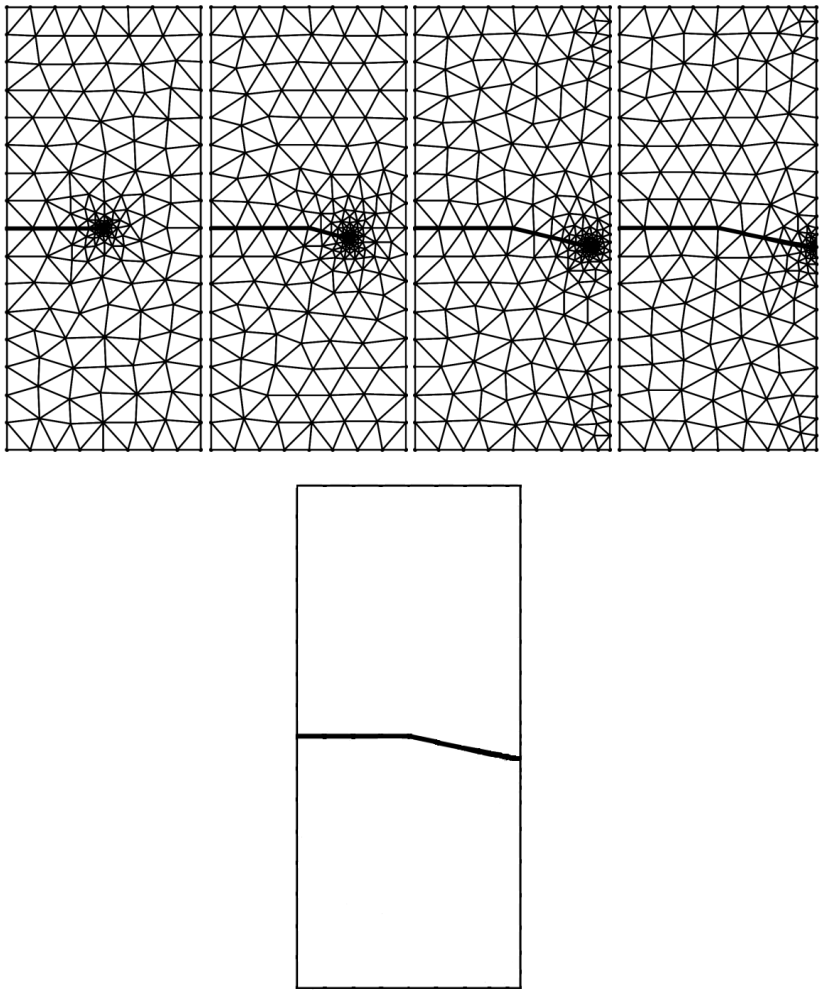

Figure 7.4. Crack growth trajectory at different steps using singular ES-FEM for the single edge cracked plate

7.4.2 Crack growth in a cracked cantilever beam

The quasi-static crack growth for a double cantilever beam illustrated in Figure 7.5 is studied for further evaluating the ability of singular ES-FEM to predict the crack growth trajectory.

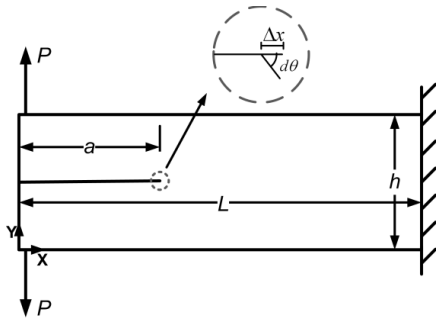

Figure 7.5. Double cantilever beam with a small perturbation angle at the crack tip

The cantilever beam has the dimensions of $L = 11.8\,mm$, $h = 3.94\,mm$ and $a = 3.94\,mm$, and is subjected to the tensile load of $P = 197\,N$. In addition, plane stress condition is assumed with Young's modulus and Poisson's ratio of $E = 3\times10^7\ N/mm^2$ and $\nu = 0.3$, respectively. The crack is given a small perturbation of length $\Delta x = 0.3\,mm$ at the tip with initial angle of $d\theta$ as shown in the figure. This perturbation contributes second mode of fracture in the problem state and leads to a mixed mode problem situation, deflecting crack trajectory from straight-horizontal path during the propagation. Figure 7.6 shows the crack path at several steps for the case in which $d\theta = 0.1\,rad$ and $da = 0.2\,mm$, where da is the length of crack increment at each step of crack growth process. Moreover, another study has been conducted to examine the effect of $d\theta$ as well as da on the crack propagation trajectory. Figure 7.7 shows how the crack trajectory will

vary when different initial perturbation slopes are implemented. It should be mentioned that the length of crack increment is fixed to $da = 0.1\,mm$ for all the reported cases in this figure. It is clearly highlighted from this figure that the crack trajectory will vary when the initial crack geometry changes. For the case in which $d\theta = 0\ rad$ the problem is under pure mode *I* situation and the crack propagates on a horizontal and straight line. By increasing the slope of initial perturbation, however, second mode of fracture plays a more important role and crack trajectory bends more. Figure 7.8 also shows the crack trajectories when the length of crack increment is changed, while the initial perturbation is fixed to $d\theta = 0.1\ rad$. It can be observed from this figure that the numerically predicted crack trajectories can be somewhat affected by the length of crack increment; however, for the small enough increments the variation in the paths can be ignored. All the results are in a good agreement with those in some other studies [110, 111]. The quality of our solution is very well controlled using triangular mesh with the singular ES-FEM ensuring the accuracy.

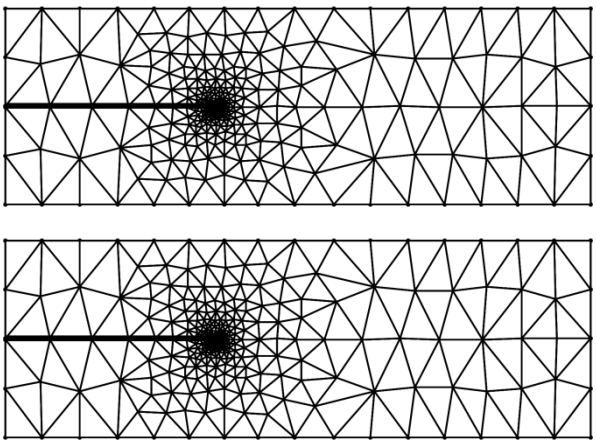

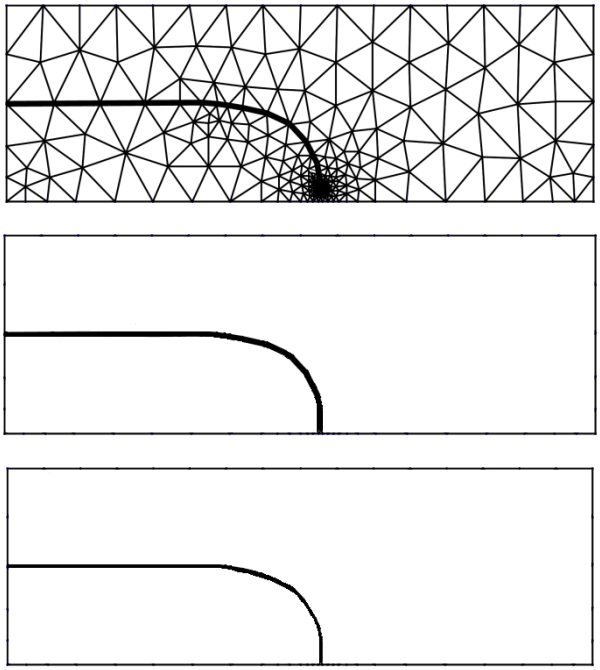

Figure 7.6. Crack growth trajectory at different steps using singular ES-FEM for the single edge cracked plate; The first 4 schemes in this figure have been obtained by singular ES-FEM while the last has been reported by experiments [110, 111]

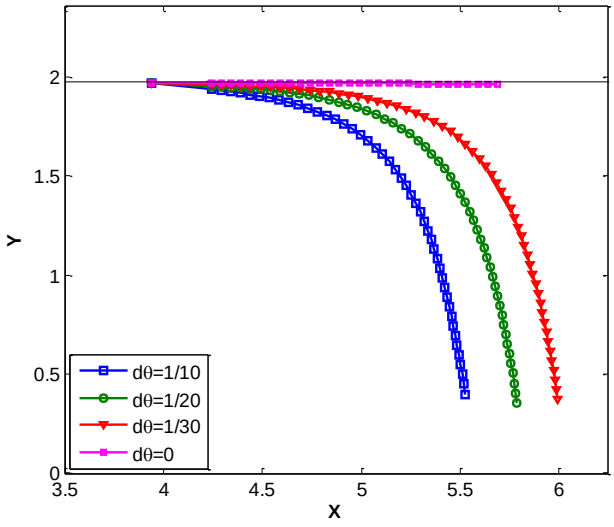

Figure 7.7. Crack propagation trajectories for different initial perturbation angles
(The unit of the angles $d\theta$ is *rad*)

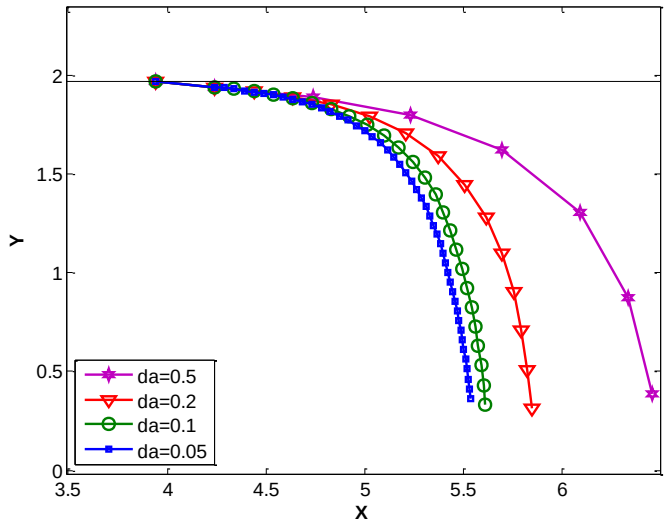

Figure 7.8. Influence of crack growth increment on crack propagation trajectory

7.4.3 Crack growth in a PMMA Specimen

The PMMA beam specimen has been examined as another benchmark with the available experimental observations by Bittencourt et al. [107]. The geometry and boundary conditions have been shown in Figure 7.9.

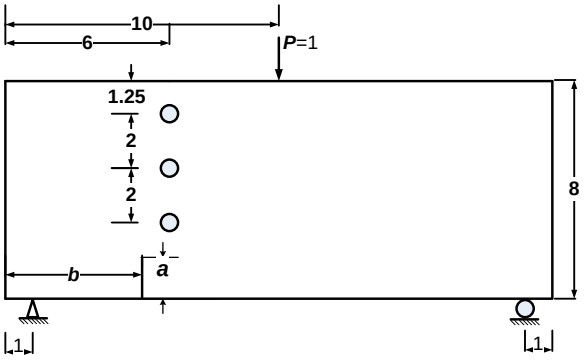

	a	b
Case I	1.0	4.0
Case II	1.5	5

Figure 7.9. Problem statement for the PMMA specimen

The material properties for this specimen are $E = 3\times10^4 MPa$ and $\nu = 0.3$, respectively. Two different settings of *a* and *b* (See, Figure 7.9) is adopted for the problem and crack is quasi-statically grown using singular ES-FEM with *S-SD*=1. Moreover, the length of crack increment is set to $da = 0.05\,mm$ for the solution steps in which shear mode of fracture tends to increase and $\left|K_{II}/K_I\right| \geq 0.2$ (similar to what happens near the holes). The length of increment is set to $da = 0.1\,mm$, however, when the opening mode of fracture is much more effective and $\left|K_{II}/K_I\right| < 0.2$. This kind of setting for the increment length helps to predict the crack trajectory more accurately.

The results are shown in Figure 7.10 and Figure 7.11. According to these results, in the first studied case, the crack passes above the lower hole and ends to the middle hole from the left side. In the second case, however, it passes through the material between lower and middle hole and approaches the middle hole from the right side. Moreover, the completely propagated crack in the first case has been obtained after 30 solution steps, while for the second case this number is 59 steps. This is due to the considerable increase in the shear (second) stress intensity factor around the holes of the second case which forces us to decrease the increment length occasionally. The results of the crack trajectory during the propagation have an excellent agreement with the experimental results given by Bittencourt et al. [107]. This excellent agreement between our results and reference observations reinforces again the claim that singular ES-FEM accurately predicts the stress intensity factors and successfully simulates the quasi-static crack growth problems by using a largely coarse base mesh of linear triangular elements.

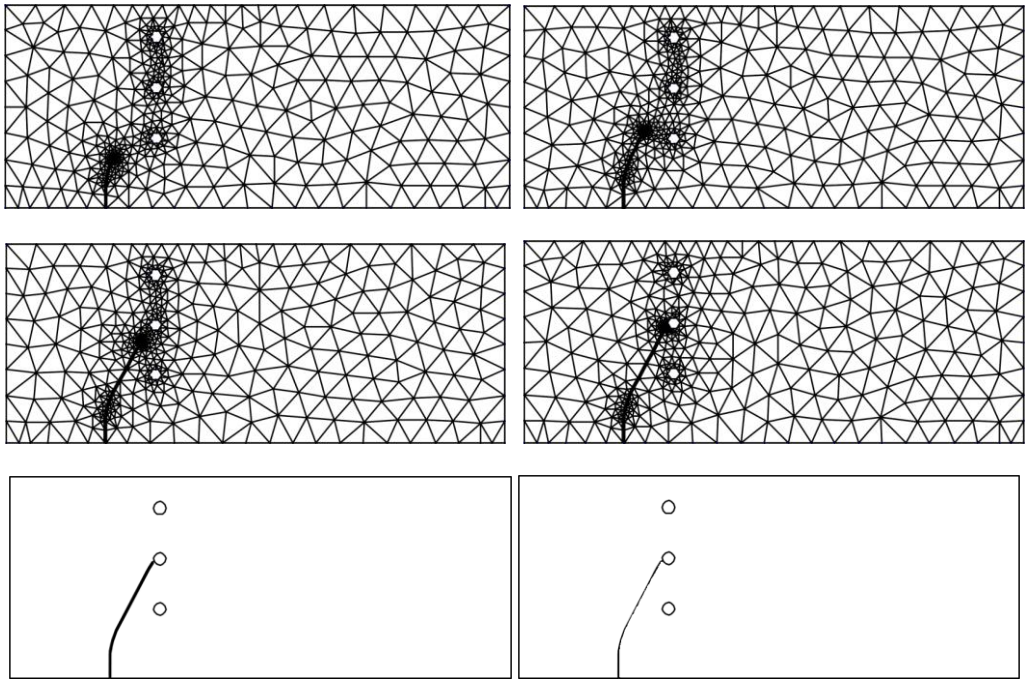

Figure 7.10. Crack growth trajectory at different steps for PMMA specimen (case I). The first 5 schemes in this figure have been obtained by singular ES-FEM while the last has been reported by experiments [107]

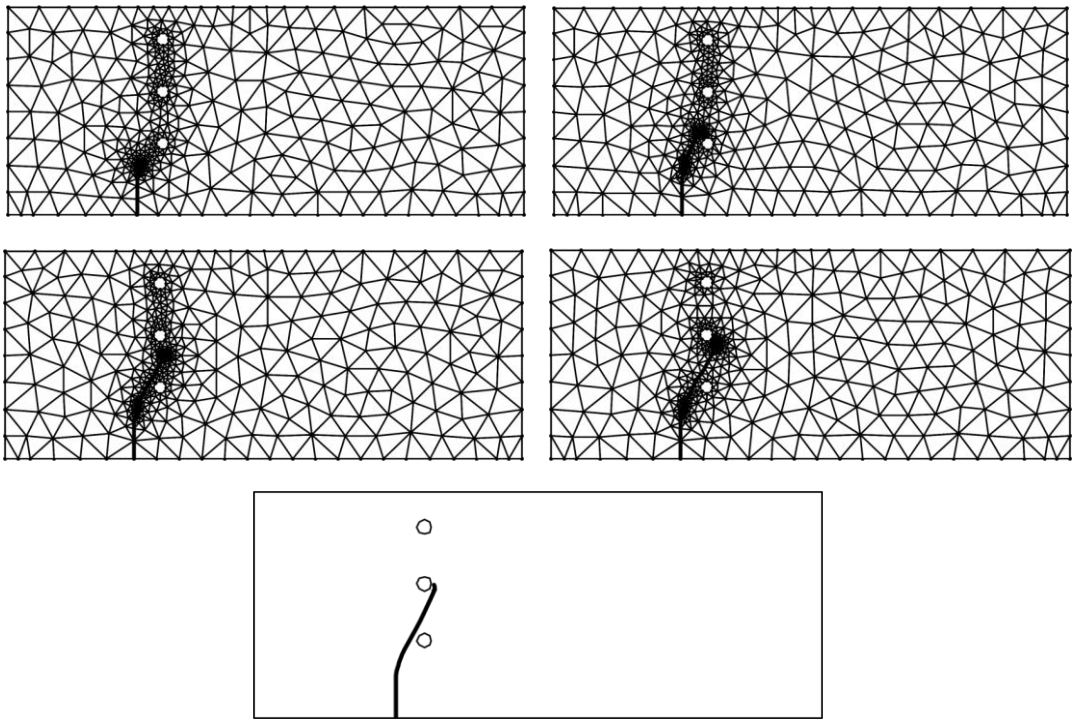

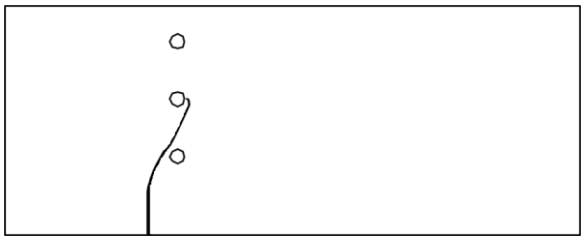

Figure 7.11. Crack growth trajectory at different steps for PMMA specimen (case II). The first 5 schemes in this figure have been obtained by singular ES-FEM while the last has been reported by experiments [107]

7.4.4 Fatigue analysis of a single-edge notched specimen using Forman model and Singular ES-FEM

A single-edge notched specimen as shown in Figure 7.12 is analyzed to examine the capacity of the method for prediction of crack behavior during a fatigue failure. The problem is solved under mode *I* loading with a load ratio of $R = 0.1$ while the specimen undergoes a sinusoidal load P.

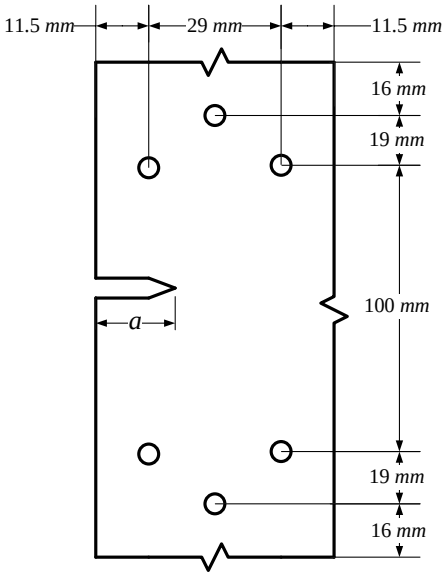

Figure 7.12. A single-edge notched specimen

The fatigue crack propagation is then simulated by adopting the Forman model. In order to verify the accuracy of results, the findings are compared with those from experimental data reported by Mohanty et al. [25] for the same geometry, load, boundary condition and material properties. Similar to that reference, the problem has been solved for two aluminum alloys of "Al7020-T7 "and "Al2024-T3". The Mechanical properties of materials, values of the Forman constants and load scenarios are listed in Table 7.1 and Table 7.2.

Table 7.1. Mechanical properties of 7020-T7 and 2024-T3 Al-alloys

Material	Young's modulus $E(MPa)$	Poisson's ratio ν	Plane strain fracture toughness $K_{IC}(MPa\sqrt{m})$	Plane stress fracture toughness $K_{IC}(MPa\sqrt{m})$
7020-T7 Al-alloy	70000	0.33	50.12	236.8
2024-T3 Al-alloy	73100	0.33	37.0	95.31

Table 7.2. Forman constants and load scenarios

Material	$C_F \times 10^5$	m_F	Maximum load $F_{\max}(KN)$	Minimum load $F_{\min}(KN)$	Initial crack length $a(mm)$
7020-T7 Al-alloy	1.33	3.1954	8.89	0.89	18.30
2024-T3 Al-alloy	1.00	3.2094	7.20	0.72	17.75

Length of the crack during the fatigue process as well as behavior of $\frac{da}{dN}$ while ΔK is changing are presented in Figure 7.13 to Figure 7.16. According to these figures it can be easily highlighted that the results of singular ES-FEM have an excellent agreement with the findings from the experimental study.

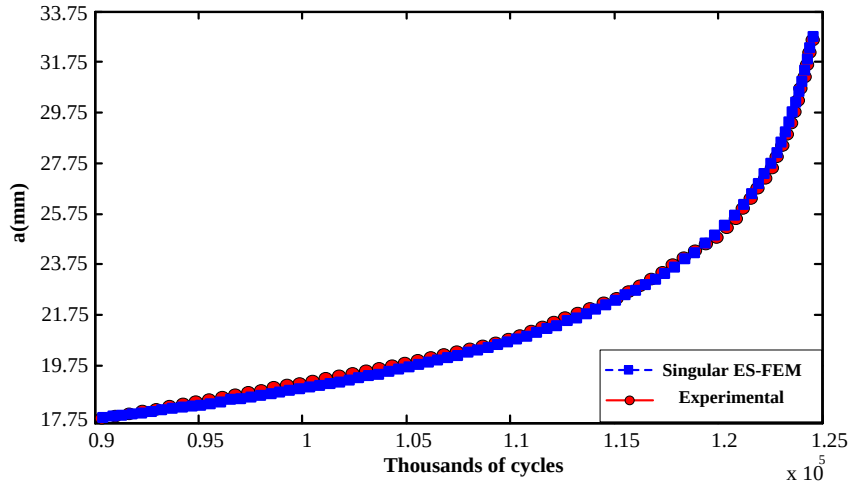

Figure 7.13. Fatigue crack growth for aluminum alloy 2024-T3

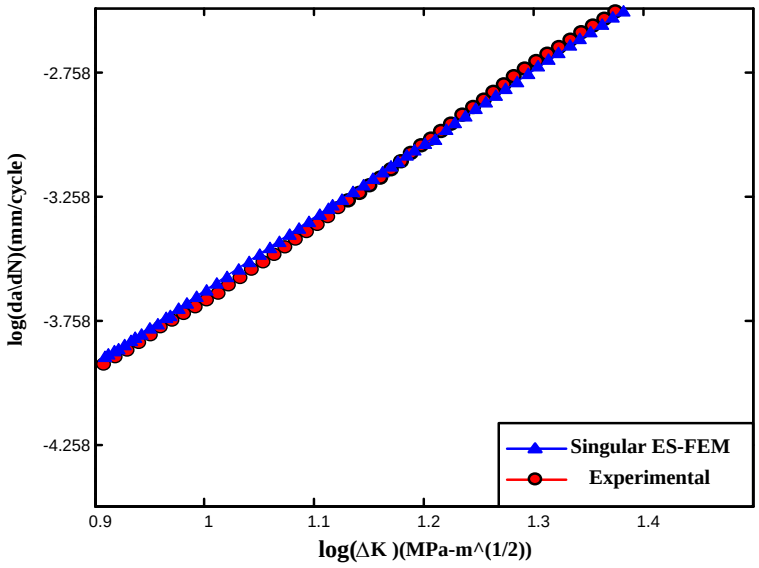

Figure 7.14. Logarithmic behavior of *FCGR* versus stress intensity factor range for aluminum alloy 2024-T3

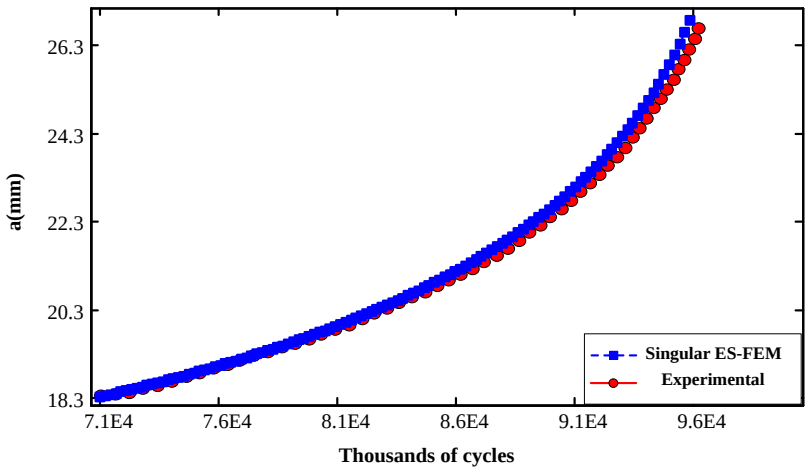

Figure 7.15. Fatigue crack growth for aluminum alloy 7020-T7

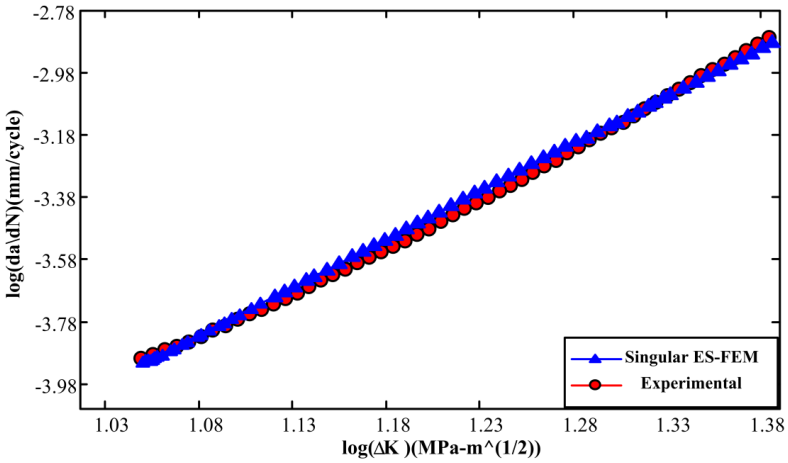

Figure 7.16. Logarithmic behavior of *FCGR* versus stress intensity factor range for aluminum alloy 7020-T7

7.4.5 Kujawski's Model of $\left(\Delta K^{+}.K_{max}\right)^{0.5}$ for aluminum alloy

The same geometry of previous example with the initial crack length of $a = 1\,mm$ is analyzed under the sinusoidal loading with the stress ratio of $R = 0.1$ and maximum load of $F_{max} = 200N$. The material properties consist of $E = 73100\ MPa$ and $\nu = 0.33$. The problem is solved using the singular ES-FEM and the results are compared with those

presented in a study conducted by Maymon [45]. The stress intensity factor in each step has been calculated using the singular ES-FEM and the FCGR has been evaluated adopting the Kujawski's model of $\left(\Delta K^{+}.K_{max}\right)^{0.5}$. The study is performed on the aluminum alloy 2024-T351 and the coefficients C_K and m_K for the material are borrowed from the reference study [45] as $C_K = 7.648179\times10^{-12}$ and $m_K = 4.05$. The results of analysis as well as the collapsed experimental data reported in the reference study of Maymon are illustrated in Figure 7.17. The excellent agreement between the results shows the power of singular ES-FEM for the fatigue crack growth simulation.

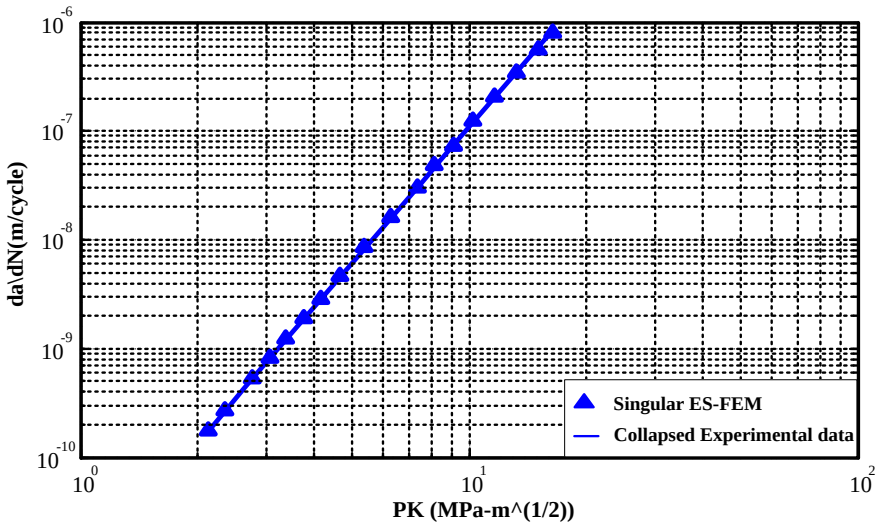

Figure 7.17. The logarithmic behavior of *FCGR* versus Kujawski's parameter PK

7.5 Summary

In this chapter, the method of singular ES-FEM has been employed to simulate the path of crack growth under quasi-static crack propagation. The stress intensity factors in both fracture modes have been calculated using the domain form of interaction integral method in the framework of singular ES-FEM. The method uses a largely coarse base

mesh of linear triangular elements. For simulating the stress and strain field singularity at the crack tip, however, singular ES-FEM implements a new 5-node triangular crack tip element.

For the fatigue analysis, two different models of Forman and Kujawski were adopted to predict the amount of crack growth due to the fatigue phenomenon. In addition, the direction of crack growth was evaluated using the maximum circumferential stress criterion. A standard Delaunay triangulation procedure was then employed for automatically mesh generating and re-meshing process. The comparison of results with the experimental observations exhibits an excellent agreement which confirms the ability of singular ES-FEM to analyze crack growth behavior.

Chapter 8: Singular Face-based Smoothed Finite Element Method (Singular FS-FEM) for the LEFM problems

"Imagination is the beginning of creation. You imagine what you desire, you will what you imagine and at last you create what you will."

George Bernard Shaw

8.1 Introduction

In previous chapters, the method of singular ES-FEM for two-dimensional linear elastic fracture mechanic problems was thoroughly developed for both cases of stationary and quasi-static crack growth simulations. Contrary to the widely used approach of FEM that simulates the singular stress field by mapping between natural and Cartesian coordinates of the so-called "collapsed quadratic elements (quarter-point elements)", in the singular ES-FEM a new 5-node triangular element with a set of specially designed shape functions is introduced to serve the purpose via a simple point interpolation method. In spite of FEM that does not work well with the linear elements, singular ES-FEM is capable of producing accurate results when the linear elements are employed. This is because of taking advantage of strain smoothing technique to develop a softer model than that of FEM.

In the present chapter, a similar approach will be developed to analyze the problems in 3-dimensional space. Instead of exerting iso-parametric mapping over a mesh of

higher order elements, a simple interpolation method is implemented over the strain smoothed domains constructed associated with a background mesh of linear tetrahedral elements. To capture the singularity of stress field, a layer of new specially designed prism element is then used along the crack front line. To connect crack tip prism elements to the base mesh of tetrahedrons, pyramid elements are then suggested to be adopted. The stiffness matrix is accordingly evaluated only by calculating the displacement field (and not the derivatives) over the boundaries of smoothing domains. Similar achievements of singular ES-FEM in analysis of 2-D problems are expected to be observed in 3-D cases when the similar procedure of singular FS-FEM is employed. To investigate this, performance of the method is examined through some examples and results are presented in terms of strain energy and displacement. Furthermore, stress intensity factors are evaluated based on a volume form of 3-D interaction integral approach, and path independency of results is investigated by adopting different domains. As it will be observed, the method works very well with the 3-D interaction integral approach and provides the accurate and path-independent results. The results of strain energy also confirms that singular FS-FEM with the proposed crack tip elements (along the crack front) and the linear tetrahedral elements (at the rest of domain) provides the more accurate results than those of FEM using quadratic and collapsed quadratic elements.

8.2 Displacement interpolation in standard faced-based smoothed finite element method (FS-FEM)

In order to improve the results of FEM using the linear 4-noded tetrahedral elements (T4), the idea of strain smoothing approach similar to that of ES-FEM in 2D space is

exerted in the faced-based smoothed finite element method (FS-FEM). Using the strain smoothing technique in the calculation of system stiffness matrix will result in a softer model than that of FEM using the same background mesh of T4 elements. Furthermore, because of using T4 elements in the FS-FEM model, the process of mesh generation can be done automatically and with ease even for the very complicated geometries. When the FS-FEM is employed, only displacements over the smoothing domains associated with the faces (and not their derivatives) are required to be evaluated. In addition, similar to other S-FEM approaches and despite FEM, in FS-FEM no iso-parametric mapping procedure is required and the stiffness matrices are calculated based on a simple interpolation method.

Not only the smoothing domains creation but also the formulations of FS-FEM imitate the same patterns of ES-FEM. Assuming domain Ω decomposed into N_e number of non-overlap and no-gap tetrahedral domains as $\Omega = \sum_{i=1}^{N_e} \Omega_i^e$ ($\Omega_i^e \cap \Omega_j^e = \varnothing$ *for* $i \neq j$), a new set of N_s non-overlap and no-gap smoothing domains is further created such that $\Omega = \sum_{k=1}^{N_s} \Omega_k^s$ ($\Omega_k^s \cap \Omega_j^s = \varnothing$ *for* $k \neq j$), in which N_s is the total number of faces associated with tetrahedrons of background mesh. In such a discretization method, for every typical face *k*, a unique smoothing domain Ω_k^s is created by simply connecting three endpoints of the triangular face to the center points of the adjacent elements to which the face belongs.

The colored areas in Figure 8.1 schematically show the way of constructing such smoothing domains for two possible cases in which face *k* either belongs to one tetrahedron (as a boundary face) or two (as a common face between two neighbor tetrahedrons). Case (*a*) typically shows the constructed smoothing domain for the dashed face *ACD* which is assumed to be a boundary face and the corresponding Ω_k^s is the volume domain bounded with surfaces *ACD, ACG, DCG, ADG*. Similarly, case (*b*) shows the Ω_k^s associated with face *ABC*. As it can be seen; the smoothing domain is bounded with triangular faces *ACG*, *CGB*, *BGA*, *AHC*, *HCB* and *BAH*, where points *G* and *H* are, respectively, denoted as center points of tetrahedrons *ABCD* and *ABCH*.

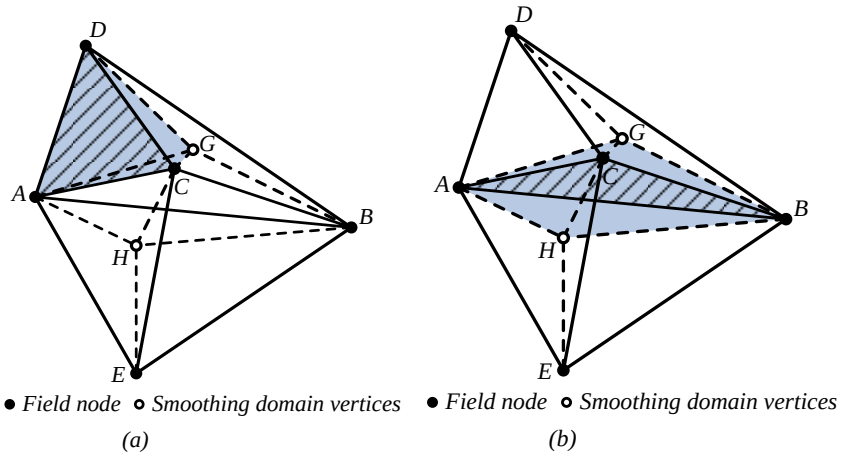

Figure 8.1. Smoothing domain for typical tetrahedral elements faces (a) for boundary face *ADC* (b) for interior face *ABC*

For such a discretized domain, the smoothed strain can be calculated in the following fashion;

$$\bar{\boldsymbol{\varepsilon}}_k(\mathbf{x}) = \int_{\Omega_k^s} \boldsymbol{\varepsilon}^h(\mathbf{x})\Phi_k(\mathbf{x})d\Omega = \int_{\Omega_k^s} \nabla_s \mathbf{u}^h(\mathbf{x})\Phi_k(\mathbf{x})d\Omega \tag{8.1}$$

Where, as before, $\mathbf{u}^h$ is a trial function identical to that of finite element method which can be re-written in the following matrix form

$$\mathbf{u}^h(\mathbf{x}) = \sum_{i=1}^{Np} \mathbf{N}_i(\mathbf{x})\mathbf{d}_i \tag{8.2}$$

Where N_p is number of nodes per the element housing $\mathbf{x}$, $\mathbf{N}_i(\mathbf{x})$ and $\mathbf{d}_i$ are i^{th} component of, respectively, nodal shape function matrix and nodal displacement vector. Moreover, smoothing function Φ_k in equation (8.1) satisfies the unity property as

$$\int_{\Omega_k^s} \Phi_k(\mathbf{x}) d\Omega = 1 \tag{8.3}$$

And can be defined based on the volume V_k^s of the smoothing domain Ω_k^s

$$\Phi_k(\mathbf{x}) = \begin{cases} 1/V_k^s & X \in \Omega_k^s \\ 0 & X \notin \Omega_k^s \end{cases} \tag{8.4}$$

In which the volume V_k^s is calculated as

$$V_k^s = \int_{\Omega_k^s} (\mathbf{x}) d\Omega = \frac{1}{4} \sum_{i=1}^{N_e} V_e^i \tag{8.5}$$

Wherein i is the number of adjacent elements to face k ($i = 1$; if the face is a boundary face, $i = 2$; otherwise), and V_e^i is the volume of i^{th} element next to face *k*. By choosing trial function $\mathbf{u}^h$ satisfying equation (8.2), substituting it in equation (8.1), and smoothing the strain over Ω_k^s corresponding smoothed strain is re-written in the following form

$$\bar{\boldsymbol{\varepsilon}}_k(\mathbf{x}) = \sum_{I=1}^{N_{ns}} \bar{\mathbf{B}}_I \mathbf{d}_I \tag{8.6}$$

Where N_{ns} is the number of nodes associated with the smoothing domain; for the boundary faces $N_{ns}=4$ whilst $N_{ns}=5$ for the interior faces. For instance, in Figure 8.1, associated nodes with the smoothing domains corresponding to the dashed faces are, respectively, nodes *A*, *B*, *C*, *D* for case (*a*) and *A*, *B*, *C*, *D*, *E* for case (*b*).

In addition, using the divergence theorem, the smoothed strain gradient matrix $\bar{\mathbf{B}}_I$ in the foregoing equation can be written in the following form

$$\bar{\mathbf{B}}_I = \frac{1}{V_k}\int_{\Omega_k^s} \nabla_s \mathbf{N}_I(\mathbf{x})d\Omega \tag{8.7}$$

Meaning that $\bar{\mathbf{B}}_I$ is calculated by performing the integration on the boundaries of smoothing domain (Γ_k^s), resulting in the following matrix form;

$$\bar{\mathbf{B}}_I(\mathbf{x}_k) = \frac{1}{V_k^s}\int_{\Gamma_k^s} \mathbf{n}_k^s(\mathbf{x})\mathbf{N}_I(\mathbf{x})d\Gamma = \begin{bmatrix} \bar{b}_{Ix}(\mathbf{x}_k) & 0 & 0 \\ 0 & \bar{b}_{Iy}(\mathbf{x}_k) & 0 \\ 0 & 0 & \bar{b}_{Iz}(\mathbf{x}_k) \\ \bar{b}_{Iy}(\mathbf{x}_k) & \bar{b}_{Ix}(\mathbf{x}_k) & 0 \\ 0 & \bar{b}_{Iz}(\mathbf{x}_k) & \bar{b}_{Iy}(\mathbf{x}_k) \\ \bar{b}_{Iz}(\mathbf{x}_k) & 0 & \bar{b}_{Ix}(\mathbf{x}_k) \end{bmatrix} \tag{8.8}$$

Where $\mathbf{n}_k^s$ is a matrix of outward normal vector on the boundary Γ_k^s as

$$\int_{\Omega_k^s} \Phi_k(\mathbf{x})d\Omega = 1 \tag{8.9}$$

In addition, $\bar{b}_{Ih}$ $(h=x,y,z)$ in equation (8.8) is calculated as

$$\bar{b}_{Ih} = \frac{1}{V_k^s}\int_{\Gamma_k^s} n_{kh}^s(\mathbf{x})N_I(\mathbf{x})d\Gamma \qquad ;(h=x,y,z) \tag{8.10}$$

Where $\bar{b}_{Ih}$ is numerically evaluated using the Gauss-Quadrature rule

$$\bar{b}_{Ih}(x_k) = \frac{1}{V_k^s} \sum_{i=1}^{M} \sum_{j=1}^{N_{GP}} N_I(x_{i,j}^{GP}) w_{i,j}^{GP} n_{ih}^k \quad ; (h = x, y, z) \tag{8.11}$$

In which M is the number of (area) boundary segments of Γ_k^s, $x_{i,j}^{GP}$ is the Gaussian point location on the i^{th} boundary segment, $w_{i,j}^{GP}$ is the Gaussian weight associated with the Gaussian point $x_{i,j}^{GP}$, N_{GP} is the number of Gaussian points on the i^{th} boundary segment, and n_{ih}^k is the h^{th} component of the unit outward vector on the i^{th} boundary segment.

Using the calculated smoothed strain gradient matrix $\bar{\mathbf{B}}$, the IJ^{th} entry of k^{th} smoothed stiffness matrix $\bar{\mathbf{K}}$ can be now calculated as

$$\bar{\mathbf{K}}_{IJ(k)} = \int_{\Omega_k^s} \bar{\mathbf{B}}_I^T \mathbf{D} \bar{\mathbf{B}}_J \, \mathrm{d}\Omega = \bar{\mathbf{B}}_I^T \mathbf{D} \bar{\mathbf{B}}_J V_k^s \tag{8.12}$$

The global stiffness of entire domain is then calculated by assembling the stiffness matrices of all the smoothing domains.

8.3 Idea of singular FS-FEM

As it was mentioned in the foregoing section, FS-FEM uses a strain smoothing technique to produce a softer model than that of FEM, yielding more accurate results than that of FEM. Most importantly, FS-FEM works very well with linear 4-noded tetrahedral elements and provides more accurate results than FEM. Unfortunately; standard form of FS-FEM does not exhibit the same remarkable features when it comes to the problems containing a discontinuity like crack. The reason is rooted in theoretically-singular

behavior of stress field along the crack front line which cannot be captured using the 4-noded tetrahedral elements with the linear interpolation functions.

In the following sections, the main focus is to develop a new type of FS-FEM for the crack problems by properly simulating theoretical behavior of stress field, and simultaneously, taking advantage of simple but unique properties of standard FS-FEM.

The new proposed method will be called “singular faced-based smoothed finite element method (singular FS-FEM) which, similar to the singular ES-FEM approach in 2D space, modifies the standard FS-FEM for the fracture simulation. Singular FS-FEM adopts a layer of specially designed singular 10-node prism elements located along the crack-tip nodes as shown in Figure 8.2. For the remaining parts of the domain, however, the standard 4-node tetrahedral elements are recommended due to their capability of being easily created even for the geometrically-complicated volumes.

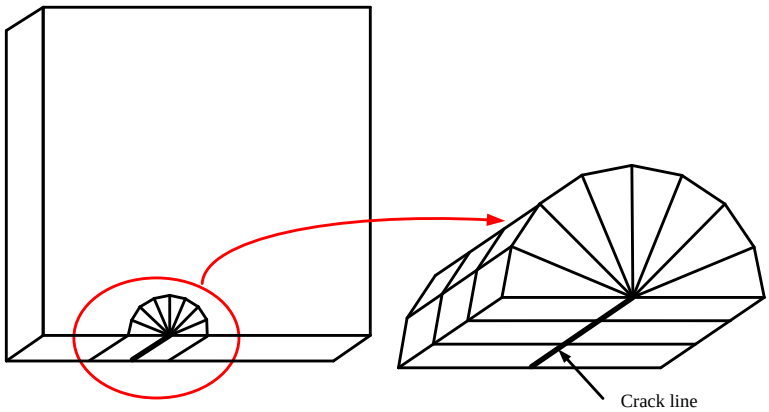

Figure 8.2. Some layers of prism elements along the crack line for a typical 3-D problem

Simultaneous use of tetrahedral and prism elements, however, causes an inconformity issue in the areas wherein rectangular faces of prism and triangular faces of tetrahedrons meet each other. As it can be seen in Figure 8.3(a), at least two tetrahedrons

are required to cover one rectangular face of the prism, meaning that each prism will have more than one adjacent element at the rectangular face meeting tetrahedron mesh. To resolve the issue, another type of element is proposed to be used. In this study pyramid element is adopted as the simplest choice to make a connection between two different types of elements without creating an inconformity issue. This is shown in Figure 8.3(b).

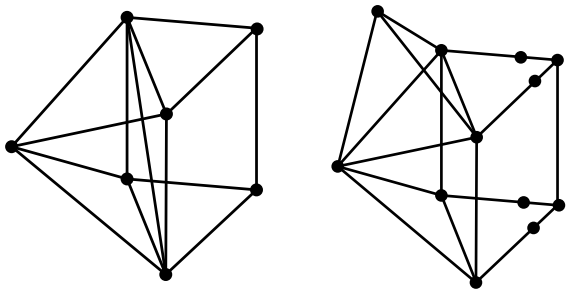

Figure 8.3. (a) Directly connecting prism element to tetrahedral elements (b) Using the pyramid element as a connector between quadrilateral surface of prism and triangular face of tetrahedron

Using the set of three different types of elements and applying the strain smoothing technique over the smoothing domains associated with elements faces, the method of singular FS-FEM is developed. In the following sections, different aspects of the method will be elaborated more.

8.4 Smoothing domain creation in singular FS-FEM

Following the similar strategy of standard FS-FEM for creation of smoothing domains associated with triangular faces of tetrahedral elements, the discretized model for the singular FS-FEM is created. However, due to introducing new additional element types, four more types of smoothing domains are constructed beyond those created in

standard FS-FEM. Based on the shape and neighboring elements, each face in singular FS-FEM model falls in one of the following categories:

- Triangular face belonging to two tetrahedral elements;

  This face is the typical face of standard FS-FEM with the smoothing domain construction approach previously described.

- Rectangular face between two neighboring prism elements;

  Creation of smoothing domain in this case is typically shown in Figure 8.4 for face *ABCD* as the common face between two prisms *ABCDEF* and *ABCDLK*. Edge *BC* in this figure is distinguished as the crack edge, and every other edge to which it directly connects is enriched with one additional node. The smoothed domain for this face is then created with faces ABG_1, ADH_1G_1, BCH_1G_1, DCH_1, ABG_2, ADH_2G_2, BCH_2G_2, and DCH_2, where H_1, G_1, *H2* and *G2* are the centroid of triangular faces.

- Rectangular face belonging to only one prism element on the free surface of crack;

  Creation of smoothing domain in this case is typically shown for face *BCEF* in Figure 8.5. The smoothing domain is constructed by faces *BCEF*, BCG_1H_1, EFG_1H_1, BFG_1, CEH_1.

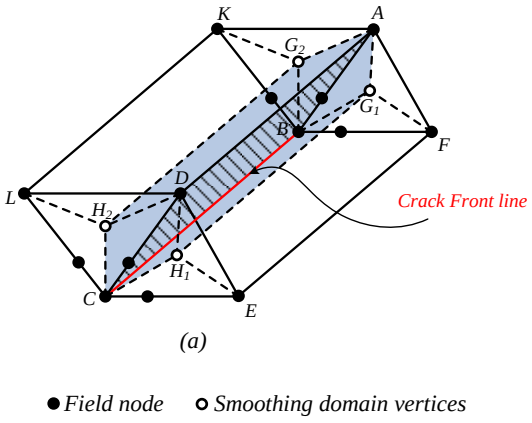

Figure 8.4. Smoothing domain associated with rectangular face between two neighbor prism elements

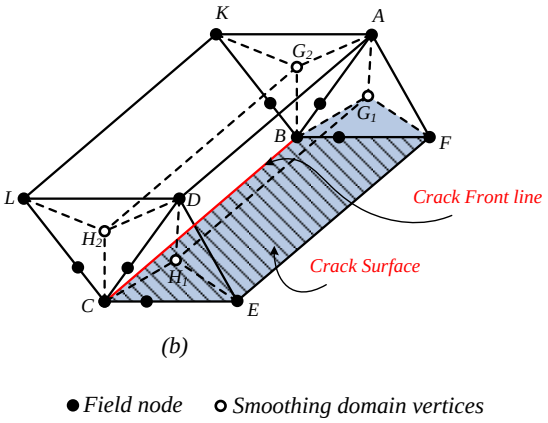

Figure 8.5. Smoothing domain associated with rectangular face belonging to only one prism element on the free surface of crack

- Rectangular face between one prism and one pyramid element;

  Creation of smoothing domain in this case is typically shown in Figure 8.6 for face *AKLD* as the common face between prism *ABCDLK* and pyramid element *ADLKM*. The smoothing domain is constructed with faces AKG_2, ADH_2G_2, KLH_2G_2, DLH_2, AKG_3, ADG_3, KLG_3 and DLG_3. It should be noted that G_3 is the center point of pyramid.

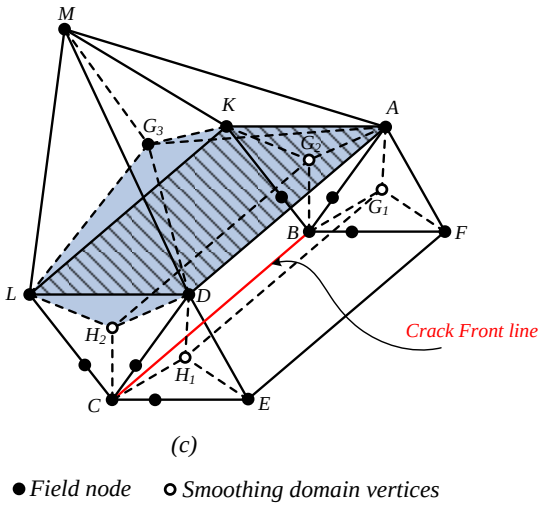

Figure 8.6. Smoothing domain associated with rectangular face between one prism and one pyramid element

- Triangular face between one tetrahedron and one pyramid element;

Creation of smoothing domain in this case is typically shown for face *MLD* in Figure 8.7. The smoothing domain is constructed with faces MDG_3, MLG_3, LDG_3, MDG_4, MLG_4 and LDG_4, where G_4 is the centroid of tetrahedron.

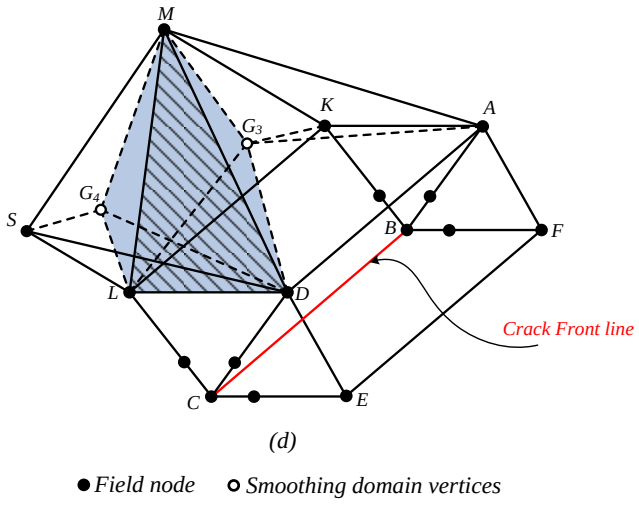

Figure 8.7. Smoothing domain associated with triangular face between one tetrahedron and one pyramid element

As it can be seen, in the prism element, smoothing domains are only created associated with rectangular faces (and not the triangular ones) by subsequently connecting the corner nodes of rectangular face to the centroid of triangular ones. Using this technique, every prism element contributes in three smoothing domains. For the pyramid elements, however, per each surface one smoothing domain is created (similar to tetrahedrons) by connecting the corner nodes of that face (could be rectangular or triangular face) to the centroid of the pyramid. This makes every pyramid element of the background mesh contribute in 5 smoothing domains.

8.5 Displacement interpolation within the prism element

The novel prism element for the crack problems with specially designed shape functions is exhibited in Figure 8.8. This specially designed element for properly simulation of singular behavior of stress field needs to be placed at the crack front along one of its longitude edges. In order to derive the shape functions for such element, two basic assumptions have been made:

- In the radial directions emanating from crack edge, displacement varies in the same way as in the previously introduced one dimensional crack tip elements (See, Figure 5.3) with the following interpolation fashion

$$u = c_0 + c_1 r + c_2 \sqrt{r} \qquad ;(c_0, c_1, c_2 \text{ are cosntants}) \tag{8.13}$$

  As it can be seen this function is linearly complete in r and owns some extra fractional term $\sqrt{r}$ to produce the singular term $1/\sqrt{r}$ in the strain field.

Referring to the strategy thoroughly described in chapter 5, the shape functions for such element is given by equation (5.8).

- In the tangential directions, displacement is assumed to vary linearly.

Considering edge 1-4 in Figure 8.8 as the crack front edge, any displacement component like component u along an arbitrary line $M-\delta''-\beta''$ is evaluated as:

$$u = u_M \phi_1 + u_{\delta''} \phi_2 + u_{\beta''} \phi_3 \tag{8.14}$$

In addition, by using simbole l_{i-j} as the distance between points i and j, displacement values of points M, δ'' and β'' can be written in terms of those values of element nodes as following equation.

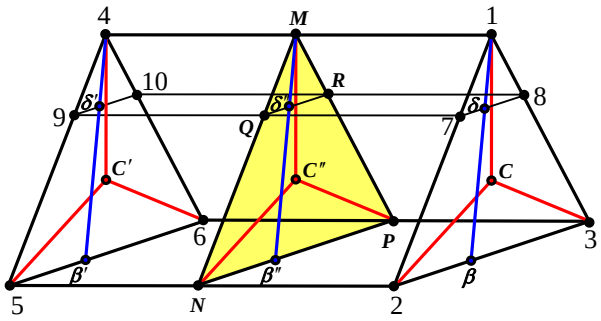

Figure 8.8. A prism element at the crack tip

$$\begin{aligned}
u_M &= \left(1-\frac{l_{M-1}}{l_{4-1}}\right)u_1 + \frac{l_{M-1}}{l_{4-1}}u_4 \\
u_{\delta''} &= \left(1-\frac{l_{\delta''-\delta}}{l_{\delta'-\delta}}\right)u_\delta + \frac{l_{\delta''-\delta}}{l_{\delta'-\delta}}u_{\delta'} \\
u_{\beta''} &= \left(1-\frac{l_{\beta''-\beta}}{l_{\beta'-\beta}}\right)u_\beta + \frac{l_{\beta''-\beta}}{l_{\beta'-\beta}}u_{\beta'}
\end{aligned} \tag{8.15}$$

in which u_δ, $u_{\delta'}$, u_β and $u_{\beta'}$ are, themselves, linear variations of nodal values as

$$\begin{cases} u_\delta = \left(1-\dfrac{l_{7-\delta}}{l_{7-8}}\right)u_7 + \dfrac{l_{7-\delta}}{l_{7-8}}u_8 \\ u_\beta = \left(1-\dfrac{l_{2-\beta}}{l_{2-3}}\right)u_2 + \dfrac{l_{2-\beta}}{l_{2-3}}u_3 \end{cases} \quad \& \quad \begin{cases} u_{\delta'} = \left(1-\dfrac{l_{9-\delta'}}{l_{9-10}}\right)u_9 + \dfrac{l_{9-\delta'}}{l_{9-10}}u_{10} \\ u_{\beta'} = \left(1-\dfrac{l_{5-\beta}{}'}{l_{5-6}}\right)u_5 + \dfrac{l_{5-\beta}{}'}{l_{5-6}}u_6 \end{cases} \tag{8.16}$$

After making relations (8.15) and (8.16) more simplified by using the simple fact that $\dfrac{l_{M-1}}{l_{4-1}} = \dfrac{l_{\delta''-\delta}}{l_{\delta'-\delta}} = \dfrac{l_{\beta''-\beta}}{l_{\beta'-\beta}} = \eta$ and $\dfrac{l_{7-\delta}}{l_{7-8}} = \dfrac{l_{2-\beta}}{l_{2-3}} = \dfrac{l_{9-\delta'}}{l_{9-10}} = \dfrac{l_{5-\beta}{}'}{l_{5-6}} = \alpha$, they can be substituted into (8.14) to give the following equation as the corresponding function to the variation of displacement component for any arbitrary point inside the prism element.

$$\begin{aligned} u = &\left\{(1-\eta)u_1 + \eta u_4\right\}\phi_1 + \\ &\left\{(1-\eta)\left((1-\alpha)u_7 + \alpha u_8\right) + \eta\left((1-\alpha)u_9 + \alpha u_{10}\right)\right\}\phi_2 + \\ &\left\{(1-\eta)\left((1-\alpha)u_2 + \alpha u_3\right) + \eta\left((1-\alpha)u_5 + \alpha u_6\right)\right\}\phi_3 \end{aligned} \tag{8.17}$$

Or in terms of nodal displacement values as

$$\begin{aligned} u = &\underbrace{\left\{(1-\eta)\phi_1\right\}}_{N_1}u_1 + \underbrace{\left\{(1-\eta)(1-\alpha)\phi_3\right\}}_{N_2}u_2 + \underbrace{\left\{(1-\eta)\alpha\phi_3\right\}}_{N_3}u_3 + \underbrace{\left\{\eta\phi_1\right\}}_{N_4}u_4 + \\ &\underbrace{\left\{\eta(1-\alpha)\phi_3\right\}}_{N_5}u_5 + \underbrace{\left\{\eta\alpha\phi_3\right\}}_{N_6}u_6 + \underbrace{\left\{(1-\eta)(1-\alpha)\phi_2\right\}}_{N_7}u_7 + \\ &\underbrace{\left\{(1-\eta)\alpha\phi_2\right\}}_{N_8}u_8 + \underbrace{\left\{\eta(1-\alpha)\phi_2\right\}}_{N_9}u_9 + \underbrace{\left\{\eta\alpha\phi_2\right\}}_{N_{10}}u_{10} \end{aligned} \tag{8.18}$$

That can be re-written in the following matrix form

$$u = \mathbf{Nd} \tag{8.19}$$

with

$$\mathbf{d} = \begin{bmatrix} u_1 & u_2 & u_3 & u_4 & u_5 & u_6 & u_7 & u_8 & u_9 & u_{10} \end{bmatrix}^T \quad ,and$$
$$\mathbf{N} = \begin{bmatrix} N_1 & N_2 & N_3 & N_4 & N_5 & N_6 & N_7 & N_8 & N_9 & N_{10} \end{bmatrix} \tag{8.20}$$

In which the nodal shape functions are defined as equation (8.21). Because in our singular ES-FEM, we do not need derivatives of shape functions, this equation is all we need in computing the stiffness matrix for creating our numerical model.

$$\begin{aligned} N_1 &= (1-\eta)\phi_1 & N_2 &= (1-\eta)(1-\alpha)\phi_3 \\ N_3 &= (1-\eta)\alpha\phi_3 & N_4 &= \eta\phi_1 \\ N_5 &= \eta(1-\alpha)\phi_3 & N_6 &= \eta\alpha\phi_3 \\ N_7 &= (1-\eta)(1-\alpha)\phi_2 & N_8 &= (1-\eta)\alpha\phi_2 \\ N_9 &= \eta(1-\alpha)\phi_2 & N_{10} &= \eta\alpha\phi_2 \end{aligned} \tag{8.21}$$

8.6 Displacement interpolation for a pyramid element in FS-FEM

As it was mentioned before, the pyramid elements are divided into five strain smoothing domains associated with faces, through the similar strategy of smoothing domain creation for the triangular faces of tetrahedral elements. The numerical integrations are then computed on the surfaces bounding these domains to calculate the stiffness matrix. In the singular FS-FEM, A natural pyramid element with the corresponding natural coordinate system shown in Figure 8.9 and shape functions given in equation (8.22) is used.

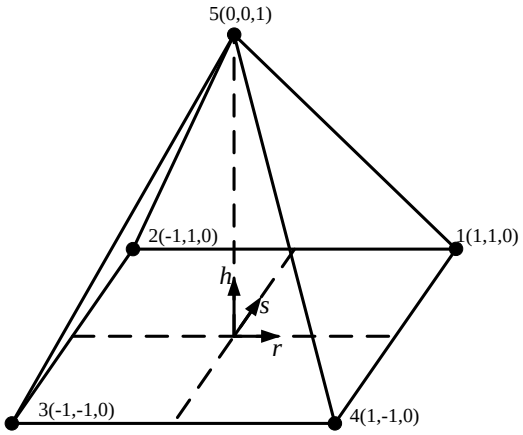

Figure 8.9. The pyramid element in the natural coordinate

The shape functions for such element have been proposed by Bedrosian [65] as:

$$H_1 = \frac{1}{4}\left((1+r)(1+s) - h + \frac{(rsh)}{(1-h)}\right), \quad H_2 = \frac{1}{4}\left((1-r)(1+s) - h - \frac{(rsh)}{(1-h)}\right)$$

$$H_3 = \frac{1}{4}\left((1-r)(1-s) - h + \frac{(rsh)}{(1-h)}\right), \quad H_4 = \frac{1}{4}\left((1+r)(1-s) - h - \frac{(rsh)}{(1-h)}\right) \qquad (8.22)$$

$$H_5 = h$$

Since in singular FS-FEM, integrations are calculated over the surrounding faces of each smoothing domains, the integration points and weighting coefficients of the Gauss-Legendre quadrature for triangular surfaces can be adopted here. The location of Gaussian points on the faces can be then identified using a simple mapping approach between the coordinate system of natural triangle and the one in the new setting of smoothing domains which is shown with red color in Figure 8.10.

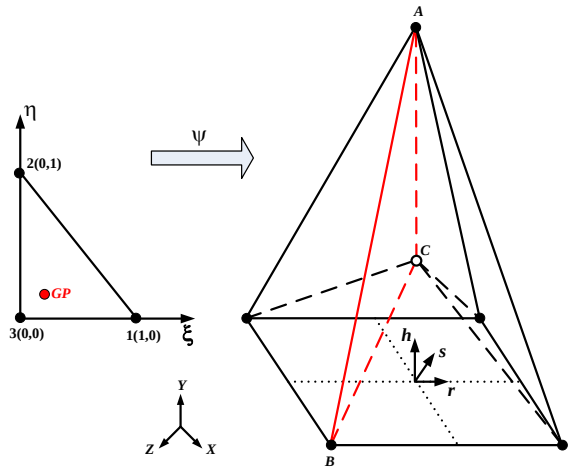

Figure 8.10. Mapping between triangle natural coordinate system and new coordinate system in the smoothing domain setting

As it is shown in this figure a direct mapping function ψ can be defined to directly map a typical point (ξ,η) on the reference triangle to a unique point on a triangle inside the pyramid (e.g., triangle *ABC*). Assume that points (1,0), (0,1) and (0,0) in the reference coordinate are respectively mapped on the points *A*, *B* and *C* in the second coordinate. Writing $\boldsymbol{\chi}$ for (ξ,η) and $\mathbf{R}$ for (r,s,h), the mapping function can be formulated in the following simple form:

$$\psi(\boldsymbol{\chi}) = \boldsymbol{\Omega}.\boldsymbol{\chi} + \mathbf{C} = \mathbf{R} \tag{8.23}$$

In order to use the above transition, the function matrix $\boldsymbol{\Omega}$ should be identified. The following mathematical efforts will lead to finding the components of matrix $\boldsymbol{\Omega}$.

$$\psi(1,0) = \begin{bmatrix} \Omega_{11} & \Omega_{12} \\ \Omega_{21} & \Omega_{22} \\ \Omega_{31} & \Omega_{32} \end{bmatrix} . \begin{Bmatrix} 1 \\ 0 \end{Bmatrix} + \begin{Bmatrix} C_r \\ C_s \\ C_h \end{Bmatrix} = \begin{Bmatrix} A_r \\ A_s \\ A_h \end{Bmatrix} \tag{8.24}$$

Therefore,

$$\begin{cases} \Omega_{11} = A_r - C_r \\ \Omega_{21} = A_s - C_s \\ \Omega_{31} = A_h - C_h \end{cases} \tag{8.25}$$

Similarly,

$$\psi(0,1) = \begin{bmatrix} \Omega_{11} & \Omega_{12} \\ \Omega_{21} & \Omega_{22} \\ \Omega_{31} & \Omega_{32} \end{bmatrix} . \begin{Bmatrix} 0 \\ 1 \end{Bmatrix} + \begin{Bmatrix} C_r \\ C_s \\ C_h \end{Bmatrix} = \begin{Bmatrix} B_r \\ B_s \\ B_h \end{Bmatrix} \tag{8.26}$$

This results in:

$$\begin{cases} \Omega_{12} = B_r - C_r \\ \Omega_{22} = B_s - C_s \\ \Omega_{32} = B_h - C_h \end{cases} \tag{8.27}$$

Hence, the mapping function can be written as the following form:

$$\psi(\xi,\eta) = \begin{bmatrix} A_r - C_r & B_r - C_r \\ A_s - C_s & B_s - C_s \\ A_h - C_h & B_h - C_h \end{bmatrix} . \begin{Bmatrix} \xi \\ \eta \end{Bmatrix} + \begin{Bmatrix} C_r \\ C_s \\ C_h \end{Bmatrix} = \begin{Bmatrix} r \\ s \\ h \end{Bmatrix} \tag{8.28}$$

One might also think about finding the location of Gaussian points in the Cartesian coordinate first and then in the natural coordinate of the pyramid as follows:

$$\begin{cases} X_{GP} = \sum_{i=1}^{3} \varphi_i(\xi,\eta) X_i \\ Y_{GP} = \sum_{i=1}^{3} \varphi_i(\xi,\eta) Y_i \\ Z_{GP} = \sum_{i=1}^{3} \varphi_i(\xi,\eta) Z_i \end{cases} \tag{8.29}$$

Wherein $\varphi_i(\xi,\eta)$ represents the i^{th} shape function of the triangle in its natural coordinate system and (X_i, Y_i, Z_i) are the Cartesian coordinates of the triangle nodes.

Similarly, one can describe the position of the Gaussian point in the framework of the pyramid as:

$$\begin{cases} X_{GP} = \sum_{j=1}^{5} H_j(r,h,s) X_j \\ Y_{GP} = \sum_{j=1}^{5} H_j(r,h,s) Y_j \\ Z_{GP} = \sum_{j=1}^{5} H_j(r,h,s) Z_j \end{cases} \tag{8.30}$$

Wherein $H_j(r,h,s)$ represents the j^{th} shape function of the triangle in its natural coordinate system and $\left(X_j, Y_j, Z_j\right)$ are the Cartesian coordinates of the pyramid nodes. Therefore, by substituting the Cartesian coordinates of the Gaussian point from (8.29) into (8.30), one may find a system of nonlinear simultaneous equations in terms of (r,h,s). Regarding the fact that finding a unique solution for this system of nonlinear equations is not easy, the simpler method of direct mapping between two triangles is adopted in this study.

8.7 J-integral and stress intensity factors

Using the singular FS-FEM to analyze the problem, the displacements, strains and stresses can be evaluated. Using these outputs, J-integral parameter can be also computed. The stress intensity factors, however, are still unknown. Although, some models have been proposed to calculate stress intensity factors based on the displacement values around the crack tip, these methods suffers from the lack of accuracy. Yet, the energy method seems to be the best choice. On the other hand the successful interaction integral has provided the possibility of using an energy-based method and extracting the

stress intensity factor values from the evaluated J-integral. The process is explained in the following sections.

8.7.1 Calculation of J-integral and Stress intensity factor

According to the definition of *J*-integral at point *s* along a 3-D crack front shown in Figure 8.11 [112];

$$J(s) = \lim_{\Gamma_J \to 0} \int_{\Gamma_J} (w\delta_{1i} - \sigma_{ij} \frac{\partial u_j}{\partial x_1}) n_i d\Gamma \tag{8.31}$$

Where Γ_J is a closed boundary contour that encloses the crack front point *s* and lies in the *X1-X2* plane of the local coordinate system. Besides, in equation (8.31), n_i represents the components of outward normal vectors on Γ_J.

Equivalent volume form of equation (8.31) proposed by shih et al. [112] seems much easier to work with for a numerical evaluation in a 3-D FEM framework. To this end, a volume is created associated with point *s* by extending contour Γ_J over a length L_c of crack front as shown in the figure. As it can be seen, the volume *V* is enclosed with the lateral surfaces S_2 and S_3, cylindrical surfaces S_t and S_1, and top and bottom crack-face surfaces S^+ and S^-.

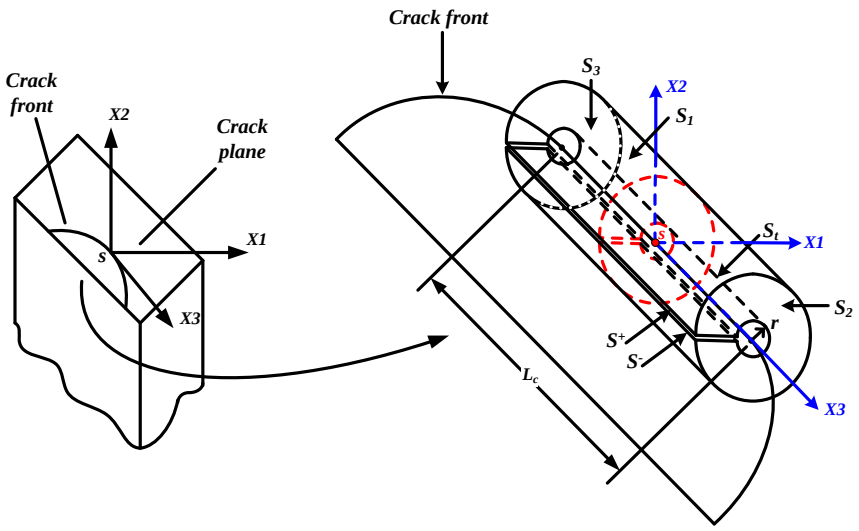

Figure 8.11. A typical 3-D crack front and corresponding domain for J-integral calculation

The energy released per unit advance of crack front segment L_c is then calculated as

$$\overline{J}(s)=\int_V\left(\sigma_{ij}u_{j,1}-W\delta_{1i}\right)q_{,i}dV+\int_V\left(\sigma_{ij}u_{j,1}-W\delta_{1i}\right)_{,i}qdV-\int_{S^+S^-}t_ju_{j,1}qdS \qquad (8.32)$$

Where q is a smoothing function. The relation between J value at point s and $\overline{J}(s)$ is also given by

$$J(s)=\frac{\overline{J}(s)}{\int_{L_c}q(s)ds} \qquad (8.33)$$

Figure 8.12 also shows a suitable cylindrical path for a typical point s located on a straight crack front. For the axisymmetric problems like a circular penny shape crack at the middle of a cylindrical shaped solid of which a portion is shown in Figure 8.13 , one can also write

$$\int_{L_c}q(s)ds=\int_{L_c}q(s)Rd\phi \qquad (8.34)$$

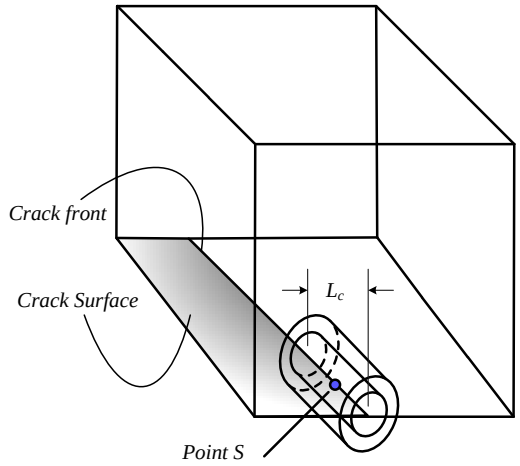

Figure 8.12. A typical straight crack front in 3-D and corresponding domain for J-integral calculation

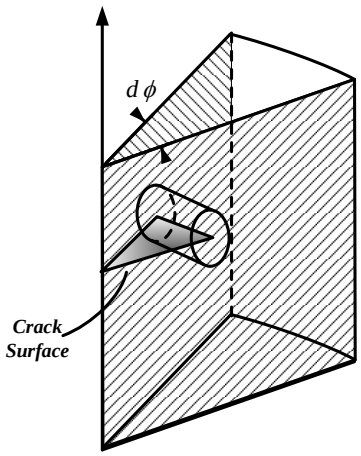

Figure 8.13. A portion of a typical axisymmetric problem

8.7.2 Volume form of interaction integral for planar crack surfaces

In order to extract the values of stress intensity factors from *J*-integral parameter, the volume form of interaction integral method is implemented. When the crack surfaces are planar, the domain form of the averaged Interaction integral can be written using the following equation [113, 114];

$$\bar{I}(s)=\int_V \underbrace{\left(\sigma_{ij}u_{j,1}^{(aux)}+\sigma_{ij}^{(aux)}u_{j,1}-\sigma_{jk}\varepsilon_{jk}^{(aux)}\delta_{1j}\right)q_{,i}}_{tr(\mathbf{P}.\nabla\mathbf{q})}dV+ \int_V \underbrace{\left[\sigma_{ij}\left(u_{j,1i}^{(aux)}-\varepsilon_{ij,1}^{(aux)}\right)+\sigma_{ij,1}^{(aux)}u_{j,1}\right]q}_{(\nabla.\mathbf{P}^T).\mathbf{q}}dV-\int_V t_j u_{j,1}^{(aux)}qdS \tag{8.35}$$

Although the second integral of the above equation will vanish for the straight crack fronts, it does not equal to zero for the cracks with the curved front. This is because of employing the curvilinear coordinate system for the curved crack front. In this case $\boldsymbol{\varepsilon}^{(aux)}\neq\nabla_s\mathbf{u}^{(aux)}$ and as a result

$$(\nabla.\mathbf{P}^T)=\boldsymbol{\sigma}:(\boldsymbol{\varepsilon}^{(aux)}\nabla-\nabla\mathbf{u}^{(aux)}\nabla)-(\nabla\mathbf{u}).(\nabla.\boldsymbol{\sigma}^{(aux)})\neq 0 \tag{8.36}$$

A strategy for skipping the difficulty of calculating second integral was proposed by Dodds [113] as "not using the curvilinear coordinate system instead of the Cartesian one". In such case one can simply avoid to evaluate the second integral even for the crack curved fronts. It should be noticed that the last term in the right hand side of the equation will be also vanished in the absence of traction on the crack surfaces. Furthermore, this equation works only for the planar crack surfaces and for the non-planar ones another additional terms should be evaluated as discussed in a work by Gosz [112] for the non-planar cracks. $I(s)$ can then be calculated as:

$$I(s)=\frac{\bar{I}(s)}{\int_{L_c} q(s)ds} \tag{8.37}$$

According to Williams' solution [115] for the stresses and displacements at the vicinity of crack fronts, $\sigma_{ij}^{(aux)}$, $u_i^{(aux)}$ and $\varepsilon_{ij}^{(aux)}$ (i,j=1,2,3) is described as

$$\sigma_{ij}^{(aux)} = \frac{K_I^{(aux)}}{\sqrt{2\pi r}} f_{ij}^{I}(\theta) + \frac{K_{II}^{(aux)}}{\sqrt{2\pi r}} f_{ij}^{II}(\theta) + \frac{K_{III}^{(aux)}}{\sqrt{2\pi r}} f_{ij}^{III}(\theta)$$

$$u_j^{(aux)} = \frac{K_I^{(aux)}}{2\mu}\sqrt{\frac{r}{2\pi}}\, g_{ij}^{I}(\theta,\nu) + \frac{K_{II}^{(aux)}}{2\mu}\sqrt{\frac{r}{2\pi}}\, g_{ij}^{II}(\theta,\nu) + \frac{2K_{III}^{(aux)}}{\mu}\sqrt{\frac{r}{2\pi}}\, g_{ij}^{III}(\theta,\nu) \quad (8.38)$$

$$\varepsilon_{ij}^{(aux)} = \frac{1}{2}\left(u_{i,j}^{(aux)} + u_{j,i}^{(aux)}\right)$$

Resulting in the following forms for the stress and displacement components [113, 114].

$$\sigma_{11}^{(aux)} = \frac{1}{\sqrt{2\pi r}}\left\{K_I^{(aux)}\cos\frac{\theta}{2}\left(1-\sin\frac{\theta}{2}\sin\frac{3\theta}{2}\right) - K_{II}^{(aux)}\sin\frac{\theta}{2}\left(2+\cos\frac{\theta}{2}\cos\frac{3\theta}{2}\right)\right\} \quad (8.39)$$

$$\sigma_{22}^{(aux)} = \frac{1}{\sqrt{2\pi r}}\left\{K_I^{(aux)}\cos\frac{\theta}{2}\left(1+\sin\frac{\theta}{2}\sin\frac{3\theta}{2}\right) + K_{II}^{(aux)}\cos\frac{\theta}{2}\sin\frac{\theta}{2}\cos\frac{3\theta}{2}\right\} \quad (8.40)$$

$$\sigma_{12}^{(aux)} = \frac{1}{\sqrt{2\pi r}}\left\{K_I^{(aux)}\cos\frac{\theta}{2}\sin\frac{\theta}{2}\cos\frac{3\theta}{2} + K_{II}^{(aux)}\cos\frac{\theta}{2}\left(1-\sin\frac{\theta}{2}\sin\frac{3\theta}{2}\right)\right\} \quad (8.41)$$

$$\sigma_{23}^{(aux)} = \frac{1}{\sqrt{2\pi r}} K_{III}^{(aux)}\cos\frac{\theta}{2} \quad (8.42)$$

$$\sigma_{13}^{(aux)} = \frac{-1}{\sqrt{2\pi r}} K_{III}^{(aux)}\sin\frac{\theta}{2} \quad (8.43)$$

$$\sigma_{33}^{(aux)} = \begin{cases} \nu(\sigma_{11}^{(aux)} + \sigma_{22}^{(aux)}) & \textit{plane strain} \\ 0 & \textit{plane stress} \end{cases} \quad (8.44)$$

$$u_1^{(aux)} = \frac{1}{8\mu}\sqrt{\frac{2r}{\pi}}\left\{K_I^{(aux)}\left[(5-8\nu)\cos\frac{\theta}{2} - \cos\frac{3\theta}{2}\right] + K_{II}^{(aux)}\left[(9-8\nu)\sin\frac{\theta}{2} + \sin\frac{3\theta}{2}\right]\right\} \quad (8.45)$$

$$u_2^{(aux)} = \frac{1}{8\mu}\sqrt{\frac{2r}{\pi}}\left\{K_I^{(aux)}\left[(7-8\nu)\sin\frac{\theta}{2} - \sin\frac{3\theta}{2}\right) - K_{II}^{(aux)}\left[(3-8\nu)\cos\frac{\theta}{2} + \cos\frac{3\theta}{2}\right)\right\} \quad (8.46)$$

$$u_3^{(aux)} = \frac{1}{\mu}\sqrt{\frac{2r}{\pi}} K_{III}^{(aux)}\sin\frac{\theta}{2} \quad (8.47)$$

Where r and θ are measured from the origin of coordinate system located at the crack tip node and

$$\kappa = \begin{cases} 3-4\nu & \textit{plane strain} \\ \dfrac{3-\nu}{1+\nu} & \textit{plane stress} \end{cases} \tag{8.48}$$

8.8 Calculation of r and θ at the integration points

Using a number of elements to discretize the problem domain, each integral term of equation (8.35) is numerically calculated. To this end, values of r and θ corresponding to each Gaussian point should be known. For a typical crack front with the local coordinate system shown in Figure 8.13, distance r between the Gaussian point and its nearest element edge lying along the crack front, and relevant angle θ is identified based on a simple algorithm which is schematically shown in the figure as well.

First, projection of Gaussian point *G* on crack front plane (plane *X1-X3* in the figure) is determined (Let name it, point *H*). Next, point *H* is projected on the nearest element edge along the crack front (Let say, edge A*B*) to obtain point *D*. point *D* is then connected to the initial Gaussian point *G* using a straight line to create the $\vec{\mathbf{r}}$ vector with the norm r and angle θ with the crack plane. Since, in vector space, the magnitude of cross product of two vectors can be interpreted as the positive area of parallelogram built up on those vectors, one can mathematically express the distance r as

$$r = \frac{\left\| AB \times AG \right\|}{\left\| AB \right\|} \tag{8.49}$$

Based on the position of point *G* regarding crack plane as well as crack front (which can be above or below the crack plane, or ahead or behind the crack front), four possible regions are identified as shown in Figure 8.13. If the second component of *G*'s local coordinate is positive ($X_2^G > 0$) then the point is placed above the crack plane, either in region *I* or *II*. On the other hand, if the sign of $AB \times AH$ is greater than zero, the point is located ahead of crack front, either in region *I* or *IV*. The angle θ is then expressed for four different regions as

$$\begin{aligned} &\theta = \sin^{-1}\left(\frac{X_2^G}{r}\right) \quad ; Region\, I \quad , \quad \theta = \pi - \sin^{-1}\left(\frac{X_2^G}{r}\right) \; ; Region\, II \\ &\theta = -\pi - \sin^{-1}\left(\frac{X_2^G}{r}\right) \; ; Region\, III \quad , \quad \theta = \sin^{-1}\left(\frac{X_2^G}{r}\right) \quad ; Region\, IV \end{aligned} \tag{8.50}$$

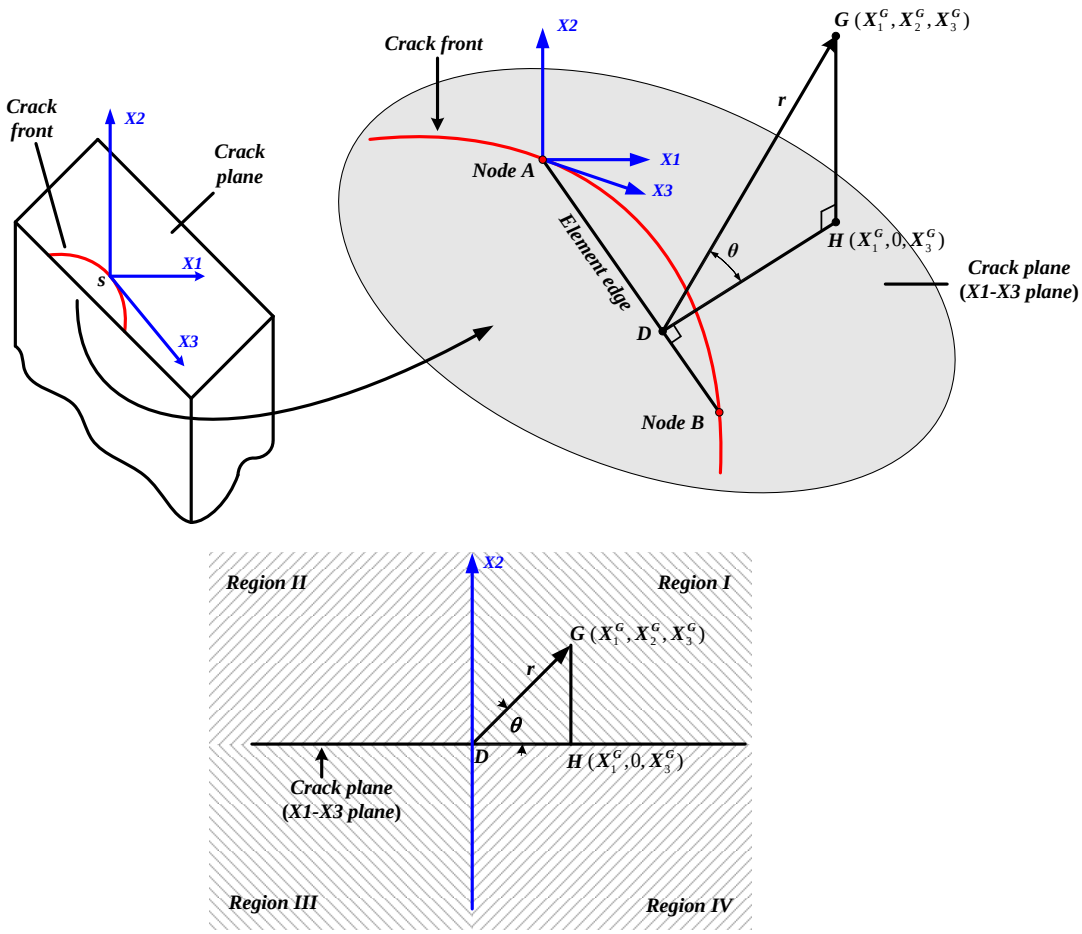

Figure 8.14. Identifying values of r and θ at each Gaussian point

8.9 Numerical calculation of q for singular FS-FEM

Because the FS-FEM uses a base mesh of linear 4-node tetrahedral elements, a simple scheme can be devised to determine the area-path V_J shown in Figure 8.15. First, a set of elements having at least one node within a cylindrical volume of radius r_d around the crack line is found, and is denoted as N_d. The weighting function q used in the Volume-path interaction integral is then chosen as a piecewisely linear function passing through the nodal values at all the nodes belonging to all the elements in N_d. If a node n_i

belonging to an element $e \in N_d$ lies outside the circle, then the nodal value of the weighting function is set to zero: $q_i = 0$; if a node n_i lies inside the cylinder, however, the weighting function is then set to unit: $q_i = 1$.

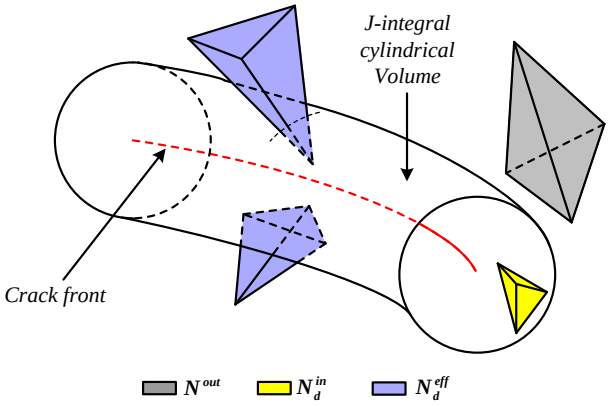

Figure 8.15. A typical method to select elements around the crack front to form the volume-path for the calculation of the interaction integral

Since the elements set N_d^{in} has all the nodes inside the cylinder as shown in the figure, their weight function will be a constant (unit) value, and they will contribute nothing to the interaction integral. This is due to the fact that gradient of q would be zero for a constant distributed field of nodal q for the element set N_d^{in}. A similar postulation is made for the element set N^{out} located outside the cylindrical volume. The non-zero contribution to the integral is obtained only for the element set N_d^{eff} with edges intersecting the cylinder. Because 4-node elements are used in ES-FEM, any cylinder will naturally always select a layer of elements that form V_J.

8.10 Numerical examples

In this section, performance of singular FS-FEM for both cases of straight and curved crack fornts is examined in details. The problems are solved using the proposed singular FS-FEM as well as singular FEM. In the singular FEM a mesh of 20-node and collapsed 20-node solid elements is used. The results in terms of strain energy, displacement and stress intensity factors are obtained using both methods. Furthermore, the path independency of the SIF results is investigated through different volumes chosen for the interaction integral method.

8.10.1 Homogenous finite cubical solid with a face crack

A cubical finite solid with a crack in one face was studied as a bench mark to examine the performance of singular FS-FEM in dealing with 3-D crack problems. The body is under tension stress at both edges. However, due to the symmetry in load and geometry, only half of the solid is modeled, as shown in Figure 8.16.

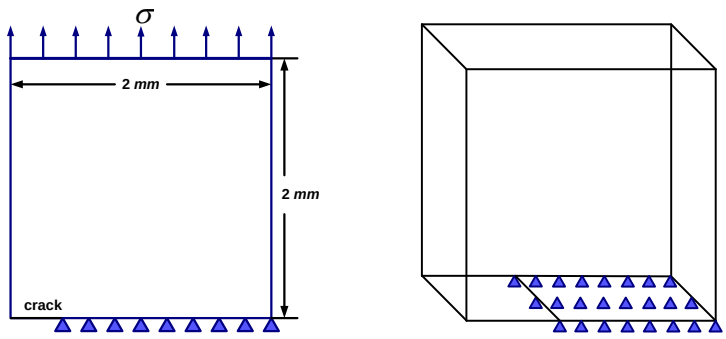

Figure 8.16. Homogenous finite cubical solid with a face crack

The problem has been solved using the singular FS-FEM and the results in terms of strain energy, displacement and stress intensity factors were obtained. First, a study

conducted to investigate the optimum number of Gaussian points (*GP*s) ensuring the stability of computational results. The findings of strain energy obtained at different meshes and by choosing five different sets of Gaussian points at different area types have been tabulated in Table 8.1. A comparison between the results corresponding to case (2) and (4) shows that, for the rectangular faces, increasing the number of *GP*s from 9 to 16 does not impose a considerable amount of change in the results. Similarly, comparing the results of cases (1) and (5), or cases (2) and (3) indicates that the results keep nearly constant when more than 3 *GP*s are used at triangular areas of the smoothing domains associated with the elements faces. Therefore, case (2) as set of 9 and 3 *GP*s at, respectively, rectangular and triangular areas is recommended to be adopted for the numerical integrations of present singular FS-FEM.

Table 8.1. Strain energy calculated by singular FSFEM and different sets of Gaussian points

DOF	726	864	942	1059	1215
Singular FS-FEM (1)	4.49431755442 2599e-008	4.82422671174 1371e-008	4.94693769993 6874e-008	4.99796247983 6373e-008	5.01797948222 3033e-008
Singular FS-FEM (2)	4.49896188909 9087e-008	4.82735503184 5988e-008	4.94866810684 3756e-008	4.99880571525 8969e-008	5.01835419181 5782e-008
Singular FS-FEM (3)	4.49894320521 5413e-008	4.82734239975 1259e-008	4.94865168005 9800e-008	4.99879683239 1507e-008	5.01834957001 4202e-008
Singular FS-FEM (4)	4.49894267117 41371e-008	4.82734175544 22599e-008	4.94865057152 58969e-008	4.99879486681 06843e-008	5.01834682410 97752e-008
Singular FS-FEM (5)	4.49429926031 7620e-008	4.82421390002 8739e-008	4.94692161535 6938e-008	4.99795398780 3813e-008	5.01797555123 3350e-008

The arrangement of the Gaussian points for the rectangular and triangular surfaces belong to the smoothing domains associated with the pyramid and prism elements:

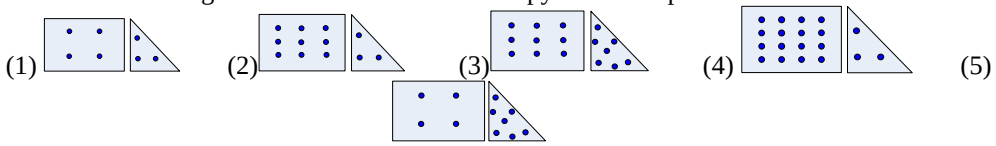

In order to make a comparison between performances of singular FS-FEM and singular FEM, the problem was also solved with FEM using the enriched elements along the crack front line, and the results in terms of strain energy and displacement have been illustrated in Figure 8.17 and tabulated in Table 8.2 and Table 8.3. Based on the analyses outcomes it can be observed that singular FS-FEM presents the more accurate results in terms of strain energy and displacement than standard singular FEM.

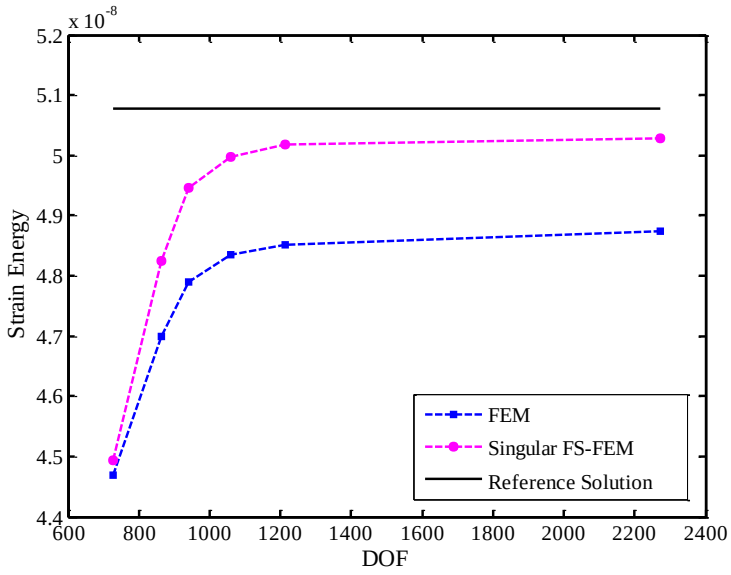

Figure 8.17. Strain energy obtained from singular FS-FEM and FEM with the singular elements along the crack front

Table 8.2. Comparison of Strain energy calculated by singular FSFEM and Singular FEM

DOF	726	864	942	1059	1215	2280
Singular FEM	4.46912243e-008	4.69919918e-008	4.79007665e-008	4.83453496e-008	4.85130166e-008	4.87344031e-008
Singular FS-FEM	4.494317554422599e-008	4.824226711741371e-008	4.946937699936874e-008	4.997962479836373e-008	5.017979482223033e-008	5.018601200713675e-008
	Reference Solution (Singular FEM With 26125node)			5.07757825e-008		

Table 8.3. Displacement component in the y direction

DOF	726	864	942	1059	1215	2280
Singular FEM	0.13526E-06	0.15167E-06	0.15757E-06	0.16046E-06	0.16150E-06	0.16321E-06
Singular FS-FEM	1.4066367 26645794e -007	1.6159809 24035188e -007	1.6833253 18460817e -007	1.7078958 77211193e -007	1.7171106 82274230e -007	1.7186017 62097757e -007
	Reference Solution (Singular FEM With 26125node)			0.17205E-06		

Moreover, the volume form of interaction integral has been adopted to evaluate the stress intensity factors at different points along the crack front line when the domain is discretized using a mesh containing a layer of prism elements along the crack line connected to the mesh of linear tetrahedral elements with a few pyramid elements in between.

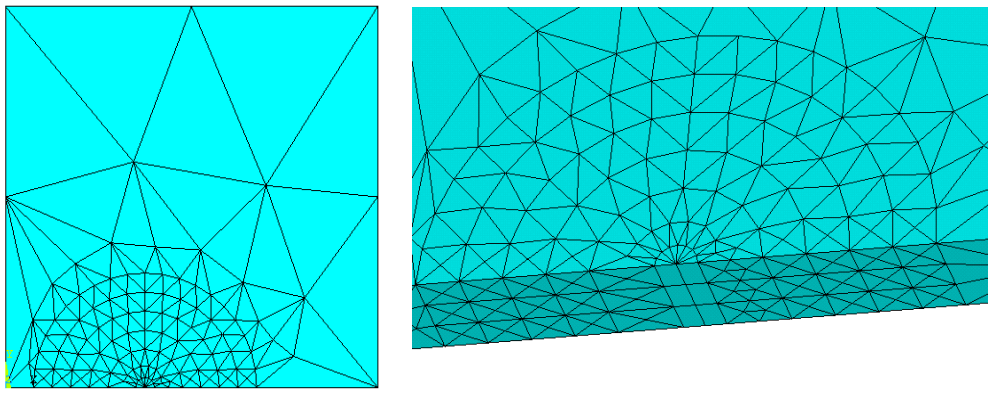

Figure 8.18. Typical mesh used in singular FS-FEM

In the development of singular FS-FEM it was sought to enhance the method in a way that it successfully simulates the problem by using a coarse base mesh of tetrahedral elements. Using such a coarse mesh will increase the computational efficiency and decrease the relevant costs.

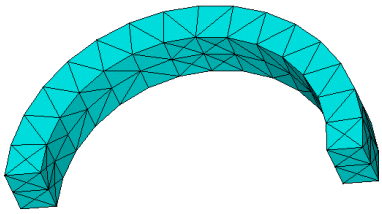

Figure 8.19. Typical volume chosen for the interaction integral calculation of singular FS-FEM

Furthermore, in order to provide the more smooth results of stress intensity factors for different domains chosen around the crack front, several layers of cylindrical volumes are created around the crack front to be used in the evaluation of interaction integral calculation of singular FS-FEM. Such a typical cylindrical volume is depicted in Figure 8.19 .

Based on the numerical results tabulated in Table 8.4; it can be highlighted that the method works very well with the interaction integral and provides stable results for different domains chosen around the crack front line. The results are accurate and path-independent.

The parameter r in this table is the radius of cylindrical volume chosen for the interaction integral evaluation and t is the thickness of specimen.

Based on these results, a symmetrical behavior can be highlighted for the values of stress intensity factors through the thickness; meaning that at $z=0$ and $z=t$ results are very close together, similarly at $z=t/4$ and $z=3t/4$. Besides, regardless of the volume chosen for the calculation of interaction integral, stress intensity parameter takes the maximum value at $z=0$ and $z=t$ (wherein the pure plane stress state exists) and

slightly decrease by approaching the mid plane of the specimen ($z = t/2$; wherein the stress state is no longer pure plane stress).

Table 8.4. Stress intensity factors calculated on different domains

Location	Method	$z = 0$ (error %)	$z = t/4$ (error %)	$z = t/2$ (error %)	$z = 3t/4$ (error %)	$z = t$ (error %)
$r = 0.35$	Sing ES-FEM	2.6475 (0.2700 %)	2.6247 (0.2400 %)	2.4226 (0.3100 %)	2.6248 (0.2300 %)	2.6471 (0.3100 %)
	Sing FEM	2.6421 (0.8100 %)	2.6211 (0.6000 %)	2.4189 (0.6800 %)	2.6213 (0.5800 %)	2.6423 (0.7900 %)
$r = 0.45$	Sing ES-FEM	2.6474 (0.2800%)	2.6249 (0.2200 %)	2.4228 (0.2900 %)	2.6244 (0.2700 %)	2.6470 (0.3200 %)
	Sing FEM	2.6417 (0.8500 %)	2.6209 (0.6200 %)	2.4176 (0.8100 %)	2.6210 (0.6100 %)	2.6422 (0.8000 %)
$r = 0.55$	Sing ES-FEM	2.6472 (0.3000 %)	2.6241 (0.3000 %)	2.4225 (0.3200 %)	2.6241 (0.3000 %)	2.6471 (0.3100 %)
	Sing FEM	2.6421 (0.8100 %)	2.6211 (0.6000 %)	2.4188 (0.6900 %)	2.6208 (0.6300 %)	2.6429 (0.7300 %)
$r = 0.65$	Sing ES-FEM	2.6473 (0.3200 %)	2.6242 (0.2900 %)	2.4229 (0.2800 %)	2.6247 (0.2400 %)	2.6472 (0.3000 %)
	Sing FEM	2.6423 (0.7900 %)	2.6208 (0.6300 %)	2.4191 (0.6600 %)	2.6211 (0.6000 %)	2.6425 (0.7700 %)
Average	Sing ES-FEM	2.6473 (0.2900 %)	2.6245 (0.2600 %)	2.4227 (0.3000 %)	2.6245 (0.2600 %)	2.6471 (0.3100 %)
	Sing FEM	2.6421 (0.8100 %)	2.6210 (0.6100 %)	2.4186 (0.7100 %)	2.6211 (0.6000 %)	2.6425 (0.7700 %)
Reference solution		2.6502	2.6271	2.4257	2.6271	2.6502

8.10.2 Homogenous finite plate with a central crack under pure mode I

In order to examine the performance of singular FS-FEM for the curved crack front lines, a homogenous finite plate with two parallel semi-circular surface cracks has been analyzed and the results have been compared with the analytical solution. The structure has the thickness of *t* and width *w*, and undergoes a tension stress σ at both top and

bottom faces as shown in Figure 8.20. Similar to the previous example, this structure is analyzed by modeling only half of it because of the symmetrical load and geometry.

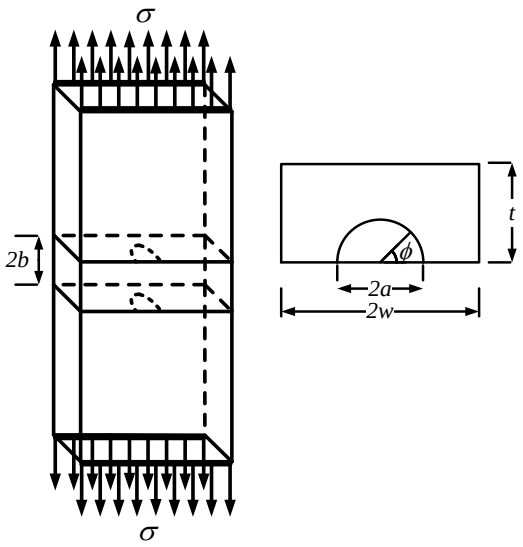

Figure 8.20. Homogenous finite plate with a central crack under pure mode I

An analytical solution for this problem was proposed by Newman and Raju [116] as:

$$K_I = \sigma\sqrt{\frac{\pi a}{Q}}F(a/c, a/t, c/w, \phi)$$
$$F = (1.04 + 0.202(a/t)^2 - 0.16(a/t)^4)gf \tag{8.51}$$

In which f and g are functions of the following forms;

$$g = 1 + (0.1 + 0.35(a/t)^2)(1 - \sin\phi)^2$$
$$f = \left[\sec\left(\frac{\pi a}{2w}\sqrt{\frac{a}{t}}\right)\right]^{1/2} \tag{8.52}$$

In which a and c are crack depth and crack length, respectively. For a semicircular surface crack, $a/c = 1$ and $Q = 2.464$ [117]. In addition, the state of stress for such a solid body is plane stress at the free surfaces ($\phi = 0$) and varies to the plane strain in the

interior part of the plate ($\phi = \frac{\pi}{2}$). Therefore, we have used the following model to describe the Young's modulus of material;

$$E^* = E\left(1 + (\frac{1}{1-\nu^2} - 1)\sin\phi\right) \tag{8.53}$$

Adopting different values of *t* and *w*, the problem has been examined and the results of normalized stress intensity factors have been tabulated in Table 8.5 for three different cases of $\phi = 0$, $\phi = \frac{\pi}{4}$ and $\phi = \frac{\pi}{2}$.

Based on these results, it can be highlighted that our singular FS-FEM provides the accurate and stable results for the domains containing curved cracks.

As it can be observed, for all the cases, normalize value of stress intensity factor obtained from singular ES-FEM is more accurate than that of singular FEM.

Table 8.5. Normalized SIF solution of singular ES-FEM for $b/a = 0.5$ and three different angles

a/w	ϕ	Method	a/t			
			0.1 (error %)	0.2 (error %)	0.3 (error %)	0.4 (error %)
0.1	0	Sing ES-FEM	0.9970 (0.30 %)	0.9973 (0.27 %)	0.9981 (0.29 %)	0.9988 (0.22 %)
		Sing FEM	0.9911 (0.89 %)	0.9917 (0.83 %)	0.9910 (0.90 %)	0.9914 (0.86 %)
	$\pi/4$	Sing ES-FEM	0.9984 (0.26 %)	0.9968 (0.32 %)	0.9971 (0.29 %)	0.9969 (0.07 %)
		Sing FEM	0.9905 (0.95 %)	0.9909 (0.91 %)	0.9911 (0.89 %)	0.9921 (0.79 %)
	$\pi/2$	Sing ES-FEM	0.9989 (0.11 %)	0.9971 (0.29 %)	0.9968 (0.32 %)	0.9972 (0.28 %)
		Sing FEM	0.9919 (0.81 %)	0.9914 (0.86 %)	0.9909 (0.91 %)	0.9917 (0.83 %)
0.2	0	Sing ES-FEM	0.9988 (0.12 %)	0.9984 (0.16%)	0.9982 (0.18 %)	0.9964 (0.36 %)
		Sing FEM	0.9907 (0.93 %)	0.9911 (0.89 %)	0.9904 (0.96 %)	0.9913 (0.87 %)
	$\pi/4$	Sing ES-FEM	1.0001 (0.01 %)	0.9982 (0.18 %)	0.9987 (0.13 %)	0.9983 (0.17 %)
		Sing FEM	0.9918 (0.82 %)	0.9923 (0.77 %)	0.9922 (0.78 %)	0.9916 (0.84 %)
	$\pi/2$	Sing ES-FEM	0.9996 (0.04 %)	0.9991 (0.09 %)	0.9994 (0.06 %)	1.0020 (0.20 %)
		Sing FEM	0.9897 (1.03 %)	0.9922 (0.78 %)	0.9914 (0.86 %)	0.9915 (0.85 %)
0.3	0	Sing ES-FEM	0.9986 (0.14 %)	0.9993 (0.07 %)	0.9988 (0.12 %)	0.9989 (0.11 %)
		Sing FEM	0.9910 (0.90 %)	0.9912 (0.88 %)	0.9929 (0.71 %)	0.9924 (0.76 %)
	$\pi/4$	Sing ES-FEM	0.9996 (0.04 %)	0.9997 (0.03 %)	1.0003 (0.03 %)	0.9994 (0.06 %)
		Sing FEM	0.9933 (0.67 %)	0.9926 (0.74 %)	0.9918 (0.82 %)	0.9917 (0.83 %)
	$\pi/2$	Sing ES-FEM	0.9984 (0.16 %)	0.9997 (0.03 %)	0.9982 (0.18 %)	0.9988 (0.12 %)
		Sing FEM	0.9919 (0.81 %)	0.9916 (0.84 %)	0.9917 (0.83 %)	0.9921 (0.79 %)

8.11 Summary

In this chapter the novel approach of singular face based smoothed finite element method (singular FS-FEM) was formulated and developed. The method uses a basic mesh of linear tetrahedral elements to discretize the domain. Despite the standard finite element method, the proposed singular FS-FEM works very well with a coarse base mesh of *linear tetrahedral elements*. To capture the stress singularity in the stress and strain domain, the method introduces a novel and specially-designed 10-node prism element to be located along the crack front line. The element has a set of shape functions that are (complete) linear in the *r* (radial distance emanating from crack front line) and enriched with a fractional term $\sqrt{r}$ to generate the singular term $1/\sqrt{r}$ in the strain field. For resolving the inconformity issue in where adjacent rectangular and triangular faces of prism and tetrahedral elements meet, 5-node pyramid elements are adopted to connect two different element types. Then the method applies the strain smoothing technique on the boundary faces of all the smoothing volumes associated with the elements faces, and provides a softer model than that of FEM.

The results of analyses indicates that using singular FS-FEM with a base mesh of linear tetrahedral elements provides the more accurate results than that of FEM using a base mesh of higher order elements. This, for sure will increase the computational efficiency. Moreover, the obtained values of stress intensity factors at different points along either straight or curved crack front lines are accurate and stable for different cylindrical domains chosen for the interaction integral calculation.

Chapter 9: Conclusion and Future Work

Try not to become a man of success but rather
try to become a man of value.

Albert Einstein

9.1 Conclusion remarks and research contributions

In the present study, a novel singular finite element method (singular ES-FEM) was developed to be used for analysis of fracture problems in both two and three dimensional cases. The method properly simulates the analytical discontinuity of stress field by proposing a new crack tip element compatibly connected to a mesh of linear triangular or tetrahedral elements. Chapter 4 presented the important foundational theories of the currently established S-FEM models. In Chapter 5, the idea of singular ES-FEM was presented to improve the performance of standard ES-FEM in dealing with fracture problems. In chapter 6, the method was further developed for the interfacial cracks between dissimilar materials. Using the introduced method in chapters 5, a Delaunay triangulation procedure was developed in chapter 7 to automatically generate the mesh for crack propagation analysis through a quasi-static simulation. The developed approach was also used to conduct a case study on the fatigue crack growth prediction. Finally, in chapter 8, another S-FEM method was proposed and formulated for the crack problems in

three dimensional spaces. The study had four main objectives which will be addressed in this section.

Introducing a novel method of singular ES-FEM for the 2-D crack problems:

- The primary aim of the study was to accurately analyze fracture problems in the frame work of smoothed finite element method (S-FEM) using a base mesh of linear 3-node triangular elements. Adapting triangular elements for creating the mesh is desirable due to the feasibility of these elements for being automatically generated even for a very complicated geometry. It was found that in spite of conventional FEM, which does not provide an accurate analysis when linear triangular elements are used, the present method successfully examines the crack parameters based on the linear elements. According to the analyses of several homogenous problems with the proposed method, the results (in terms of strain energy, displacements, and more importantly; stress intensity factors) of singular ES-FEM with *SD*=1 at each crack tip edge are always more accurate than those of standard FEM and ES-FEM using the same mesh of linear triangular elements. It is not always true, however, when it comes to comparison of the method with singular FEM using currently widely-used quarter-point crack tip elements; In some cases the results of singular ES-FEM with *SD*=1 are better than those of singular FEM, while they are not in some other cases. However, by further dividing each crack tip smoothing domain into more sub-smoothing domains (*S-SD*= 2, 3 or 4), performance of the method can be improved compared to the singular FEM. Findings from several examples indicate that when *S-SD*=2 the results are always

more accurate not only than FEM-T3 and ES-FEM, but also than FEM-T6 with quarter-point crack tip elements; This ensured accuracy can be attributed to the proper use of "smoothing technique" on the domains associated with the edges of the elements, leading to a solution for resolving the overly-stiff behavior of the FEM model. Since the FEM provides a monotonically lower bound solution for the solid problems, properly softening the model may yield more accurate results with a lower value of error norm.

- Increasing the number of smoothing domains (*SD*s) associated with each crack tip edge does not show the same effect that the increasing of number of sub-smoothing domains does. In other words, using more smoothing domains associated with each edge makes the model stiffer and declines the accuracy of analysis.

- The conducted study on the relative error in energy norm of the proposed method also shows that our method provides a higher convergence rate compared to all the other methods including FEM-T6. In the case study conducted on a rectangular finite plate with a central crack, it was observed that using only one *S-SD* can yield the convergence rate of 0.7639 which is more than the peer value for FEM-T3 (0.4745), ESFEM (0.5462) and even FEM-T6 (0.7104). Increasing the number of *S-SD* to two will results in a further increase in the convergence rate and provides the super convergence value of 1.0157.

- It can be also observed that there is no significant change in the results when $S - SD > 2$. Although in some cases the method works very well even when one *S-SD* is adopted for the crack tip edges, to be always on the safe side and benefit from

the super convergence behavior, we recommend the use of two *S-SDs* in the present singular ES-FEM.

- The foregoing features of the method are not exclusive to the problem domains containing only one crack. All the remarkable properties of the method were also observed for the domains with more than one crack.

- The simulation results of computational efficiency suggest that the computational efficiency of singular ES-FEM is higher than that of singular FEM with quadratic elements. In other words, the singular ES-FEM with a base mesh of linear elements approaches the analytical solution faster than singular FEM with a mesh of quadratic elements. This amazing property of being faster in reaching the more accurate results is because of the simultaneous use of linear triangular elements instead of quadratic elements and interpolation method instead of isoparametric mapping technique.

- From the analyses based on the general formulation of singular ES-FEM, it was also found that strain energy and stress intensity factors are almost the same for different values of parameter λ which is the parameter for the intermediate node position on the edges directly connected to the crack tip. This implies that in spite of singular FEM, there is no obligation to fix the value of parameter $\lambda = 1/4$ in our singular ES-FEM; meaning that the intermediate nodes could be located in any arbitrary position on the edges when our singular ES-FEM is used ($0 < \lambda < 1$). It may be attributed to the fact that in the singular FEM, the singular term in the stress

field is created only by applying the iso-parametric mapping procedure for a special value of $\lambda = 1/4$. In our singular ES-FEM method, however, the singular term is generated via a direct interpolation method using a proper pre-identified fractional term in the proposed displacement functions.

- From the results**,** it also can be highlighted that the method works well for the stress intensity factor calculations based on the domain form of interact integration. The results are accurate and stable for different area chosen around the crack tip confirming the 'path independency' nature of stress intensity factors calculated with our singular ES-FEM. Since the most important feature of J-integral parameter is the "path-independency", it is of high importance to achieve that feature for the stress intensity factors calculated in the similar fashion by using the interaction integral.

- It should be noted that, the present method enhances the performance of currently established FEM (in terms of accuracy and computational efficiency) in a way that the property of "partition of unity" is always satisfied. This can be justified by considering the fact that in the singular ES-FEM there is no demand for blending elements in the transition zone from "3-noded triangular elements" to the "crack-tip enriched elements". This is because in singular ES-FEM, the compatibility of displacement field between the adjacent elements is ensured by the assumption of linear variation in the tangential direction inside the crack tip elements.

Developing the singular ES-FEM for the interfacial crack analysis

- Another objective of the study was to modify the proposed method for analysis of interfacial cracks between the dissimilar isotropic materials in addition to the isotropic fracture cases. Based on the findings, It can be seen that strain energy and SIFs keep nearly constant when more than 5 Gauss points are used to evaluate the numerical integration of strain gradient matrix components. It also observed that the less the gauss points used, the higher the strain energy and the stress intensity factors. This may be explained that less gauss points bring the effect of the similar reduce integration, and thus lead to over-estimation of results.

- The study on the interfacial crack problems using singular ES-FEM exhibits similar properties observed in analysis of homogenous problems. It can be highlighted from the results that compared to standard FEM, ES-FEM and even FEM with the singular elements, the SIFs and *G* of the singular ES-FEM, no matter the mesh size used, are much closer to the exact values. More importantly, the relative errors of K_I, K_{II} and G using the singular ES-FEM are all within 1 percent for all the models used in the study, except the case of K_{II} value with the very coarse mesh. It also can be observed that convergence of strain energy for the singular ES-FEM models is faster and the error in energy norm is less than that of standard FEM, ES-FEM or FEM-T6 with the singular elements, confirming the fact that singular ES-FEM can solve the interface crack problems effectively. A study using both the structured and unstructured mesh to calculate the stress intensity factors also indicates that the method works very well in providing path-independent results for

the interfacial crack problems.

- The conducted study on the robustness of singular ES-FEM by perturbing the location of crack tip conveys an excellent agreement between the numerical values of SIFs and G with the corresponding exact solutions.

- The performance of the method associated with different material property pairs was also studied by changing the ratio of E_1 / E_2 at the constant poison ratios. It was observed that the results are also accurate to within a few percent relative errors. Furthermore, the method was implemented to a film\substrate system and all the foregoing features were identically observed. In addition, the problem was examined in a fixed total thickness, and different thickness ratios as well as material properties combinations of film and substrate. The steady state energy release rate for different thickness ratio and different material combinations exhibits an excellent agreement with the corresponding reference solutions, and the relative errors are less than 1 percent.

Developing an automatically quasi-static crack propagation simulation using the singular ES-FEM:

- Third objective of the present dissertation was to accomplish a quasi-static crack growth prediction using the singular ES-FEM. The obtained results clearly show that the present singular ES-FEM is able to predict the stress intensity factors and simulate the crack path accurately in a quasi-static propagation procedure. It is of high importance to notice that all the results have been obtained using a simple interpolation method and without any mapping on the natural coordinate of the

elements. Moreover, all the problem domains have been discretized to a largely coarse mesh of linear triangular elements that are known as the simplest elements in two-dimensional space. It should be highlighted that while singular ES-FEM ensures the accuracy of results even when such coarse linear elements are adopted, using standard FEM on the same set of elements causes a considerable loss of accuracy. This analogy helps to better highlighting the power of singular ES-FEM in working with linear elements. The results also imply that singular ES-FEM works very well with maximum circumferential criterion. The mesh generation, node creation, mesh smoothing and adaptive re-meshing are based on the standard Delaunay triangulation procedure which is very straightforward to be implemented.

- The crack incremental value Δa was the only arbitrary parameter in the conducted propagation simulations and based on the strength of shear mode was accordingly chosen in the range of $10\% - 20\%$ of initial crack length a, inversely proportional to the ratio of $\left|K_{II}/K_{I}\right|$. Generally, by choosing a smaller length of increment, the trajectory of the crack growth will be predicted more accurately, particularly in the regions where the ratio of $\left|K_{II}/K_{I}\right|$ is relatively high. The numerical results indicate that the predicted crack trajectory can be somewhat affected by the length of crack increment; however, for the small enough increments the variation in the paths can be ignored. To be on the safe side, the method can occasionally decline the incremental value for the solution steps at which high shear mode occurs.

- Fatigue analysis of the structures undergoing thousands cycles of varying-amplitude load indicate that the results of our singular ES-FEM have an excellent agreement with the findings from the experimental studies. Two different models of Forman and Kujawski's were successfully adopted in the frame work of developed adaptive singular ES-FEM and provided the results that confirm capability of singular ES-FEM in dealing with fatigue crack growth simulations.

Introducing a novel method of singular FS-FEM for the 3-D crack problems:

- The final aim of the present study was to formulate a S-FEM approach for the 3-D crack problems. To this end, a novel approach of singular face based smoothed finite element method (singular FS-FEM) was proposed, formulated and developed. The method uses a base mesh of linear tetrahedral elements to discretize the domain. Despite the standard finite element method, the proposed singular FS-FEM works very well with a coarse base mesh of *linear tetrahedral elements*. To capture the stress singularity in the stress and strain domain, the method introduces a novel and specially-designed 10-node prism element to be located along the crack front line. The element is armed with a set of shape functions that are (complete) linear in the r (radial distance emanating from crack front line) and enriched with a fractional term $\sqrt{r}$ to generate the singular term $1/\sqrt{r}$ in the strain field. For resolving the inconformity issue in where adjacent rectangular and triangular faces of prism and tetrahedral elements meet, 5-node pyramid elements are adopted. Then, the method applies the strain smoothing technique on the boundary faces of

all the smoothing volumes associated with the elements faces, and provides a softer model than that of FEM.

- The results of analysis indicate that using singular FS-FEM with a base mesh of linear tetrahedral elements provides the more accurate results than that of FEM using a base mesh of higher order elements. Moreover, the obtained values of stress intensity factors at different points along either straight or curved crack front lines are accurate and stable for different cylindrical volumes chosen for the interaction integral calculation.

- In summary, singular FS-FEM with a direct interpolation method on a combination of "one layer of proposed 10-node crack tip prism elements along the crack front line", "4-node linear tetrahedral elements at the rest parts of the domain", and "5-node pyramid elements in between" successfully provides the results which are more accurate than FEM using a mapping procedure on an entire mesh of higher order elements. Although, using the strain smoothing technique significantly helps to provide a softer discretized model, the main improvement of our singular FS-FEM for the fracture applications is due to the use of novel prism elements. The method is straightforward and easy to implement.

9.2 Recommendations for future works

First, as one of the novel numerical methods, mathematical proofs about the characters and advantages of the proposed new numerical method have not been explored comprehensively in this research. Some obtained results were mainly drawn from the

numerical results which may restrict the general application of the methods to a certain degree. Further study is therefore needed to develop mathematical bases for the method. This not only makes the proposed new numerical method more applicable to practical engineering problems with certain confidence, but also guides us on how to further improve the solutions. It is now clearly necessary to establish a general theoretical framework to justify the formulation of the newly developed FEM model, similar to the works have been recently performed by Liu [118-122] to establish the new functional spaces containing the S-FEM models and S-PIM models. However, many theoretical aspects related to these spaces still need to be analyzed in details in the coming time.

Second, based on the achievements of the method in dealing with elementary and basic sample problems, it seems necessary to implement the established method on the more practical engineering problems to analyze the structures with complicated geometries undergoing complicated loading conditions. This will help the further modification of the method to be suit for the real problems of industry. For instance, it seems necessary to establish the method for the more popular material structures like composite materials which are widely used in the vehicle and aerospace industry because of their remarkable features including high strength and low weight.

Third, both approaches of singular ES-FEM and singular FS-FEM were established for the linear fracture problems with a very small plastic deformation zone at the crack tip compared to the characteristic length of the crack. Since analysis of the non-linear fracture mechanics was out of the scope of present dissertation, this type of failure has

not been studied. More studies on extension of present methods to the case of non-linear fracture problems are suggested.

Fourth, the present methods were formulated to produce a singular term of order ½ around the crack tip. Higher orders of singularity can be produced to examine if there is an improvement in the accuracy and computational efficiency.

Fifth, for the three dimensional cases, the method of singular FS-FEM for the stationary crack analyses was successfully developed using three different element types. The propagation of the crack in three dimensional cases has not been presented in the present study. In the future works, this can be sought by initially creating a mesh of prism elements along the crack front line and moving this set of elements with the crack front while the crack propagates. The re-meshing problem can be then simplified to the tetrahedral re-meshing on the rest part of the domain.

Finally, it is promising to develop the more accurate models by combining the present method with the other competitive methods established based on the strong discontinuity theory. The method can be also studied in more details to extend the idea in the Multiscale simulations.

References

[1] *R. D. Henshell and K. G. Shaw, "crack tip finite elements are unnecessary," Int J Numer Methods Eng, vol. 9, pp. 495-507. , 1975.*

[2] *R. S. Barsoum, "On the Use of Isoparametric Finite Elements in Linear Fracture Mechanics," International Journal for Numerical Methods in Engineering, vol. 10, pp. 25-37, 1976.*

[3] *R. S. Barsoum, "Triangular Quarter-Point Elements as Elastic and Perfectly-Plastic Crack Tip Elements," International Journal for Numerical Methods in Engineering, vol. 11, pp. 85-98, 1977.*

[4] *J. M. Melenk and I. Babuska, "The partition of unity finite element method: Basic theory and applications," Computer Methods in Applied Mechanics and Engineering, vol. 139, pp. 289-314, Dec 15 1996.*

[5] *T. Belytschko and T. Black, "Elastic crack growth in finite elements with minimal remeshing," International Journal for Numerical Methods in Engineering, vol. 45, pp. 601-620, Jun 20 1999.*

[6] *N. Moes, et al., "A finite element method for crack growth without remeshing," International Journal for Numerical Methods in Engineering, vol. 46, pp. 131-150, Sep 10 1999.*

[7] *C. Daux, et al., "Arbitrary branched and intersecting cracks with the extended finite element method," International Journal for Numerical Methods in Engineering, vol. 48, pp. 1741-1760, Aug 30 2000.*

[8] *J. Chessa, Wang, H., and Belytschko, T, "On the construction of blending elements for local partition of unity enriched finite elements," International Journal for Numerical Methods in Engineering, vol. 57, pp. 1015-1038, 2003.*

[9] *T. P. Fries, "A corrected XFEM approximation without problems in blending elements," International Journal for Numerical Methods in Engineering, vol. 75, pp. 503-532, Jul 30 2008.*

[10] *J. E. Tarancon, et al., "Enhanced blending elements for XFEM applied to linear elastic fracture mechanics," International Journal for Numerical Methods in Engineering, vol. 77, pp. 126-148, Jan 1 2009.*

[11] *G. R. Liu, et al., "A smoothed finite element method for mechanics problems," Computational Mechanics, vol. 39, pp. 859-877, May 2007.*

[12] *G. R. Liu, et al., "Theoretical aspects of the smoothed finite element method (SFEM)," International Journal for Numerical Methods in Engineering, vol. 71, pp. 902-930, Aug 20 2007.*

[13] *G. R. Liu and T. T. Nguyen, Smoothed Finite Element Methods. Boca Raton: CRC Press, 2010.*

[14] *C. E. Inglis, "Stresses in a plate due to pressence of cracks and sharp corners," transactions of the institute of naval architects, vol. 2, pp. 5-32, 1913.*

[15] *A. A. Griffith, "The phenomena of rupture and flow in solids," Phylosophical transaction of the royal society, vol. 221, pp. 163-198, 1920.*

[16] *G. R. Irwin, "Analysis of stresses and strains near the end of a crack trasversing a plate," Journal of applied mechanics, vol. 24, pp. 361-364, 1957.*

[17] *E. Orowan, "Energy criterion of fracture," Welding research supplement, vol. 20, p. 157, 1955.*

[18] *H. M. Westergaard, "Bearing pressures and cracks," Journal of applied mechanics, vol. 6, pp. 49-53, 1939.*

[19] *I. N. Sneddon, "The distribution of stress in the neighborhood of a crack in an elastic solid," Proceeding of royal society of london A, vol. 187, pp. 229-260, 1946.*

[20] *M. L. Williams, "On the stress distribution at the base of statinary crack," Journal of applied mechanics, vol. 24, pp. 109-114, 1957.*

[21] *J. R. Rice, "A path independent integral and the approximate analysis of strain concentration by notches and cracks," Journal of applied mechanics, vol. 35, pp. 379-386, 1968.*

[22] *F. Z. Li, et al., "A Comparison of Methods for Calculating Energy-Release Rates," Engineering Fracture Mechanics, vol. 21, pp. 405-421, 1985.*

[23] *A. R. Ingraffea and P. A. Wawrzynek, "3.01 - Finite Element Methods for Linear Elastic Fracture Mechanics," in Comprehensive Structural Integrity, I. M. Editors-in-Chief: , et al., Eds., ed Oxford: Pergamon, 2003, pp. 1-88.*

[24] *I. Milne, et al., "Comprehensive Structural Integrity, Volumes 1-10," ed: Elsevier.*

[25] *J. R. Mohanty, et al., "Prediction of fatigue crack growth and residual life using an exponential model: Part I (constant amplitude loading)," International Journal of Fatigue, vol. 31, pp. 418-424, Mar 2009.*

[26] *R. P. Wei and A. J. McEvily, "Fracture mechanics and corrosion fatigue," in Conference on Corrosion Fatigue, 1971, pp. 381-395.*

[27] *R. O. Ritchie, "Influence of Microstructure and Mean Stress on near-Threshold fatigue crack propagation in ultra-high strength steel," Metal Science, vol. Aug/Sep, pp. 368-381, 1977.*

[28] *D. Kujawski and F. Ellyin, "A Fatigue Crack-Growth Model with Load Ratio Effects," Engineering Fracture Mechanics, vol. 28, pp. 367-378, 1987.*

[29] *M. Klesnil and P. Lukas, "Effect of Stress Cycle Asymmetry on Fatigue Crack Growth," Materials Science and Engineering, vol. 9, pp. 231-&, 1972.*

[30] *P. C. Paris and F. Erdogan, "A critical analysis of crack propagation law," J basic Eng, vol. 85, pp. 528-534, 1963.*

[31] *A. M. L. Adib and C. A. R. P. Baptista, "An exponential equation of fatigue crack growth in titanium," Materials Science and Engineering a-Structural Materials Properties Microstructure and Processing, vol. 452, pp. 321-325, Apr 15 2007.*

[32] *R. G. Forman, et al., "Numerical analysis of crack propagation in cyclic-loaded structures," J basic Eng, vol. 89, pp. 459-464, 1967.*

[33] *K. Walker, "the effect of stress ratio during crack propagation and fatigue for 2024-T3 and 7075-T6 aluminum. ," Effect of Enviroment and Complex load history for Fatigue life, ASTM STP, vol. 462, pp. 1-14, 1970.*

[34] *W. Elber, "fatigue crack closure under cyclic tension," Engineering Fracture Mechanics, vol. 2, pp. 37-44, 1970.*

[35] *W. Elber, "the Significance of Fatigue Crack Closure - Damage Tolerance in Aircraft Structures," Americam Society for Testing and Materials, vol. 486, pp. 230-242, 1971.*

[36] *D. Kujawski, "Correlation of long- and physically short-cracks growth in aluminum alloys," Engineering Fracture Mechanics, vol. 68, pp. 1357-1369, Aug 2001.*

[37] *J. C. Newman, et al., "Crack-growth calculations in 7075-T7351 aluminum alloy under various load spectra using an improved crack-closure model," Engineering Fracture Mechanics, vol. 71, pp. 2347-2363, Nov 2004.*

[38] *C. M. Pang and J. H. Song, "Crack-Growth and Closure Behavior of Short Fatigue Cracks," Engineering Fracture Mechanics, vol. 47, pp. 327-343, Feb 1994.*

[39] *J. C. Newman, et al., "Small-crack growth and fatigue life predictions for high-strength aluminium alloys. Part II: crack closure and fatigue analyses," Fatigue & Fracture of Engineering Materials & Structures, vol. 23, pp. 59-72, Jan 2000.*

[40] *K. Donald and P. C. Paris, "An evaluation of Delta K-eff estimation procedures on 6061-T6 and 2024-T3 aluminum alloys," International Journal of Fatigue, vol. 21, pp. S47-S57, Nov 1999.*

[41] *D. Kujawski, "Enhanced model of partial crack closure for correlation of R-ratio effects in aluminum alloys," International Journal of Fatigue, vol. 23, pp. 95-102, Feb 2001.*

[42] *P. C. Paris, et al., "Service load fatigue damage - a historical perspective," International Journal of Fatigue, vol. 21, pp. S35-S46, Nov 1999.*

[43] *D. Kujawski, "A new (Delta K+Kmax)(0.5) driving force parameter for crack growth in aluminum alloys," International Journal of Fatigue, vol. 23, pp. 733-740, Sep 2001.*

[44] *S. Y. Lee and J. H. Song, "Crack closure and growth behavior of physically short fatigue cracks under random loading," Engineering Fracture Mechanics, vol. 66, pp. 321-346, Jun 2000.*

[45] *G. Maymon, "A 'unified' and a (Delta K+center dot K-max)(1/2) crack growth models for aluminum 2024-T351," International Journal of Fatigue, vol. 27, pp. 629-638, Jun 2005.*

[46] *D. Kujawski, "A fatigue crack driving force parameter with load ratio effects," International Journal of Fatigue, vol. 23, pp. S239-S246, 2001.*

[47] S. Dinda and D. Kujawski, "Correlation and prediction of fatigue crack growth for different R-ratios using K-max and Delta K+ parameters," Engineering Fracture Mechanics, vol. 71, pp. 1779-1790, Aug 2004.

[48] Reddy. B. D., Introductory Functional Analysis. New York: Springer-Verlag, 1998.

[49] Delaunay. B., " Sur la sphère vide, Izvestia Akademii Nauk SSSR," Otdelenie Matematicheskikh i Estestvennykh Nauk, vol. 7, pp. 793–800, 1934.

[50] Voronoi. G., "Nouvelles applications des paramètres continus à la théorie des formes quadratiques," Journal für die Reine und Angewandte Mathematik, vol. 133, pp. 97-178, 1908.

[51] L. Guibas and J. Stolfi, "Primitives for the Manipulation of General Subdivisions and the Computation of Voronoi Diagrams," Acm Transactions on Graphics, vol. 4, pp. 74-123, 1985.

[52] K. L. Clarkson and P. W. Shor, "Applications of Random Sampling in Computational Geometry .2.," Discrete & Computational Geometry, vol. 4, pp. 387-421, 1989.

[53] P. J. Green and R. Sibson, "Computing Dirichlet Tessellations in Plane," Computer Journal, vol. 21, pp. 168-173, 1978.

[54] L. J. Guibas, et al., "Randomized Incremental Construction of Delaunay and Voronoi Diagrams," Algorithmica, vol. 7, pp. 381-413, 1992.

[55] T. Ohya, et al., "Improvements of the Incremental Method for the Voronoi Diagram with Computational Comparison of Various Algorithms," Journal of the Operations Research Society of Japan, vol. 27, pp. 306-337, 1984.

[56] S. Fortune, "A Sweepline Algorithm for Voronoi Diagrams," Algorithmica, vol. 2, pp. 153-174, 1987.

[57] J. U. Fang, et al., "Sweepline Algorithm for Unstructured-Grid Generation on 2-Dimensional Nonconvex Domains," International Journal for Numerical Methods in Engineering, vol. 36, pp. 2761-2778, Aug 30 1993.

[58] S. M. Hu, et al., "A sweepline algorithm for Euclidean Voronoi diagram of circles," Computer-Aided Design, vol. 38, pp. 260-272, Mar 2006.

[59] R. A. Dwyer, "Higher-Dimensional Voronoi Diagrams in Linear Expected Time," Discrete & Computational Geometry, vol. 6, pp. 343-367, 1991.

[60] A. Maus, "Delaunay Triangulation and the Convex-Hull of N-Points in Expected Linear Time," BIT, vol. 24, pp. 151-163, 1984.

[61] M. Tanemura, et al., "A New Algorithm for 3-Dimensional Voronoi Tessellation," Journal of Computational Physics, vol. 51, pp. 191-207, 1983.

[62] C. B. Barber, "Computational geometry with imprecise data and arithmetic," Ph D, Princeton University, 1992.

[63] D. Hoey and M. I. Shamos, "Efficient Computations in Geometry," Notices of the American Mathematical Society, vol. 22, pp. A596-A597, 1975.

[64] D. T. Lee and B. J. Schachter, "2 Algorithms for Constructing a Delaunay Triangulation," International Journal of Computer & Information Sciences, vol. 9, pp. 219-242, 1980.

[65] T. Ohya, et al., "A Fast Voronoi-Diagram Algorithm with Quaternary Tree Bucketing," Information Processing Letters, vol. 18, pp. 227-231, 1984.

[66] R. A. Dwyer, "A Faster Divide-and-Conquer Algorithm for Constructing Delaunay Triangulations," Algorithmica, vol. 2, pp. 137-151, 1987.

[67] J. Katajainen, et al., "Divide and Conquer for the Closest-Pair Problem Revisited," International Journal of Computer Mathematics, vol. 27, pp. 121-132, 1989.

[68] J. M. Moreau and C. Lemaire, "A probabilistic result on multi-dimensional Delaunay triangulations, and its application to the 2D case," Computational Geometry-Theory and Applications, vol. 17, pp. 69-96, Oct 2000.

[69] J. R. Camacho, et al., "A functional language to implement the divide-and-conquer Delaunay triangulation algorithm," Applied Mathematics and Computation, vol. 168, pp. 178-191, Sep 1 2005.

[70] Y. Choi, et al., "A divide-and-conquer Delaunay triangulation algorithm with a vertex array and flip operations in two-dimensional space," International Journal of Precision Engineering and Manufacturing, vol. 12, pp. 435-442, Jun 2011.

[71] J. R. Sack and J. Urrutia, Handbook of computational geometry. Amsterdam ; New York: Elsevier, 2000.

[72] Owen. S. J., "A survey of unstructured mesh generation technology," In Proceedings of the 7th International Meshing Roundtable, pp. 239–267, 1998.

[73] H. Edelsbrunner, Geometry and topology for mesh generation. Cambridge ; New York: Cambridge University Press, 2001.

[74] E. Byskov, "The Calculation of Stress Intensity Factors Using the Finite-Element Method with Cracked Elements," International Journal of Fracture, vol. 6, pp. 159-167, 1970.

[75] D. M. Tracey, "Finite Element for determination of crack tip elastic stress intensity factors," Engineering Fracture Mechanics, vol. 3, pp. 255-256, 1971.

[76] P. Tong, et al., "A Hybrid Element Approach to crack problems in plane elasticity," Int J Numer Methods Eng, vol. 7, pp. 1031-1036, 1973.

[77] S. G. Papaioannou, et al., "A Finite Element Method for calculating stress intensity factors and its application to composites," Engineering Fracture Mechanics, vol. 6, pp. 807-823, 1974.

[78] S. N. Atluri, et al., "An assumed displacement hybrid finite element model for linear elastic fracture mechanics," Int J Fracture, vol. 11, pp. 257-271, 1975.

[79] D. M. Tracey and T. S. Cook, "ANALYSIS OF POWER TYPE SINGULARITIES USING FINITE-ELEMENTS," International Journal for Numerical Methods in Engineering, vol. 11, pp. 1225-1233, 1977.

[80] J. E. Akin, "GENERATION OF ELEMENTS WITH SINGULARITIES," International Journal for Numerical Methods in Engineering, vol. 10, pp. 1249-1259, 1976.

[81] W. S. Blackburn, "Calculation of stress intensity factors at crack tips using special finite elements," in The mathematics of finite elements, New York, 1973, pp. 327-336.

[82] S. E. Benzely, "Representation of singularities with isoparametric finite elements," International journal for numerical methods in engineering, vol. 8, 1974.

[83] R. D. Henshell and K. G. Shaw, "Crack tip finite elements are unnecessary," International Journal for Numerical Methods in Engineering, vol. 9, pp. 495-507, 1976.

[84] C. E. Freese and D. M. Tracey, "The natural triangle versus collapsed quadrilateral for elastic crack analysis," Int J Fracture, vol. 12, pp. 767-770, 1976.

[85] R. S. Barsoum, "Triangular quarter-point elements as elastic and perfectly-plastic crack-tip elements," Int J Numer Methods Eng, vol. 11, pp. 85-98, 1977.

[86] L. Bankssills and Y. Bortman, "Reappraisal of the Quarter-Point Quadrilateral Element in Linear Elastic Fracture-Mechanics," International Journal of Fracture, vol. 25, pp. 169-180, 1984.

[87] L. Bankssills, "Quarter Point Singular Elements Revisited," International Journal of Fracture, vol. 34, pp. R63-R69, Aug 1987.

[88] J. S. Chen, et al., "Regularization of material instabilities by meshfree approximations with intrinsic length scales," International Journal for Numerical Methods in Engineering, vol. 47, pp. 1303-1322, Mar 10 2000.

[89] T. Nguyen-Thoi, et al., "On the essence and the evaluation of the shape functions for the smoothed finite element method (SFEM)," International Journal for Numerical Methods in Engineering, vol. 77, pp. 1863-1869, Mar 26 2009.

[90] G. R. Liu, et al., "A node-based smoothed finite element method (NS-FEM) for upper bound solutions to solid mechanics problems," Computers & Structures, vol. 87, pp. 14-26, Jan 2009.

[91] G. R. Liu, et al., "An edge-based smoothed finite element method (ES-FEM) for static, free and forced vibration analyses of solids," Journal of Sound and Vibration, vol. 320, pp. 1100-1130, Mar 6 2009.

[92] T. Nguyen-Thoi, et al., "A novel alpha finite element method (alpha FEM) for exact solution to mechanics problems using triangular and tetrahedral elements," Computer Methods in Applied Mechanics and Engineering, vol. 197, pp. 3883-3897, 2008.

[93] T. Nguyen-Thoi, et al., "A face-based smoothed finite element method (FS-FEM) for 3D linear and geometrically non-linear solid mechanics problems using 4-node tetrahedral elements," International Journal for Numerical Methods in Engineering, vol. 78, pp. 324-353, Apr 16 2009.

[94] G. R. Liu and S. S. Quek. (2003). The finite element method : a practical course / G.R. Liu and S.S. Quek.

[95] O. C. Zienkiewicz and R. L. Taylor, The finite element method, 5th ed. Oxford: Butterworth Heinemann, 2000.

[96] H. Tada, et al., The stress analysis of cracks handbook, 3rd ed. New York: ASME Press, 2000.

[97] J. F. Yau, et al., "A Mixed-Mode Crack Analysis of Isotropic Solids Using Conservation-Laws of Elasticity," Journal of Applied Mechanics-Transactions of the Asme, vol. 47, pp. 335-341, 1980.

[98] J. R. Rice, "Elastic Fracture-Mechanics Concepts for Interfacial Cracks," Journal of Applied Mechanics-Transactions of the Asme, vol. 55, pp. 98-103, Mar 1988.

[99] C. F. Shih, "Cracks on Bimaterial Interfaces - Elasticity and Plasticity Aspects," Materials Science and Engineering a-Structural Materials Properties Microstructure and Processing, vol. 143, pp. 77-90, Sep 15 1991.

[100] J. Dundurs and D. B. Bogy, "Edge-Bonded Dissimilar Orthogonal Elastic Wedges under Normal and Shear Loading," Journal of Applied Mechanics, vol. 36, pp. 650-&, 1969.

[101] B. Moran and C. F. Shih, "Crack Tip and Associated Domain Integrals from Momentum and Energy-Balance," Engineering Fracture Mechanics, vol. 27, pp. 615-642, 1987.

[102] J. R. Rice and G. C. Sih, "Plane Problems of Cracks in Dissimilar Media," Mechanical Engineering, vol. 87, pp. 81-&, 1965.

[103] P. G. Charalambides, et al., "A test specimen for determining the fracture resistance of bimaterial interfaces," Journal of Applied Mechanics, vol. 56, pp. 77-82, 1989.

[104] C. F. Shih and R. J. Asaro, "Elastic-Plastic Analysis of Cracks on Bimaterial Interfaces .1. Small-Scale Yielding," Journal of Applied Mechanics-Transactions of the Asme, vol. 55, pp. 299-316, Jun 1988.

[105] F. Erdogan and G. Shih, "On the crack extension in plates under plane loading and transverse shear," Journal of Basic Engineering vol. 85 pp. 519-527, 1963.

[106] W. Shen and J. D. Lee, "The Non-Linear Energy Method for Mixed-Mode Fracture," Engineering Fracture Mechanics, vol. 16, pp. 783-798, 1982.

[107] T. N. Bittencourt, et al., "Quasi-automatic simulation of crack propagation for 2D LEFM problems," Engineering Fracture Mechanics, vol. 55, pp. 321-334, Sep 1996.

[108] S. Phongthanapanich and P. Dechaumphai, "Adaptive Delaunay triangulation with object-oriented programming for crack propagation analysis," Finite Elements in Analysis and Design, vol. 40, pp. 1753-1771, Aug 2004.

[109] B. N. Rao and S. Rahman, "An efficient meshless method for fracture analysis of cracks," Computational Mechanics, vol. 26, pp. 398-408, Oct 2000.

[110] R. Huang, et al., "Modeling quasi-static crack growth with the extended finite element method Part II: Numerical applications," International Journal of Solids and Structures, vol. 40, pp. 7539-7552, Dec 2003.

[111] G. H. Lee, et al., "Adaptive crack propagation analysis with the element-free Galerkin method," International Journal for Numerical Methods in Engineering, vol. 56, pp. 331-350, Jan 21 2003.

[112] C. F. Shih, et al., "Energy-Release Rate Along a 3-Dimensional Crack Front in a Thermally Stressed Body," International Journal of Fracture, vol. 30, pp. 79-102, Feb 1986.

[113] R. H. Dodds, et al., "Interaction integral procedures for 3-D curved cracks including surface tractions," Engineering Fracture Mechanics, vol. 72, pp. 1635-1663, Jul 2005.

[114] M. Gosz and B. Moran, "An interaction energy integral method for computation of mixed-mode stress intensity factors along non-planar crack fronts in three dimensions," Engineering Fracture Mechanics, vol. 69, pp. 299-319, Feb 2002.

[115] M. L. Williams, "On the stress distribution at the base of a stationary crack," ASME J Appl Mech vol. 24, pp. 109-114, 1957.

[116] J. C. Newman and I. S. Raju, "Stress intensity factor equations for crack in three-dimensional finite bodies," in Fracture Mechanics, 1983.

[117] Z. D. Jiang, et al., "Stress intensity factors of two parallel 3d surface cracks," Engineering Fracture Mechanics, vol. 40, pp. 345-354, 1991.

[118] G. R. Liu and T. T. Nguyen, Smoothed finite element methods. Boca Raton: CRC Press, 2010.

[119] G. R. Liu, "A Generalized Gradient Smoothing Technique and the Smoothed Bilinear Form for Galerkin Formulation of a Wide Class of Computational Methods," International Journal of Computational Methods, vol. 5, pp. 199-236, Jun 2008.

[120] G. R. Liu, "A G space theory and a weakened weak (W(2)) form for a unified formulation of compatible and incompatible methods: Part I theory," International Journal for Numerical Methods in Engineering, vol. 81, pp. 1093-1126, Feb 26 2010.

[121] G. R. Liu, "A G space theory and a weakened weak (W(2)) form for a unified formulation of compatible and incompatible methods: Part II applications to solid mechanics problems," International Journal for Numerical Methods in Engineering, vol. 81, pp. 1127-1156, Feb 26 2010.

[122] G. R. Liu, "A G Space Theory with Discontinuous Functions for Weakened Weak (W2) Formulation of Numerical Methods," Analysis of Discontinuous Deformation: New Developments and Applications, pp. 37-38, 2010.

List of Publications

Journal papers:

1. **N. Nourbakhshnia**, G. R. Liu, *A quasi-static crack growth simulation based on the singular ES-FEM*, International Journal for Numerical Methods in Engineering, 88 (2011), 473–492
2. **N. Nourbakhshnia**, G. R. Liu, *Fatigue Analysis using the singular ES-FEM*, International Journal of fatigue, (2011), Accepted for publication, DOI: 10.1016/j.ijfatigue.2011.12.018
3. **N. Nourbakhshnia**, G. R. Liu, *A Novel Singular Face-based Smoothed Finite Element Method for three-dimensional linear elastic fracture problems* , (2012), In preperation
4. G. R. Liu, **N. Nourbakhshnia**, *A novel singular ES-FEM method for simulating singular stress fields near the crack tips for linear fracture problems*, Engineering Fracture Mechanics, 78 (2011) 863-876
5. G. R. Liu, **N. Nourbakhshnia**, L. Chen, Y. W. Zhang, *Analysis of mixed-mode fracture problems using a new general formulation for ES-FEM method*, International Journal of Computational Methods, Vol. 7(1) (2010) 191-214
6. H. Nguyen-Xuana, G.R. Liu, **N. Nourbakhshnia**, L. Chen, *A novel singular ES-FEM for crack growth simulation*, Engineering Fracture Mechanics, 84 (2012) 41-66
7. L.Chen, G. R. Liu, **N. Nourbakhsh-Nia**, K. Zeng, *A singular edge-based smoothed finite element method (ES-FEM) for bimaterial interface cracks*, Computational Mechanics, 45 (2010) 109–125.

Conference papers:

1. **N. Nourbakhsh Nia**, G.R. Liu, *Crack growth simulation using smoothed FEM*, 9th Word Congress on Computational Mechanics (WCCM), Sydney, Australia, 19-23 July 2010
2. **N. Nourbakhsh Nia**, G.R. Liu, *Simulation of Stress Singularity around the crack tips for LEFM problems using a new numerical method*, 9th International Conference on Analysis of Discontinuous Deformation (ICADD9), Singapore , 25 – 27 November 2009